Barium tagging for a future nEXO upgrade

Simulating barium ion motion in liquid xenon for a future barium tagging upgrade of nEXO

By Megan Cvitan, B.Sc.

A Thesis Submitted to the School of Graduate Studies in the Partial Fulfillment of the Requirements for the Degree Master of Science

McMaster University

McMaster University
Master of Science (2024)
Hamilton, Ontario (Physics & Astronomy)

TITLE: Simulating barium ion motion in liquid xenon for a future barium tagging upgrade of nEXO
AUTHOR: Megan Cvitan, B.Sc. (McGill University, 2021)
SUPERVISORS: Dr. Alan Chen & Dr. Annika Lennarz
NUMBER OF PAGES: xi, 101

Abstract

The neutrino is one of the most abundant elementary particles in the Universe, and plays important roles in proposed answers to many frontier scientific questions, such as matter-antimatter asymmetry, and by what mechanism and processes do massive stars end their lives in supernova explosions. Nevertheless, some of the neutrino's most basic properties remain poorly understood, in particular, the neutrino's mass. One avenue to determine the mass of the neutrino and explore its origin is the study of a hypothetical nuclear decay process known as neutrinoless double beta decay ($0\nu\beta\beta$).

The nEXO experiment is a tonne-scale liquid xenon (LXe) time projection chamber that aims to uncover properties of neutrinos via the $0\nu\beta\beta$ in the isotope ^{136}Xe. The observation of $0\nu\beta\beta$ would point to new physics beyond the Standard Model and imply lepton number violation, indicating that neutrinos are their own antiparticle and thus change our understanding of the universe.

The collaboration has been pursuing the development of Ba-tagging as a potential technique to further improve upon the detection sensitivity of nEXO by detecting the daughter isotope ^{136}Ba, produced from the $\beta\beta$ of ^{136}Xe. This technique aims to extract single daughter Ba ions from a LXe volume. Ba-tagging would allow for an unambiguous identification of true $\beta\beta$ decay events. Various Ba-ion extraction approaches are under investigation by the nEXO collaboration. The groups at TRIUMF and McGill University are developing an accelerator-driven ion source to implant radioactive beam ions inside a LXe volume, for subsequent ion extraction and identification via methods under development by other nEXO collaborators. In the first phase, radioactive ions will be extracted using an electrostatic probe for subsequent identification by γ spectroscopy.

This thesis describes the setup, fluid dynamics and particle ray tracing simulations to study the motion of barium ions in liquid xenon, and ion extraction efficiency simulations using an electrostatic probe.

Acknowledgements

First and foremost, I would like to thank my two supervisors Dr. Annika Lennarz and Dr. Alan Chen for giving me the opportunity to work at TRIUMF and join the nEXO collaboration, and for their tremendous support and patience. Thank you to my former advisor Dr. Thomas Brunner for introducing me to neutrino physics and for all of the support over the years.

Thanks to all of the Ba-tagging collaborators at McGill and Carleton, and especially Dr. Robert Collister for his extensive guidance on running COMSOL simulations. Thank you to Dr. Dwaipayan Ray for taking the time to answer all of my questions, and taking over the Ba-tagging project while I was away.

Thank you to the former and current McMaster co-op undergraduate students for all of their hard work. Thank you to the TITAN group at TRIUMF for adopting me and teaching me about ion traps, and everyone I got to work with at McMaster while I was finishing my coursework.

I am grateful to my parents, my sister, my future in-laws, and my friends for their unconditional encouragement and for reminding me to take it easy sometimes.

Finally, I would like to thank my little family: my wonderful husband-to-be, and our beautiful daughter. You two give me the motivation to jump out of bed each and every day, and I can't wait for the rest of our adventures in this mountainous land.

Contents

Abstract iii

Acknowledgements iv

Declaration of Authorship x

1 Theoretical background 1
- 1.1 Neutrinos . . . 1
- 1.2 Neutrino Oscillations and Neutrino Mass . . . 2
- 1.3 Neutrinoless Double Beta Decay . . . 6
- 1.4 Searching for $0\nu\beta\beta$ with EXO-200 and nEXO . . . 11
- 1.5 Ba-tagging for a Future $0\nu\beta\beta$ Decay Experiment . . . 15
- 1.6 Ion Mobility in Noble Gases . . . 18

2 Methodology and Apparatus 22
- 2.1 Radioactive Ion Beams at TRIUMF . . . 22
- 2.2 Barium Tagging Apparatus at TRIUMF . . . 24
- 2.3 Commissioning in Gas Media and Proposed Experimental Plan . . . 29

3 Electrostatic Probe Simulations 36
- 3.1 Software Considerations . . . 36
- 3.2 Benchmark Model . . . 37
- 3.3 Simulation Environment . . . 40
  - 3.3.1 Simulation Geometries . . . 40
  - 3.3.2 Solving Electrostatics . . . 41
  - 3.3.3 Fluid Dynamics Solution . . . 44
  - 3.3.4 Particle Tracing . . . 51
- 3.4 Attraction Efficiency Simulation Results . . . 57
  - 3.4.1 Probe Bias Effects on Extraction Efficiency . . . 58
  - 3.4.2 Varying Probe Shapes and Probe Depth . . . 61
  - 3.4.3 Fluid Velocity Field Effects on Extraction Efficiency . . . 65
  - 3.4.4 Effects of Proximity to Probe on Extraction Efficiency . . . 71
  - 3.4.5 Feasibility of Commissioning with Other Liquid and Gas Noble Mediums . . . 74
  - 3.4.6 Modifications to Beam Entrance Window . . . 80

4 Discussion **84**
4.1 Future Outlook 85

A Saturation and Decay Chain Plots **87**

B Beam Delivery of ^{139}Cs and ^{139}Ba **90**

C Extraction Efficiency Plot **93**

List of Figures

1.1 The two possible neutrino mass hierarchies. . . . 6
1.2 The mass parabola maps the valley of stability against β-decays. . . . 7
1.3 Feynman diagrams of $2\nu\beta\beta$ and $0\nu\beta\beta$. . . . 8
1.4 Energy spectra for $2\nu\beta\beta$ and $0\nu\beta\beta$ decays. . . . 11
1.5 Artist's rendition of the EXO-200 detector. . . . 12
1.6 Artist's rendition of the nEXO experiment. . . . 14
1.7 nEXO sensitivity and discovery potential. . . . 15
1.8 nEXO detector sensitivity to $0\nu\beta\beta$ half-lives vs background models. . . . 16
1.9 Overview of conceptual steps involved in Ba-tagging. . . . 17
1.10 Multi-phase Canadian Ba-tagging scheme. . . . 18

2.1 The ISAC facilities at TRIUMF. . . . 23
2.2 A schematic of the SEBT beamline. . . . 23
2.3 The Ba-tagging apparatus at TRIUMF. . . . 25
2.4 Engineering rendering of the beam window mount. . . . 26
2.5 Gas handling system of the Ba-tagging setup. . . . 27
2.6 The saturation curve for xenon. . . . 28
2.7 A cross section view of the LXe cell. . . . 29
2.8 A close view of the probe. . . . 30
2.9 Stopping ranges for ^{139}Cs in LXe. . . . 31
2.10 The decay scheme of ^{139}Ba. . . . 33
2.11 The γ-ray spectrum of ^{139}Ba and ^{139}Cs. . . . 34
2.12 Stopping ranges of ^{139}Cs in various media. . . . 35

3.1 Electric potential (V) in simplistic model. . . . 38
3.2 Electric field (V/m) . . . 39
3.3 Singly charged ^{139}Ba trajectories in liquid xenon. . . . 39
3.4 Geometries of the COMSOL simulations . . . 41
3.5 Electric potential around biased probe tip. . . . 43
3.6 The electric field around the probe tip in LXe. . . . 44
3.7 LXe pressure field with creeping flow. . . . 48
3.8 LXe velocity field with creeping flow. . . . 48
3.9 Enlarged velocity field map for LXe with creeping flow. . . . 49
3.10 LXe pressure solution with laminar flow . . . 50
3.11 LXe velocity solution with laminar flow . . . 50
3.12 $^{139}Ba^{+}$ ions in LXe travelling towards a biased probe tip. . . . 54

3.13 Simulated Ba ion mobility for various ion sizes. 56
3.14 Ion Distribution A. 57
3.15 Distribution A in context of simulation. 58
3.16 Extraction efficiency vs. time for various probe biases. 59
3.17 Electric field and ions' final position on probe. 60
3.18 Extraction efficiency vs time for various probe biases. 60
3.19 Electric field for flat cylindrical probe. 62
3.20 The extraction efficiency as a function of time for three different probe types. 63
3.21 Rounded probe in Model A, after running simulation with Distribution A. 64
3.22 The extraction efficiency for various probe depths. 64
3.23 The boundaries for the four groups of particles within Distribution A. . . 66
3.24 Three views of successful Distribution A particles. 67
3.25 Ba ions at probe tip classified by their (+) initial position. 68
3.26 Ba ions at probe tip classified by their (-) initial position. 68
3.27 All successful Ba ions at probe tip. 69
3.28 Number of ions extracted originating in each quadrant. 70
3.29 Effect of currents on extraction efficiency. 71
3.30 A SRIM particle distribution of 100 $^{139}Ba^{+}$ ions. 72
3.31 Ion cloud distance vs time in LXe. 73
3.32 The collection time to achieve 100 % efficiency vs the ionic diameter. . . . 74
3.33 The reduced mobility of $^{138}Ba^{1+}$ ions drifting in GAr. 76
3.34 Electric field solution of Model B. 77
3.35 Trajectories of 100 Ba ions in GAr. 77
3.36 Ion cloud distance vs. time for various probe biases in GAr. 78
3.37 Ion cloud distance vs. time for various probe biases in GXe. 79
3.38 Ion cloud distance vs. time for various probe biases in LAr 79
3.39 Electric potential and fluid velocity map of LXe. 81
3.40 Ion Distribution C. 82
3.41 Final locations of Ba ions on the probe tip. 82
3.42 The simulated trajectories of 15,000 $^{139}Ba^{1+}$ ions in GAr. 83

A1.1 The saturation curve for Ar. The red diamond denotes the triple point. . 87
A1.2 Saturation curve for Ar. 88
A1.3 The decay series for ^{139}Cs after 4 hours. 89

A2.1 Beamline and accelerator network for the ISAC experimental halls. 91

A3.1 Extraction efficiency of Ba in LXe for probe biases. 93

List of Tables

1.1 Mixing angles compiled from various neutrino oscillation experiments. . . 5
1.2 The measured $2\nu\beta\beta$ decay half-lives for several isotopes. 8
1.3 The current experimental limits of various $0\nu\beta\beta$ searches. 9

2.1 Boiling and melting points of Xe, Ar, and Kr. 28
2.2 Radioactive isotopes and their respective half lives available at TRIUMF. 34

3.1 Common liquid xenon fluid parameters for COMSOL simulation purposes. 45
3.2 Ion mobility values from literature for $^{139}Ba^{1+}$ in various media 75
3.3 Results for Ba ion simulations in GAr. 80

Declaration of Authorship

I, Megan Cvitan, declare that this thesis titled, "Simulating barium ion motion in liquid xenon for a future barium tagging upgrade of nEXO" and the work presented in it are my own, unless otherwise specified in-text.

Figure 2.12 in Chapter 2 was created by Dr. Dwaipayan Ray.

The GEANT4 simulations of Ge detector studies were performed by Lucas Backes and Iroise Casandjian.

For Matia and Daniel

Chapter 1

Theoretical background

1.1 Neutrinos

The neutrino is one of the most abundant elementary particles in the Universe, and plays important roles in proposed answers to many frontier scientific questions, such as why the Universe is composed almost entirely of matter rather than anti-matter [1], and by what mechanism and processes do massive stars end their lives in supernova explosions [2, 3]. Nevertheless, some of the neutrino's most basic properties remain poorly understood. In particular, the neutrino's mass influences how the neutrino interacts with matter, which in turn affects the role of neutrinos in the Cosmos. The existence of the neutrino's mass and neutrino oscillation (see Section 1.2) was established by the 2015 Nobel Prize-winning research carried out at the Sudbury Neutrino Observatory and Super-Kamiokande [4, 5, 6]. The actual neutrino mass value, however, is presently unknown and its origin remains one of the biggest questions in particle physics.

Neutrinos are weakly interacting elementary particles with no electric charge; they are currently classified as leptons because of their half-integer spin nature, according to the Standard Model of Physics [7]. The neutrino was first proposed by Wolfgang Pauli in 1930 to explain the continuous energy spectrum in beta decays [8]. He suggested that this particle could carry the missing energy and angular momentum, explaining the discrepancies between the initial and final states of the decay. Originally named the "neutron", the neutrino was postulated to be electrically neutral and of similar mass to that of an electron in order to obey conservation laws, and also to speculate on why it was so difficult to detect.

In 1934, Enrico Fermi renamed the particle to its current name while presenting the now-recognizable theory of beta decays [9]. The nucleus was already conceptualized as bound states of protons and neutrons, where neutrons could undergo a decay resulting in a proton, electron, and antineutrino, as shown in Equation 1.1. At this time, the neutrino was believed to have no rest mass.

$$n^0 \rightarrow p^+ + e^- + \bar{\nu}_e \tag{1.1}$$

The first direct experimental detection of neutrinos was in 1956 by the Cowan-Reines neutrino experiment [10]. Cowan and Reines measured the (then hypothetical) electron antineutrino flux from a nearby nuclear reactor through inverse beta decay, using large water tanks as their detector. Throughout the 1960s, the nature of the neutrino continued to be a popular area of research. It was later discovered in 1962 that there was more than one type of neutrino, beginning with the muon neutrino [11]. An intense proton beam was accelerated onto a beryllium target to produce pi-mesons, which decayed and resulted in a collimated beam of muons and neutrinos. These neutrinos were then detected in a large spark chamber.

In 1975, the tau lepton was discovered [12] and it immediately implied the existence of the tau neutrino. The tau neutrino was later found at Fermilab by the DONUT collaboration in 2000 [13]. It was, therefore, accepted that in nature there are three distinct neutrino flavours: ν_e, ν_μ, and ν_τ, each corresponding to a respective lepton with which they weakly interact.

The infamous solar neutrino problem, discovered in the mid-1960s by the Homestake experiment, presented an inconsistency between the flux of solar neutrinos as calculated from the Sun's luminosity and as measured directly [14]. The solar neutrino flux as theoretically calculated by John Bahcall were consistently three times larger than the value measured by the Homestake experiment, lead by Raymond Davis [15]. It was found that both approaches were correct, except Davis' chlorine-based detector was only sensitive to one kind of neutrino out of the three possible types. Steps towards solving this discrepancy required an update to the (then accepted) Standard Model around 2002 [16]. It was then postulated that the three neutrino flavours each had slightly different mass values, and that the neutrino mass is a mixture of these three mass eigenstates. In addition, the neutrinos could change flavour eigenstates as they travelled to Earth from the Sun, giving rise to the process known as neutrino oscillation. The solar neutrino problem remained unsolved for about 30 years, until the discovery of solar neutrino oscillations in 2001 at the Sudbury Neutrino Observatory (SNO) [5]. This discovery was in support of the detection of atmospheric neutrino oscillation by Super-Kamiokande a few years prior in 1998 [6].

1.2 Neutrino Oscillations and Neutrino Mass

Neutrino oscillations are only possible if the lepton flavour numbers (L_e, L_μ, L_τ) are not conserved by the neutrino mass term, that is if $\Delta L_x \neq 0$. During the process of neutrino oscillation, a neutrino changes its flavour eigenstate between ν_e, ν_μ, and ν_τ. The neutrino flavour eigenstates (ν_e, ν_μ, ν_τ) and mass eigenstates (ν_1, ν_2, ν_3) are related by a unitary transformation matrix U as follows:

$$\begin{bmatrix} \nu_e(t) \\ \nu_\mu(t) \\ \nu_\tau(t) \end{bmatrix} = U \begin{bmatrix} \nu_1(t) \\ \nu_2(t) \\ \nu_3(t) \end{bmatrix} \tag{1.2}$$

This mixing matrix U is known as the Pontecorvo-Maki-Nakagawa-Sakata (PMNS) matrix [17]. Evidently, the flavour and mass eigenstates would be equal if this matrix was an identity operator, but this would not correspond to experimental findings. The PMNS matrix is given by

$$U = \begin{bmatrix} U_{e1} & U_{e2} & U_{e3} \\ U_{\mu 1} & U_{\mu 2} & U_{\mu 3} \\ U_{\tau 1} & U_{\tau 2} & U_{\tau 3} \end{bmatrix}, \tag{1.3}$$

where it can be represented as a product of three rotation matrices, resulting in

$$U = \begin{bmatrix} c_{12}c_{13} & s_{12}c_{13} & s_{13}e^{-i\delta} \\ -s_{12}c_{23} - c_{12}s_{23}s_{13}e^{i\delta} & c_{12}c_{23} - s_{12}s_{23}s_{13}e^{i\delta} & s_{23}c_{13} \\ s_{12}c_{23} - c_{12}s_{23}s_{13}e^{i\delta} & -c_{12}c_{23} - s_{12}s_{23}s_{13}e^{i\delta} & c_{23}c_{13} \end{bmatrix} P. \tag{1.4}$$

The terms c_{ij} and s_{ij} represent $\cos(\theta_{ij})$ and $\sin(\theta_{ij})$, where θ_{ij} is the mixing angle, and δ is the Dirac CP-violating phase [18]. The matrix P is either the 3x3 unit matrix for Dirac neutrinos, or carries the Majorana CP phases α_1 and α_1 as in Equation 1.5.

$$P = \begin{bmatrix} 1 & 0 & 0 \\ 0 & e^{i\alpha_1/2} & 0 \\ 0 & 0 & e^{i\alpha_2/2} \end{bmatrix} \tag{1.5}$$

The neutrino mass matrix M_ν can be found through a congruence relation involving the PMNS matrix, since U is invertible.

$$M_\nu = U \begin{bmatrix} m_1 & 0 & 0 \\ 0 & m_2 & 0 \\ 0 & 0 & m_3 \end{bmatrix} U^T, \tag{1.6}$$

The diagonal elements in the central matrix are the neutrino masses corresponding to their respective mass eigenstates. The mass eigenstates $|\nu_j\rangle$ can also be expressed by a plane wave solution

$$|\nu_j(t)\rangle = e^{-i(E_j t - \vec{p}_j \cdot \vec{x})}|\nu_j(0)\rangle, \tag{1.7}$$

where the energy of mass eigenstate j, E_j , can be approximated in the ultra-relativistic limit ($|\vec{p}_j| = p_j \gg m_j$) as

$$E_j = \sqrt{{p_j}^2 + {m_j}^2} \approx E + \frac{{m_j}^2}{2E}, \tag{1.8}$$

since it is known that neutrino masses are on the order of eV [19], and their energies are greater than 1 MeV. In Equation 1.8, the term E is the energy of the particle to be detected. Redefining the dependent variable in Equation 1.7, the time parameter, to distance travelled by the particles, and including the approximation for the energy gives

$$|\nu_j(L)\rangle = e^{-i({m_j}^2 L/2E)}|\nu_j(0)\rangle. \tag{1.9}$$

As such, the frequency at which a neutrino propagates depends on the mass in the exponent, where heavier mass eigenstates oscillate faster than lighter ones. Furthermore, since the mass eigenstate can be expressed as a superposition of flavour eigenstates, as in Equation 1.10, the differences in the frequency lead to interference between the corresponding flavour components of a mass eigenstate.

$$|\nu_\alpha(t)\rangle = \sum_{j=1}^{3} U_{\alpha j}|\nu_j\rangle \tag{1.10}$$

By inverting Equation 1.10, and substituting in the time evolved neutrino mass eigenstates from the Schrodinger equation, a superposition of flavour eigenstates can be derived to express the flavour eigenstate at time t:

$$|\nu_\alpha(t)\rangle = \sum_{\beta=e,\mu,\tau}\left(\sum_{k=1}^{3} U_{\alpha k}e^{-iE_k t}U^*_{\beta k}\right)|\nu_\beta\rangle \tag{1.11}$$

This constructive interference gives rise to the possibility of observing a neutrino changing flavours during propagation. With Equation 1.11 and the energy approximation, the probability of oscillation ($\nu_\alpha \to \nu_\beta$) is then represented by

$$P_{\alpha\to\beta} = |\langle\nu_\beta(L)|\nu_\alpha\rangle|^2 \tag{1.12}$$

$$P_{\nu_\alpha\to\nu_\beta} = |\sum_j U_{\beta j}e^{-i{m_j}^2 L/2E}{U_{\alpha j}}^*|^2 = \sum_{j,k} {U_{\alpha j}}^* U_{\beta j}U_{\alpha k}{U_{\beta k}}^* e^{-i\Delta{m_{jk}}^2 L/2E}, \tag{1.13}$$

where the subscripts α and β correspond to two of the three neutrino flavors, and j and k correspond to the mass eigenstates. More conveniently, for a simplified two-neutrino system, the oscillation probability for an electron neutrino with a travelling distance L and kinetic energy E is given by:

$$P_{\nu_e\to\nu_\mu} = \sin^2(2\theta_{12})\sin^2\left(\frac{\Delta m^2 L}{4E}\right). \tag{1.14}$$

This probability equation reveals the length scale for neutrino oscillations, $\mathrm{L} = 4\mathrm{E}/\ \Delta\mathrm{m}^2$: the distance after which a given neutrino is most likely to be found in the muon state

[7]. By measuring neutrinos from a source with a known and constant flavor at a certain distance away, the quantity of neutrinos that had changed state can be determined, and thus Δm^2 may be calculated.

From Equation 1.13, $\Delta {m_{jk}}^2$ is the difference between the squared neutrino masses, ${m_j}^2$ - ${m_k}^2$ [20]. The measured oscillation probability defined above can set bounds on the squared mass differences, but they do not define the order of the hierarchy. From the KamLAND experiment, the magnitude of the squared mass differences between mass eigenstates ν_1 and ν_2 is established, and it is known from atmospheric neutrino experiments that the difference between the ν_3 mass eigenstate and the other two is larger [21]. As a result, there are two possible combinations of neutrino mass orderings denoted by normal ordering ($m_1 < m_2 < m_3$), and inverted ordering ($m_3 < m_1 < m_2$); the ν_3 state is considered either the lightest or the heaviest. Figure 1.1 demonstrates these two possible neutrino mass orderings, and the flavour oscillation dependence on Δm^2_{21}, Δm^2_{31}, and Δm^2_{32} if $\Delta {m_{ij}}^2 = {m_i}^2$ - ${m_j}^2$, i and j = 1,2,3, and i $\neq$ j. The true neutrino mass ordering and absolute mass scale are unknown because it is not possible to determine the sign of the Δm^2_{31} term.

From experiment, the observed number of neutrinos of each flavor can be compared to the number produced to obtain values for the weak mixing angles θ_{12} and θ_{23}. In addition, these measurements can be compared to limits placed on observations of the cosmic microwave background to place a limit on θ_{13}. Solar, atmospheric, and reactor neutrino oscillation experiments have provided us with approximate values for the weak neutrino mixing angles given in Table 1.1 [22]. The mixing amplitude of each mass eigenstate with each weak eigenstate can be determined by substituting these values of θ_{ij} into the PMNS matrix in Equation 1.4. The contribution of each flavour state is also shown in Figure 1.1.

$sin^2(\theta_{12})$	0.846 ± 0.021 [23]
$sin^2(\theta_{13})$	0.093 ± 0.008 [23]
$sin^2(\theta_{23})$	$> 0.92 \pm 0.061$ [24]

TABLE 1.1: Mixing angles compiled from various neutrino oscillation experiments.

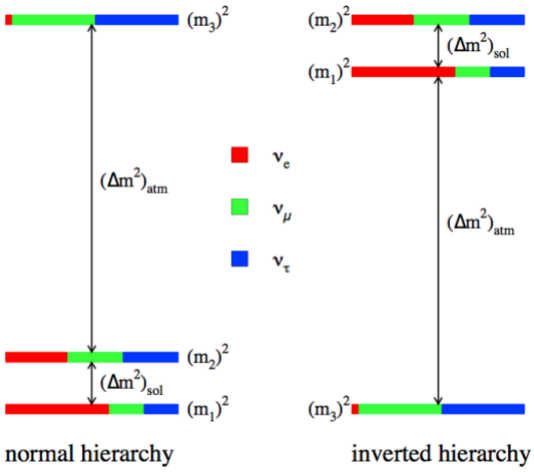

FIGURE 1.1: A visualization of the two possible neutrino mass hierarchies. By the conventional definition if $\Delta m^2_{21} > 0$, normal ordering is in the case where $\Delta m^2_{31} > 0$ (left) and $\Delta m^2_{31} < 0$ depicts inverted ordering (right). Schematic from [25].

Current estimates of the mass differences are approximately 2.44 $\times 10^{-3}$ eV^2 for $|\Delta {m_{atm}}^2|$ and about 7.53 $\times 10^{-5}$ eV^2 for $\Delta {m_{sol}}^2$ [26].

Assuming that the light Majorana neutrino exchange model and the calculations for the nuclear matrix elements are correct, the $0\nu\beta\beta$ discovery potential of next-generation experiments in the case where neutrinos are Majorana particles differs depending on the mass hierarchy. Given these assumptions for all next-generation experiments, in the case of an inverted hierarchy, the discovery probability is 100%; the normal hierarchy discovery probablity is closer to 70% [27].

Thus the observation of neutrino oscillation requires that neutrinos have mass. As previously mentioned, however, the neutrino mass-generating mechanisms are unknown. If Dirac neutrinos acquire their mass through the Higgs coupling, just like other leptons [28], it would still raise questions about why the neutrino mass is comparatively obscurely small to other leptons. For this reason, many believe the neutrino could be a Majorana particle, or its own anti particle, since it would provide an intuitive explanation for this peculiarity, and eliminate the need for observable right-handed neutrinos in the SM. The handedness of neutrinos refers to the relative orientations of spin and linear momentum, which is fixed and intrinsic to the particle. If they exist, the spin and linear momentum of right-handed, or sterile neutrinos, would be in the same direction.

1.3 Neutrinoless Double Beta Decay

There are certain types of isotopes that decay via double beta ($\beta\beta$) decay, which is a rare transition between two nuclei with the same mass number A. In this decay, the atomic number Z changes by two units (N-2, Z+2). The $\beta\beta$ decay occurs only in even-even

nuclei, which are isotopes with even numbers of p^+ and n^0 [29], when the single β decay (n⇒p or p⇒n) to an odd-odd isobar is energetically forbidden or severely suppressed by the angular momentum. Due to the pairing forces, the ground states of an even-even nucleus more tightly bound than their neighbouring odd-odd nuclei. The second order decay, however, into the (Z+2) daughter nucleus is still energetically allowed. The process of $\beta\beta$ decay is presented in Figure 1.2.

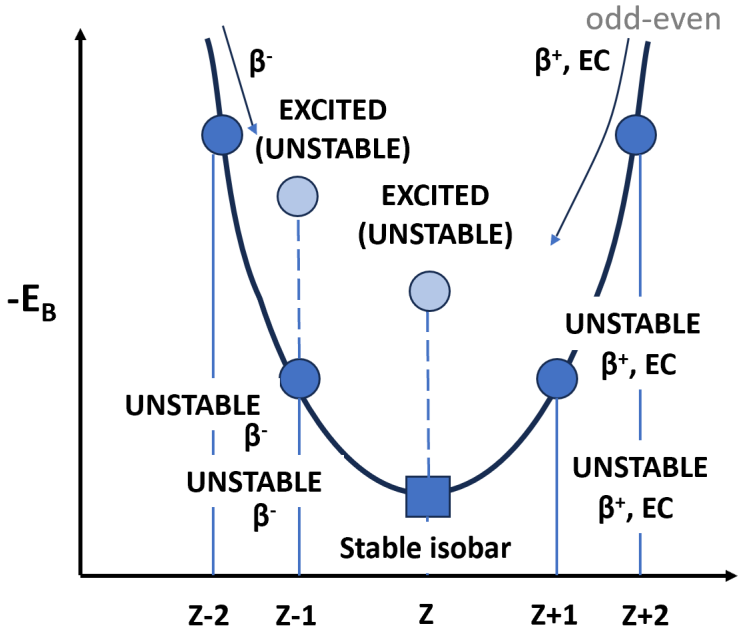

FIGURE 1.2: The mass parabola maps the valley of stability against β-decays. The ground states of even-even nuclei are energetically lower than their (A,Z+1) neighbour. These nuclei only decay into a stable isotope through the emission of two electrons and two neutrinos [29].

The $\beta\beta$ decay is thought to occur through two decay channels: the rare process of two neutrino double beta decay ($2\nu\beta\beta$) given by

$$(A, Z) \rightarrow (A, Z+2) + 2e^- + 2\bar{\nu}_e \tag{1.15}$$

and, if the neutrino were Majorana in nature, neutrinoless double beta decay ($0\nu\beta\beta$), given by

$$(A, Z) \rightarrow (A, Z+2) + 2e^-. \tag{1.16}$$

Both of these decay channels are depicted in Figure 1.3.

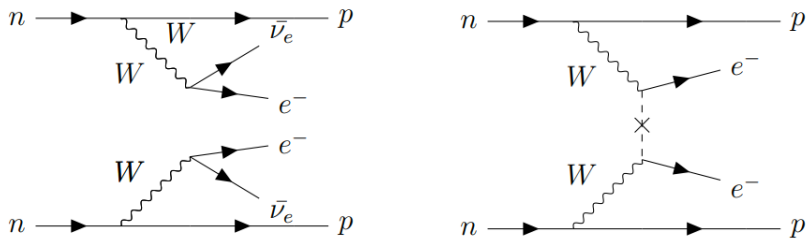

(A) $2\nu\beta\beta$ (B) $0\nu\beta\beta$

FIGURE 1.3: Feynman diagrams for (A) $2\nu\beta\beta$ and (B) $0\nu\beta\beta$, taken from [30]. The difference between the decays lies with the number of electron antineutrinos released.

The $2\nu\beta\beta$ process was first postulated in 1935 by Maria Goeppert-Mayer [31]. It conserves both electric charge and lepton number, and typically occurs between nuclear ground states ($0^+ \rightarrow 0^+$). There are 35 isotopes that could theoretically decay via $2\nu\beta\beta$ decay, but only 14 have been observed experimentally [32, 33, 34, 35]. The decay has been measured for a variety of nuclei: ^{48}Ca, ^{76}Ge, ^{82}Se, ^{96}Zr, ^{100}Mo, ^{116}Cd, ^{128}Te, ^{130}Te, ^{130}Ba, ^{136}Xe, ^{150}Nd and ^{238}U. Table 1.2 shows the $2\nu\beta\beta$ decay half-lives for these listed isotopes. Moreover, the shortest half lives of the $\beta\beta$ decays for these isotopes are on the order of 10^{18} years [36]. Comparatively, the age of the universe is about 1.4×10^{10} years [37].

Isotope	$T^{2\nu}_{1/2}$ [$\times 10^{21}$ years]
^{48}Ca	$0.064 \pm^{0.007}_{-0.006} (stat.) \pm^{0.0021}_{-0.009} (syst.)$ [33]
^{76}Ge	1.926 ± 0.094 [36]
^{82}Se	$0.096 \pm 0.003(stat.) \pm 0.010(syst.)$ [36]
^{96}Zr	$0.0235 \pm 0.0014(stat.) \pm 0.0016(syst.)$ [36]
^{100}Mo	0.00693 ± 0.00004 [36]
	$0.69\pm^{0.1}_{-0.06}$ [36]
^{116}Cd	$0.028 \pm 0.001(stat.) \pm 0.003(syst.)$ [36]
	$0.026\pm^{0.009}_{-0.005}$ [36]
^{128}Te	7200 ± 400 [36]
	1800 ± 700 [36]
^{130}Te	$0.82 \pm 0.02(stat.) \pm 0.06(syst.)$ [34]
^{136}Xe	$2.165 \pm 0.016(stat.) \pm 0.059(syst.)$ [36]
^{150}Nd	$0.00911 \pm^{0.00025}_{-0.00022} (stat.) \pm 0.00063(syst.)$ [36]
	$0.107\pm^{0.046}_{-0.026}$ [36]
^{238}U	2.0 ± 0.6 [36]

TABLE 1.2: The measured $2\nu\beta\beta$ decay half-lives for several isotopes.

If neutrinos were classified as Dirac particles, $2\nu\beta\beta$ would be the only possible decay channel for these isotopes, with no new physics involved. The Majorana neutrino would transform double beta decay events into new opportunities to search for physics beyond

the Standard Model. If the $0\nu\beta\beta$ process exists in nature, it can only occur if the neutrino is its own anti-particle, and consequently violates lepton number conservation. This latter property would imply a unique mechanism for generating the neutrino's mass, thus shedding light on its origin. Since the rate of the decay process is proportional to the effective neutrino mass square, its observation would further offer the possibility to calculate the neutrino mass, provided the nuclear matrix elements associated with the decay process are known.

Since the amplitude of the neutrinoless decay mode is small as a result of the small neutrino mass, it has not been possible to observe the $0\nu\beta\beta$ decay experimentally. The sensitivity limits of the $0\nu\beta\beta$ decay half life, however, are reported to be between 10^{25} and 10^{26} years [38, 39, 40]. There are several large-scale experiments world-wide searching for $0\nu\beta\beta$, and they are all doing so using different isotopes. Some of these past and present isotopes of interest are summarized in Table 1.3, along with their published sensitivity ($T^{0\nu}_{1/2}$ limit assuming a null signal, which depends on detector resolution, background index, and exposure), $T^{0\nu}_{1/2}$ limits (determined by statistics), exposure (the mass of the isotope in use times the duration of data acquisition), and effective Majorana neutrino mass ($m_{\beta\beta}$).

Isotope	Exposure [kg × yrs]	Sensitivity [yrs]	$T^{0\nu}_{1/2}$ [yrs]	$m_{\beta\beta}$ [eV]	Experiment
^{48}Ca		$1.8 \cdot 10^{22}$	$> 1.4 \cdot 10^{22}$	< 3.5 - 22	ELEGANT-VI [41]
^{76}Ge	127.2	$18 \cdot 10^{25}$	$> 1.8 \cdot 10^{26}$	< 0.079 - 0.18	GERDA [38]
	64.5	$> 8.1 \cdot 10^{25}$	$> 8.3 \cdot 10^{25}$	< 0.113 - 0.269	M.D. [42]
^{82}Se		$8 \cdot 10^{23}$	$> 1.0 \cdot 10^{23}$	< 1.8 - 4.7	NEMO-3 [43]
^{82}Se	8.82	$7.0 \cdot 10^{24}$	$> 4.6 \cdot 10^{24}$	< 0.263 - 0.545	CUPID-0 [44]
^{100}Mo	7.369	$2 \cdot 10^{24}$	$> 2.1 \cdot 10^{25}$	< 0.32 0.88	NEMO-3 [43]
^{116}Cd	-	-	$> 1.7 \cdot 10^{23}$	< 1.5 - 2.5	Solotvina [45]
^{128}Te	309.33	$2.2 \cdot 10^{24}$	$> 3.6 \cdot 10^{24}$		CUORE [46]
^{130}Te	1000	$2.8 \cdot 10^{25}$	$> 2.2 \cdot 10^{25}$	< 0.09 - 0.305	CUORE [47]
^{136}Xe		$5.0 \cdot 10^{25}$	$> 3.5 \cdot 10^{25}$	< 0.09 - 0.29	EXO [48]
	970	$1.5 \cdot 10^{26}$	$> 2.3 \cdot 10^{26}$	< 0.036 - 0.156	KamLAND-Zen [49]
^{150}Nd			$> 2.1 \cdot 10^{25}$	< 4.0 - 6.3 eV	NEMO-3 [50]

TABLE 1.3: The current experimental limits (>90% CL) of various $0\nu\beta\beta$ searches. $T^{0\nu}_{1/2}$ and $m_{\beta\beta}$ denote the $0\nu\beta\beta$ half-life and the effective Majorana neutrino mass, respectively.

The $0\nu\beta\beta$ decay rate itself depends on the neutrino's effective Majorana mass, and so a measurement of the rate would determine the actual value of this mass. If this hypothetical process proceeds through light neutrino exchange, the half life for this decay [51] can be represented by

$$\frac{1}{{T_{1/2}}^{0\nu}} = G^{0\nu}|M^{0\nu}|^2 \frac{< m_\nu >^2}{{m_e}^2}. \tag{1.17}$$

In Equation 1.17, $G^{0\nu}$(Q,Z) is the leptonic phase space factor, which varies between isotopes [52], and only depends to the 5^{th} order on the Q-value since less particles than in the 2ν process are emitted. $M^{0\nu}$ is the nuclear matrix element, and $\langle m_\nu \rangle$ is the effective Majorana neutrino mass. More specifically, the nuclear matrix element consists of

$$M^{0\nu} = {g_A}^2 \times {M_{GT}}^{0\nu} - {g_V}^2 \times {M_F}^{0\nu} + {g_A}^2 \times {M_A}^{0\nu}, \tag{1.18}$$

where the terms ${M_{GT}}^{0\nu}$, ${M_F}^{0\nu}$, and ${M_A}^{0\nu}$ are the Gamow-Teller, Fermi, and tensor nuclear matrix elements, as calculated in [53]. The axial and vector coupling constants for the weak interaction are denoted by g_A and g_V, respectively.

Many of these experiments outlined in Table 1.3 employ one common technique in hopes of finding this decay: using large quantities of an active isotope that is known to undergo $2\nu\beta\beta$. If neutrinos are Majorana in nature and $0\nu\beta\beta$ exists, the amount of detected events $N_{0\nu\beta\beta}$ can be estimated by the following:

$$N_{0\nu\beta\beta} = \frac{ln(2) \cdot \alpha \cdot m \cdot N_A \cdot \epsilon_{detector} \cdot t_{live}}{M \cdot T_{1/2}}, \tag{1.19}$$

given a certain detector of mass m with isotopic abundance fraction α. The terms M and N_A are the molar mass (kg) of the decaying isotope employed by the detector, and Avogadro's number (mol^{-1}). $\epsilon_{detector}$ is the detector efficiency towards $0\nu\beta\beta$, t_{live} is the detector's duration of data acquisition, and the half life of $0\nu\beta\beta$ is given by Equation 1.17. By Equation 1.19, it is evident that increasing the quantity of active material in the detector improves the chances of observing this decay event.

The final state of a $2\nu\beta\beta$ decay involves two neutrinos carrying away a portion of the decay's energy–although the neutrinos would not be detected. For $0\nu\beta\beta$, all of the decay energy is encapsulated in the two emitted electrons. This decay energy is called the Q-value. It is an important aspect to consider when choosing the active isotope in a detector, and it can be defined for a $\beta\beta$ decay as

$$Q_{\beta\beta} = M(A, Z) - M(A, Z + 2), \tag{1.20}$$

where M is the mass (in units of kg, of the detector isotope), A is the atomic number and Z is the proton number [54]. Thus, the energy spectrum for the emitted electrons would differ significantly for the two decay modes. Peaks would be observed in different locations depending on the decay; for the $0\nu\beta\beta$ case, at the tail of the curve at the Q value [29]. As an example, the endpoint energy spectrum for the emitted electrons in ^{136}Xe is shown in Figure 1.4. The peaks take the form of a distribution instead of a delta function, considering that the energy collection is governed by Poisson statistics. The total number of detected photons for $0\nu\beta\beta$ decays is distributed around the Q-value [55], since all of the decay energy would have to be carried away by the detected electrons.

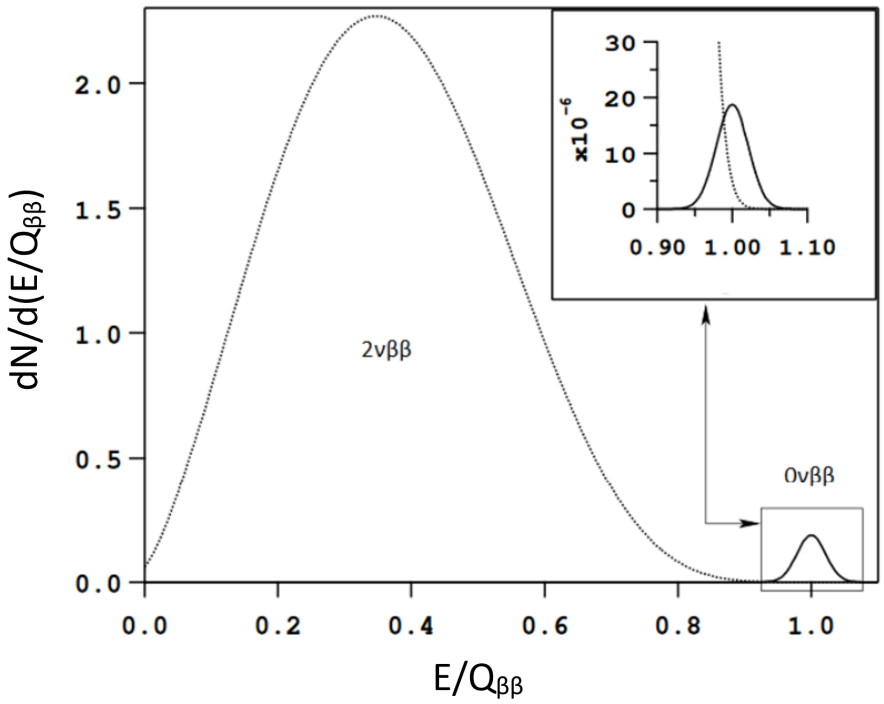

FIGURE 1.4: The decay rate as a function of the fraction of the decay energy for both electrons, normalized for $2\nu\beta\beta$ decays. The small peak located on the tail of the larger curve corresponds to $0\nu\beta\beta$ decays, normalized to 10^{-6} in the inset for emphasis. Adopted from [55].

There are many reasons to consider a monolithic (liquid) ^{136}Xe-based detector. Xe has a natural abundance of 9% but it can be enriched to >80% with centrifuge techniques. It also has a high Q = 2457 keV, in a signal region which can have lower contamination from radioactive background events [56]. Due to its high Z value, a 2.5 MeV γ ray would have an attenuation length of about 9 cm in liquid xenon [57].

^{136}Xe is also known for its special ability to produce scintillation light [58], which can be used to enhance the energy resolution and identify other backgrounds. Lastly, a $\beta\beta$ decay of ^{136}Xe would produce a stable ^{136}Ba ion, allowing for the exciting opportunity to make an unambiguous measurement of a $\beta\beta$ decay. This process is referred to as Ba-tagging, and it is discussed more in sections 1.5 and 2.

1.4 Searching for $0\nu\beta\beta$ with EXO-200 and nEXO

EXO-200 was an experiment searching for $0\nu\beta\beta$ with approximately 175 kg of 80.6% enriched ^{136}Xe in the liquid phase [59]. It was in operation at the Waste Isolation Pilot Plant (WIPP) in New Mexico, USA from 2011 until its decommission in 2018. The detector vessel, seen in Figure 1.5, consisted of a double wall copper cryostat, and the liquid xenon was held in a Time Projection Chamber (TPC) that served as a calorimeter to record the electron energy spectrum [59], location and event multiplicity.

The scintillation light was collected by Large Area Avalanche Photo-Diodes (LAAPDs) located behind wire planes at each end of the TPC. At the time, no evidence of $0\nu\beta\beta$ decay was found and new limits on the half-life and sensitivity were set at 3.5×10^{25} and 5.0×10^{25} at 90% confidence level, respectively [48]. EXO-200 achieved the first experimental observation of $2\nu\beta\beta$ [60], and performed the most precise measurement of the half-life to date for this decay process: $2.165 \pm 0.016(stat) \pm 0.059(syst) \times 10^{21}$ years [59].

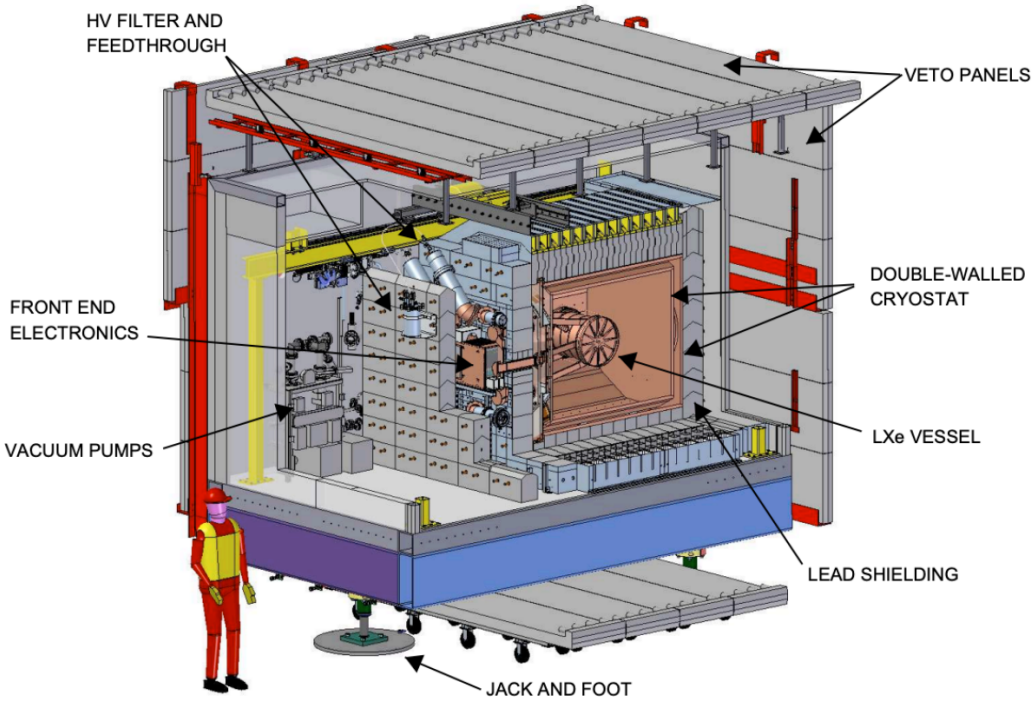

FIGURE 1.5: Artist's rendition of the EXO-200 detector. The experiment was located in an underground clean room in New Mexico, and it searched for $0\nu\beta\beta$ decay using 175 kg of LXe isotopically enriched to 80.6% in ^{136}Xe. The key component of the detector was a LXe time projection chamber (TPC) inside a double-walled Cu cryostat, lead shielding, and a muon veto. The role of the inner cryostat was to keep the xenon liquid, and to shield from background radiation. Taken from [60].

As the successor to EXO-200, the nEXO experiment will search for $0\nu\beta\beta$ decay in 5 tonnes of LXe enriched to 90% [61]. The nEXO detector will be ^{136}Xe-based, which undergoes $\beta\beta$ decay to ^{136}Ba:

$$^{136}\text{Xe} \rightarrow ^{136}\text{Ba} + 2e^- + 2\bar{\nu_e}. \tag{1.21}$$

In the event of a $0\nu\beta\beta$, the above decay equation would omit the two neutrinos. The Q-value for $2\nu\beta\beta$ is 2458 ± 0.31 keV [62], which would be split between the electrons

and the neutrinos, or carried away entirely by the electrons in a $0\nu\beta\beta$ decay.

The nEXO detector design is shown in Figure 1.6. nEXO is a single phase cylindrical Time Projection Chamber (TPC) that will search for $0\nu\beta\beta$ decay through a combination of light and charge readout. The xenon atoms in the TPC are subject to excitation or ionization caused by decay events, which creates excited xenon dimers [63] that decay and emit 175 nm scintillation light. A static electric field will drift the ionization charge to a segmented anode, and scintillation light will be detected by specialized photo-detectors called silicon photomultipliers (SiPMs). Thus, a decay event position can be reconstructed based on the electron drift in LXe and the timing information from the scintillation light signal. The x and y coordinates of a position can be found by the location of the charges at the charge collecting tiles at the anode, and the z coordinate is found by comparing the electrons' time of arrival on the anode with the scintillation light signal from the SiPMs.

These detection techniques will take place in the TPC (copper-coloured), at the centre of the diagram in Figure 1.6; it will contain the 5 tonnes of LXe, which will be surrounded by the inner cryostat vessel full of refrigerant (HFE 7000) to maintain the xenon at liquid phase at about 168 K. The outer cryostat encapsulates the TPC and inner cryostat within a vacuum environment. The 12.3 m outer detector then shields the system from external radiation, namely γ backgrounds, and serves as a muon veto through the use of photomultipliers (PMTs) [61].

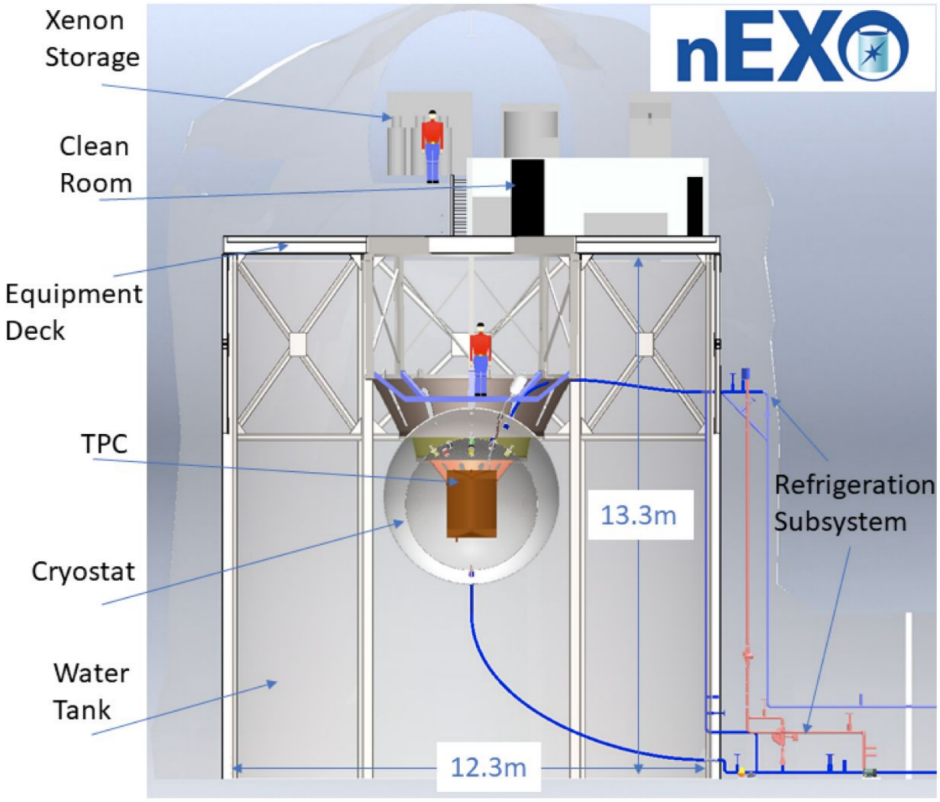

FIGURE 1.6: Artist's rendition of the nEXO experiment that is planned for construction ∼2 km underground at SNOLab, in Sudbury, Ontario, Canada. Shown is the TPC containing LXe within the inner cryostat, nested inside the outer cryostat and the outer detector to protect from external radiation. The SNOLab cryopit is the ideal site for the experiment, given a very low muon rate of 0.27 muon/day/m^2 [64]. Picture taken from [65].

After 10 years of detector livetime, the half-life sensitivity for nEXO is projected to be 1.35×10^{28} years (90% CL), and the 3σ discovery potential is calculated to be 0.74×10^{28} [66], as demonstrated in Figure 1.7. Using Equation 1.17, this sensitivity estimates an effective Majorana neutrino mass < 15 meV. nEXO will be able to explore the entire inverted hierarchy parameter space, since this mass range is less than the parameter space for most nuclear matrix elements. In the case of normal mass ordering, there is also a significant possibility to discover $0\nu\beta\beta$ as the nEXO half-life sensitivity is increased by more than two orders of magnitude compared to existing experiments.

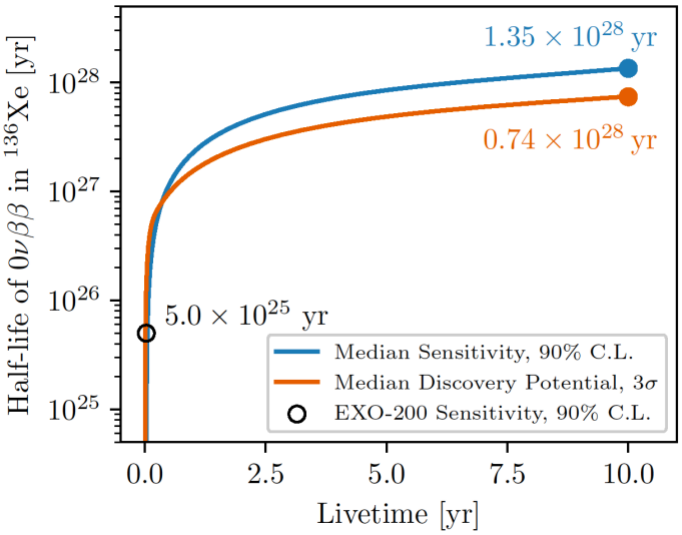

FIGURE 1.7: The nEXO sensitivity and discovery potential as a function of detector livetime [67]. The projection includes an updated 2021 background model with reduced radioactivity.

The $0\nu\beta\beta$ sensitivity of nEXO is nonetheless limited by background signals that contribute counts to the region of interest, most of which are derived from long-lived radionuclides, cosmogenically-activated radionuclides, neutrino-induced backgrounds, and radionuclides from (α,n) reactions. The energy spectra of these background radiation sources overlap with the $Q_{\beta\beta}$ value of the $\beta\beta$ decay in ^{136}Xe.

Several steps are taken to minimize the amount of radionuclides inside the detector, such as improvements in the materials used and using an open field cage to minimize the amount of cage material. However, it is difficult to completely reject all backgrounds. To combat these irreducible background contributions, a background rejection technique called Ba-tagging is under development as a potential future upgrade to the nEXO detector.

1.5 Ba-tagging for a Future $0\nu\beta\beta$ Decay Experiment

A challenge in the search for $0\nu\beta\beta$ is the suppression of background events. In future upgrades of the nEXO detector, there may be a possibility to essentially completely suppress background events, except those from $2\nu\beta\beta$, by extracting and identifying the ^{136}Xe-decay daughter nucleus ^{136}Ba. This process is referred to as Ba-tagging, and is based on a concept introduced in the early 1990s by M. Moe [68]. An event of interest in the detector volume is considered a possible $0\nu\beta\beta$ decay candidate only if ^{136}Ba is identified because gamma-background events do not produce ^{136}Ba.

Figure 1.8 shows the projected nEXO sensitivity as a function of different background rates in the inner 2 tonnes of LXe. The $2\nu\beta\beta$-only background, denoted in Figure 1.8,

demonstrates the sensitivity of nEXO in a 100% efficiency Ba-tagging scenario, assuming that Ba-tagging separates all $\beta\beta$ events from gamma-background events. In this scenario, the sensitivity could be increased by a factor of 2-3 compared to the baseline models, denoted by the red curve in Figure 1.8. To reach the same detector sensitivity as with Ba-tagging, a significant increase in the detector mass would be required.

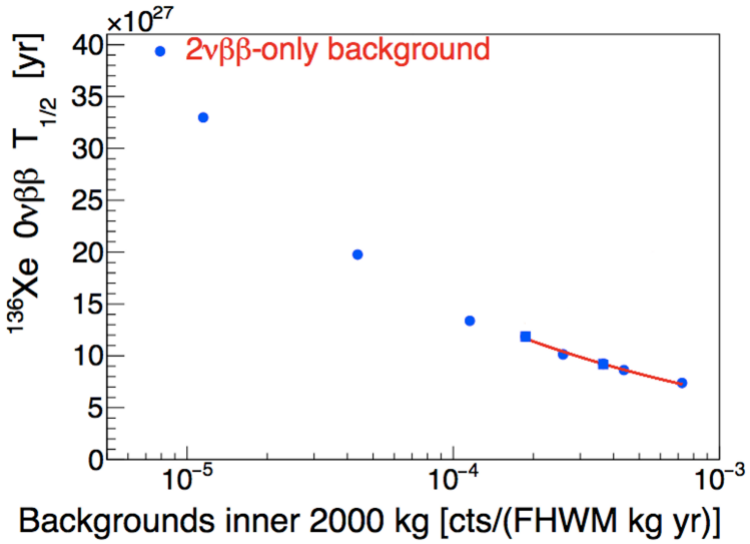

FIGURE 1.8: Plot of the nEXO detector sensitivity to $0\nu\beta\beta$ half-lives as a function of different background models in the inner-most 2 tonnes of liquid xenon over 10 years of data-taking [66].

Ba-tagging would allow for the possibility to unambiguously identify a candidate $0\nu\beta\beta$ as a true $\beta\beta$ decay. In essence, this technique acts as a method of independent identification of an event as a $\beta\beta$ decay.

There are four main steps in the process of Ba-tagging outlined in a flow chart in Figure 1.9. When a possible $0\nu\beta\beta$ event is detected, the position of the decay within the detector is located in Step I. A small volume surrounding the event location is extracted from the detector to search for the daughter nucleus ^{136}Ba in Step II. In Step III, if there is a ^{136}Ba ion present in this small volume of liquid xenon, it is then separated from the residual LXe that was removed from the detector volume along with the Ba. Whether Step III is needed or not depends on the technologies used in the subsequent and prior steps. In Step IV, the isolated ^{136}Ba is identified. The presence of ^{136}Ba at the location of a $\beta\beta$-like event inside the detector will provide conclusive proof for excluding all non-$\beta\beta$-decay backgrounds. Step I in Figure 1.9 has been established by EXO-200, where decay events were localized within a few millimetres [69].

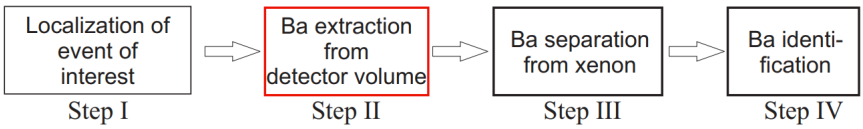

FIGURE 1.9: Overview of conceptual steps involved in Ba-tagging. This thesis focuses on the development of Step II (highlighted in red).

Identification approaches (Step IV) for various forms of Ba have been previously demonstrated, such as Ba^{+} trapped in vacuum [70], Ba^{-} atoms trapped in a Xe-ice matrix [71], and Ba^{++} with Single Molecule Fluorescence Imaging [72]. The Ba-tagging technique relies on the fluorescence of the Ba+ ion. This unique property of ^{136}Ba+ was applied in the early development of imaging trapped ions dating from the 1980s using laser spectroscopy [73]. In these early studies, two lasers are aimed at trapped ^{136}Ba+ ions in order to excite the ground state ($\lambda = 493.545$ nm), but prohibiting the ion from reaching a meta-stable state ($\lambda = 649.869$ nm) [70]. Thus, laser spectroscopy of ^{136}Ba is well-established.

The only remaining step that needs to be demonstrated experimentally is the extraction of ^{136}Ba from a volume of its parent isotope ^{136}Xe. The nEXO collaboration is investigating two main extraction approaches (Step II). One method involves inserting a cryoprobe inside the LXe volume, whereas a capillary tube is used in the other. The cryoprobe approach is pursued by researchers at Colorado State University [71]; it consists of trapping a Ba-ion in a Xe ice matrix frozen to the tip of the probe. The capillary approach is studied by a number of Canadian groups, and it involves ion extraction, from liquid to gas phase using a capillary tube, being developed at Carleton University, followed by separation of Ba-ion from the accompanying Xe and identification, being developed at McGill University. It is currently unknown which of these extraction methods will be exclusively used in the final Ba-tagging scheme. For the demonstration of Ba-extraction from LXe– using either the cryoprobe or the capillary tube approaches– a single-Ba-ion source is required. This thesis focuses on simulations of an accelerator-driven radioactive Ba-ion source using rare isotope beams (RIBs) from the TRIUMF-ISAC facility. The apparatus is described in Chapter 2.

A diagram of the entire Ba-tagging scheme using the capillary approach is shown in Figure 1.10 [74]. It begins with the extraction of ions from the location of a possible $0\nu\beta\beta$ decay signal.

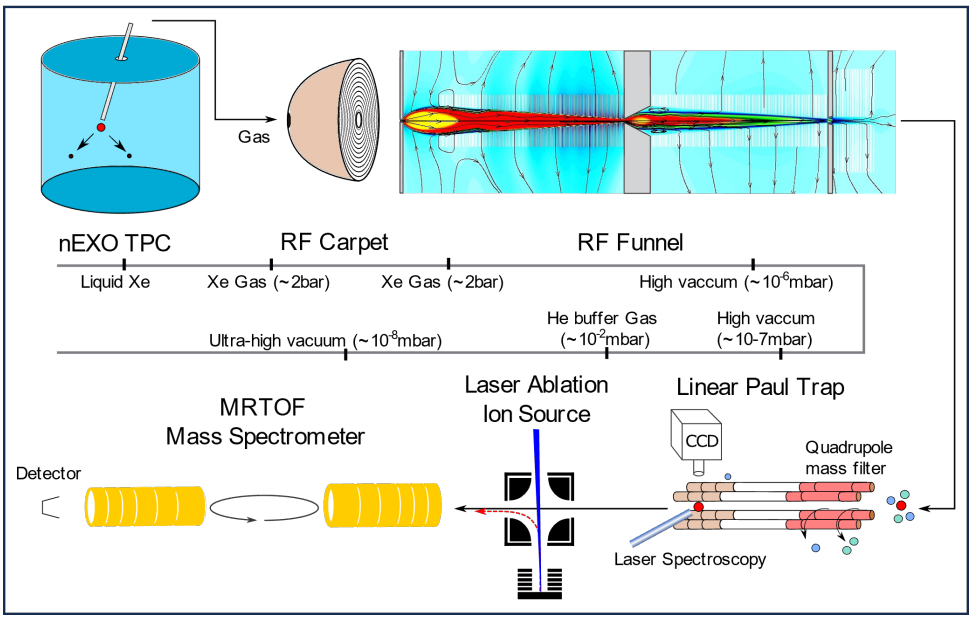

FIGURE 1.10: Multi-phase Canadian Ba-tagging approach, as outlined in [75]. The $^{136}Ba^{+}$ is extracted from the TPC, along with some LXe. An RF carpet guides the $^{136}Ba^{+}$ ion into the RF-funnel, bringing the ion from high pressure to a high vacuum environment. The $^{136}Ba^{+}$ is directed to a linear Paul trap, where it could be identified via laser fluorescence spectroscopy, prior to being transferred to a mass spectrometer to measure its mass.

The capillary will be moved into the TPC to extract a small volume of LXe from the detector volume from the location of a $0\nu\beta\beta$ signal. The extracted detector volume phase transitions from liquid to gas, while containing the $^{136}Ba^{+}$ inside it. A singly charged Ba is expected because the Ba^{2+} is expected to undergo electron exchange with xenon [68]. At this stage, the Ba ion is in the xenon gas, which is kept at pressures of (1-10) bar. Next, an RF-only ion funnel transports the ion from high pressure ($\approx$ 10 bar) to vacuum ($\approx 10^{-6}$ mbar) [76].

An RF carpet is under development; it will allow the ions to enter the funnel. The RF carpet guides the ions towards the central axis using optimized RF potential and electrode geometry. The ^{136}Ba+ moves to the linear Paul trap. Here, the ions are trapped, and element-specific identification is performed using laser fluorescence spectroscopy. Then, the $^{136}Ba^{+}$ ion is transported downstream to a multiple-reflection time-of-flight mass spectrometer (MRTOF-MS) to measure its mass to a high precision and accuracy [77].

1.6 Ion Mobility in Noble Gases

Understanding ion mobility in liquid xenon is key to the development of efficient Ba-ion extraction methods. Ion mobility refers to the differential speeds at which ions migrate through a medium under the influence of an electric field [78]. In addition to the effect

of the ion's mass and charge, the mobility is also influenced by the temperature and density of the medium through which it propagates. Specifically, this property becomes relevant when simulating charged particles in liquid xenon. It is crucial to understand loss mechanisms for our setup to demonstrate extraction efficiencies and ultimately, we need to know precise locations of the ions in the nEXO TPC, where mobility will play a role as well.

Much of our understanding of ion mobility comes from the study of ion transport in gases [79, 80]. The theory of ion mobility spectroscopy (IMS) is summarized in this section, as it applies to singly charged ions in noble gases in low electric fields.

An ion distribution of n_i ions (molm^{-3}) for a single species i disperses through a noble gas medium by diffusion– the main force exerted on the ions. Naturally, the ions move from high concentration to low concentration regions until all ions are uniformly dispersed. In order for the diffusion to be the dominant force on the ions, there are four main conditions that must hold true:

1. There must be no temperature gradient.
2. The density of the ions must be low enough to neglect Coulomb repulsion.
3. There must be no electric or magnetic fields.
4. There cannot be any chemical or charge transfer reactions occurring.

This ion flux[1]($\mathrm{molm}^{-2}\mathrm{s}^{-1}$), J, due to diffusion is defined by Fick's first law, where J is proportional to the magnitude of the concentration gradient ∇n_i–that is, the first derivative of the concentration for ideal mixtures [81]:

$$J = -D|\nabla n_i| \tag{1.22}$$

The constant D, the ion diffusion ($\mathrm{m}^2\mathrm{s}^{-1}$), is a joint property of the ions and the gas medium through which the motion proceeds. The velocity of these ions, which is the velocity of the diffusive flow, is represented by v, as given by $J = n_i v$. As such, Equation 1.22 can be modified to find an expression for the velocity:

$$v = -\frac{D}{n_i}|\nabla n_i| \tag{1.23}$$

By applying a weak uniform electric field in the gas, the ions begin to flow along the field lines. This ion motion is superimposed on the diffusive motion in the gas. The average velocity of the ions, v_d, is also called the drift velocity. The drift velocity is directly proportional to the electric field E; an increase in the electric field strength increases the drift velocity.

[1] For simplicity, the magnitudes of the flux, velocity, and field vectors are used.

$$v_d = K \cdot E \tag{1.24}$$

The coefficient K is the ion mobility, and it is also a joint property of the ions and the gas through which they diffuse. The ion mobility is essentially a measure of friction linked to the time that it takes the ions to traverse a certain distance. The ion flux can now be reformulated to

$$J = n_i K \cdot E - D|\nabla n_i|. \tag{1.25}$$

The relation between, D, and the weak-field ion mobility, K, for singly charged ions is given by the recognizable Nernst-Townsend-Einstein equation [79]:

$$K = eD/k_B T, \tag{1.26}$$

where k_B is the Boltzmann constant, e is the electron charge, and T is the temperature of the gas. Equation 1.26 is generally true for systems near equilibrium; that is, if the field and the concentration gradients are small. This equation is valid for dilute and dense gases, as well as liquids and isotropic solids [80]. The ion mobility can be found from a measurement of the ion drift time t_d, as expressed by

$$t_d = \int_S ds/v_d(s) = \frac{1}{K}\int_S ds/E(s), \tag{1.27}$$

where $v_d(s)$ is the instantaneous ion drift velocity along a trajectory S, in a weak field $E(s)$.

To compare results of ion mobility from different experiments, the mobility can be expressed as a function of the parameter E/n, where n is the number density of the drift gas atoms. This parameter considers the experimental conditions during a measurement, and characterizes the average ionic energy acquired from the electric field. It is generally expressed in units of Townsends, where 1 Td = $10^{-21}\ Vm^2$. The ion mobility is inversely proportional to the number density of the gas medium atoms; it is typically converted to the reduced mobility K_0, defined by

$$K_0 = K \cdot \frac{P}{P_0} \cdot \frac{T_0}{T}, \tag{1.28}$$

where P_0 is the standard pressure, 760 Torr, and the standard temperature T_0 is 273.16 K. The gas pressure and temperature P and T are the conditions at which the mobility K was calculated. However, the reduced ion mobility is not a constant, as it depends on the E/n ratio:

$$K_0\left(\frac{E}{n}\right) = K_0(0)\left[1 + \alpha_2\left(\frac{E}{n}\right)^2 + \alpha_4\left(\frac{E}{n}\right)^4 + ...\right] \tag{1.29}$$

The low-field limit is when E/n is small enough where K_0 is independent of E/n. This condition generally remains true for E/n values below ≈ 2 Td [82].

The reduced ion mobility also depends on the collision frequency, which is linked to all of the other parameters already introduced such as T, P, and n. In cases where the drift velocity v_d is small compared to the ion thermal velocity v_T, the mobility can be expressed as [83]:

$$K_0 = \frac{3}{16}\sqrt{\frac{2\pi}{\mu k_B T}}\frac{Ze}{n\Omega}, \tag{1.30}$$

where μ is the reduced mass of the ion-gas pair, denoted by $\mu = \mathrm{mM}/(\mathrm{m+M})$, and m and M are the ion and gas particle masses. The Ze term corresponds to the charge of the ion. From kinetic theory, the collision cross section term, Ω, represents the momentum transfer integral between the ion and gas particles averaged over all gas-ion relative v_T [84]. As a result, a value for this experimental "cross section" can be obtained through measuring K_0. This integral is generally difficult to calculate theoretically unless a rigid sphere model is used, where it is equal to the projection cross section [85]. The details of this integral representation are inconsequential for simulation developments; derivations of the collision cross section with a rigid sphere model are described by Ref. [86].

A process that affects ion mobility, and is involved at the forefront of performing particle simulations, is ion cluster formation. Clusters are composed by a central ion with one or more neutral atoms or molecules, bound together by charge induced dipoles [87], consequently changing the effective radius of the ion in question. The size of a cluster has implications on the drift velocity of the ions, and it is also pressure dependent [88]. This concept of electrostriction becomes increasingly important when simulating Ba ions in noble gas and liquid media, and is later discussed in Section 3.

Chapter 2

Methodology and Apparatus

2.1 Radioactive Ion Beams at TRIUMF

Situated in Vancouver, British Columbia, TRIUMF stands as Canada's premier particle accelerator centre, facilitating rigorous research across a spectrum of disciplines [89]. Its mandate spans critical domains such as particle physics, nuclear physics, nuclear medicine, materials research, and the advancement of accelerator and detector technologies. At the core of TRIUMF, facilitating such research, is the 520 MeV H^- cyclotron, which possesses the capacity to simultaneously deliver multiple proton beams at distinct energies for a range of experiments [90]. The cyclotron provides beams for the Isotope Separator and Accelerator (ISAC) target stations. The ISAC facilities, shown in Figure 2.1, host various experiments dedicated to research with radioactive ion beams (RIBs) [91].

The process of ion beam generation leading up until the ISAC facility is outlined below. It starts with a source of H^- ions that are delivered to the cyclotron to be accelerated. Thin graphite foils are placed at various radii of the cyclotron to strip the two electrons off of the H^-, leaving a bare proton beam, which is then led out of the cyclotron to the beamlines. Beam line 2A supplies ISAC facilities with 500 MeV proton beams up to currents of 100 μA [91], made by the Isotope Separator On-line (ISOL) method. At TRIUMF, the ISOL method is capable of producing the desired exotic nuclei by aiming a high energy proton beam at thick high power targets to induce spallation and fragmentation reactions [92].

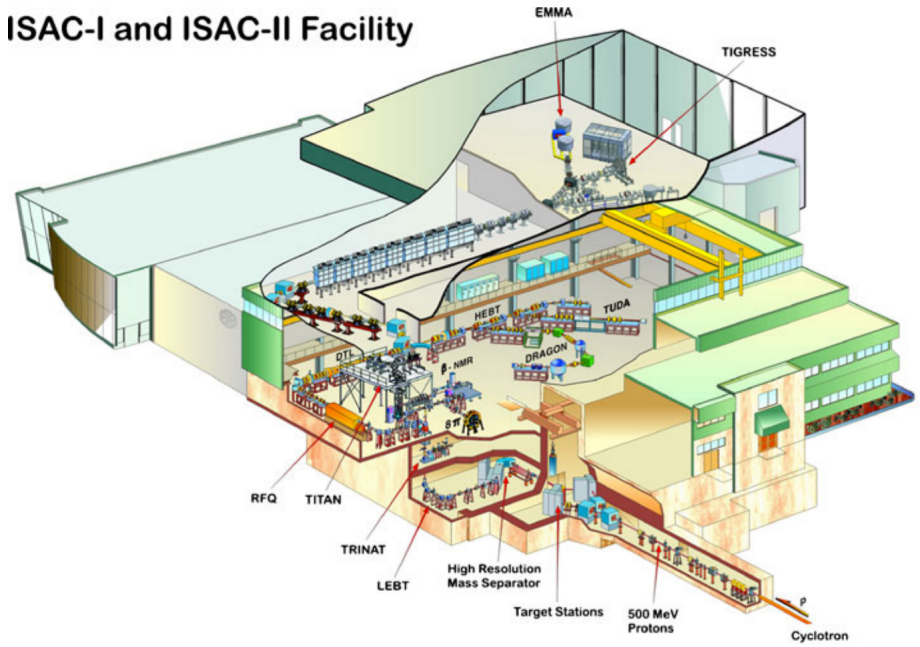

FIGURE 2.1: The ISAC facilities at TRIUMF, highlighting some of the many experimental setups accommodated there. Figure from [91].

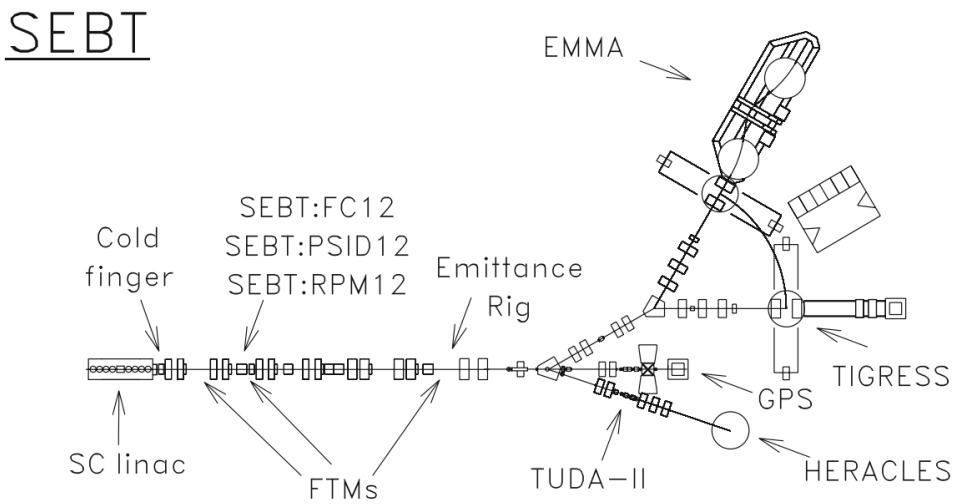

FIGURE 2.2: A schematic of the SEBT beamline, from the superconducting (SC) linac to experiments EMMA, TIGRESS, and TUDA-II, which is an external user beamline (SEBT-I). This section of the entire beamline is also in Figure 2.1, at the top of the image. The Ba-tagging apparatus is located where the HERACLES (shown) once was. Image courtesy of [93].

Proton beams with 500 MeV energies are sent to the ISAC target stations, and they impinge on a target at the RIB target station is shown in Figure 2.1. The target is made

of several disks (stacked), inside which stable and radioactive isotopes are produced. The reaction products quickly diffuse to the surface of the target and evaporate. The isotopes are guided to an ion source to become ionized before being directed to ISAC experiments. There are various different ion sources available: a surface ion source, a laser ion source called the TRIUMF Resonant Ionization Laser Ion Source (TRILIS), and a plasma ion source named the Forced Electron Beam Induced Arc Discharge (FEBIAD) [91]. The RIB is extracted and separated based on mass-to-charge ratio m/q and velocity v by a high resolution magnetic mass-separator. The ions are guided through the magnet at different radii, $r = mv/qB$, and are spatially separated with a resolving power of $m/\delta m \approx 2500$ [94]. At this stage, the RIB is delivered to either the ISAC-I or ISAC-II experimental halls. The Ba-tagging apparatus is located in ISAC-II at the end of the SEBT-I beam line, depicted in Figure 2.2. After the mass-separator, the RIB goes through an RFQ and then to the drift tube linac before the final acceleration stage by the superconducting linac to ISAC-II, where it is distributed to experiments with high beam energy requirements.

The ISAC yield station determines the isotope species in the beam by taking a decay spectroscopy measurement to determine the half lives of the beam constituents. This step occurs before every experiment during the setup shifts, and it is important for determining any contaminant isotope species. In the future, when ARIEL-CANREB is available for RIB production using an electron beam ion source (EBIS) for ISAC-housed experiments, the beam would be sent to an almost identical yield station in the ARIEL facility.

2.2 Barium Tagging Apparatus at TRIUMF

In this section, the multi-phase experimental approach and details of the experimental setup at TRIUMF are introduced. Currently in preparation, the experiment aims to perform radioactive ion beam implantation into LXe followed by extraction and identification. The experimental approach involves stopping a radioactive beam of ^{139}Cs ions in LXe, extracting the decay product ^{139}Ba after a certain collection time, and then identifying the extracted ions using γ spectroscopy.

An engineering rendering model of the apparatus is shown in Figure 2.3. Also shown is the current state of the setup at TRIUMF's ISAC-II experimental hall. There are three main components to the setup: the Injection Chamber (IC), the Measurement Chamber (MC), and the electrostatic probe. The IC contains a LXe chamber of volume 1.045 cm^3 and 1.9 cm thick copper walls. It is thermally coupled to a liquid nitrogen (LN_2) reservoir with copper heat-transfer straps and suspended in a vacuum chamber for thermal insulation [74]. The copper straps have a high thermal conductivity, allowing for the LN_2-enabled cooling system to over-cool the IC. For this reason, the cooling system also consists of gold resistive heaters, allowing for a better range of temperature control. The heaters are controlled by a Proportional Integral Derivative (PID) controller, which could hold the temperature of the cell at approximately 165 K to maintain Xe in its

liquid state. There are already PT100 Resistive Thermal Device (RTD) probes installed to measure the temperature of the cell.

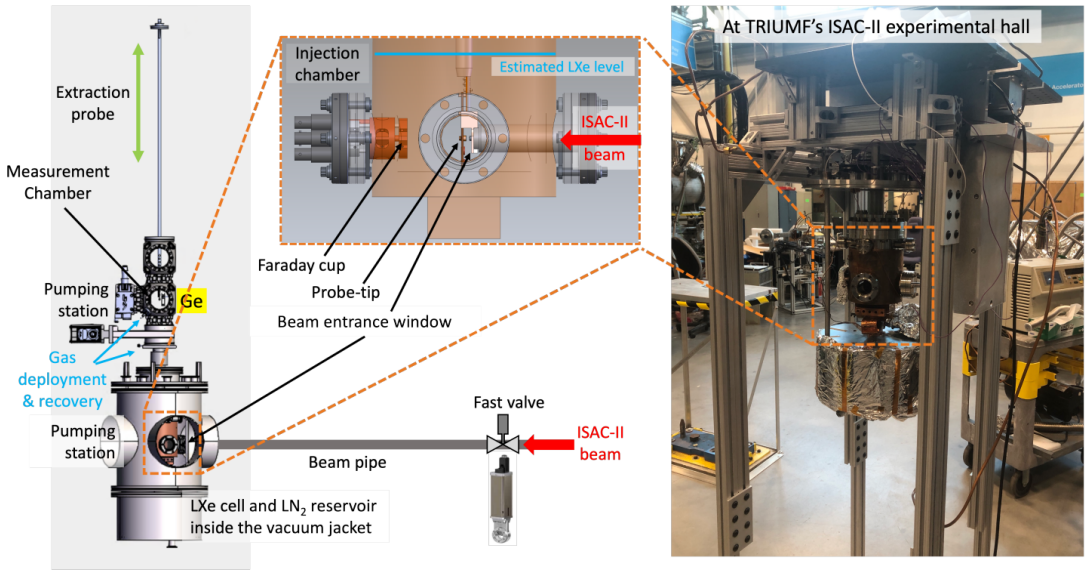

FIGURE 2.3: Left: Ba-tagging apparatus at TRIUMF. A Computer-Aided Design (CAD) model of the Ba-tagging system showing the Injection Chamber, Measurement Chamber, and extraction probe. Right: The current setup at TRIUMF, under reassembly. Adopted from [74].

There are four ConFlat, (CF2.75″) ports surrounding the LXe cell. One of the ports will be fitted with a radioactive-ion beam entrance window to contain the LXe within the cell. The port opposite to the beam entrance window will be fitted with a Faraday-cup detector for tuning the RIB into the cell. The two side-view ports will be reserved for visible verification of the probe position within the cell.

The beam entrance window will be manufactured by Moxtek using commercially available Be of width 7.62 μm. This thickness is best suited for letting through a mass 139 beam, while withstanding a significant pressure gradient between both sides of the window ($\sim 10^{-7}$ Torr and > 1 atm) and the cryogenic conditions of the system. Extensive testing regarding the beam entrance window has been carried out by T. Daniels et.al at the University of North Carolina Wilmington (UNCW). The window will be attached on the tip of a mounted nozzle by either epoxy or metal diffusion bonding, as seen in the inset in Figure 2.3, and in (c) of 2.4. The nozzle will extend into the LXe through the CF flange on the LXe cell.

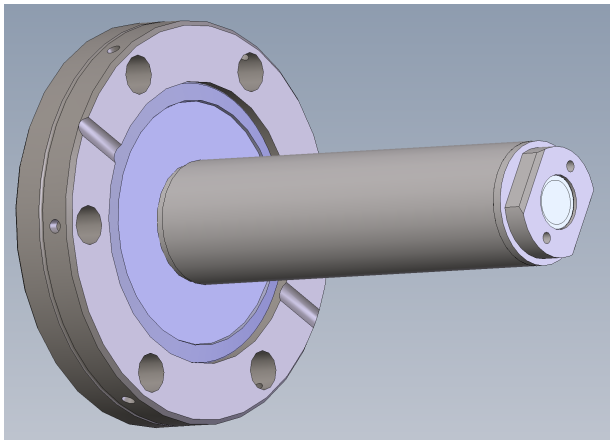

FIGURE 2.4: An engineering rendering of the beam window mount, showing the future position of the Be window at the end of the cylinder.

The MC is located above the IC. This chamber will house a high purity Ge-detector (HPGe), beside which the extraction probe tip will be placed. The motion of the extraction probe is controlled by a linear actuator with a stepper motor. Additionally, the probe tip has the functionality to be biased.

Also shown at the bottom of Figure 2.3 is a beam pipe and a fast-acting valve. The installation of the setup will be at the SEBT-I beamline in ISAC-II, connected by a beam pipe outfitted with a fast-acting valve to preserve the rest of the beamline vacuum in the event of a window failure. The setup requires a beam stand to ensure that it is levelled properly with the SEBT-I beamline. The beam stand is currently under construction, and the pumping system with interlocks was developed by M. Good at TRIUMF. The controls of all of the pumps and gauges responsible for the temperature and pressure readback will be integrated with EPICS.

The LXe cell will be maintained at a pressure of approximately 900 Torr inside the IC. It would require ∼3.1 kg of xenon gas (GXe) to fill the xenon to the blue line shown in the inset of Figure 2.3. A gas handling system (GHS) is under development for deploying and recovering the GXe for recycling and purification as a means of reducing future material costs. A schematic of the GHS is shown in Figure 2.5. The design of the GHS has been approved by the TRIUMF Detector Group, and it is in its final stages before commissioning. The GXe will be deployed from the GHS into the setup from a pre-filled gas bottle (GB1) through a cold getter purifier (GP) to remove any contaminants. The recovery process will return the gas into the other (empty) gas cylinder, through cryopumping. On the next deployment, the GXe will be supplied from the second (now-filled) bottle. Along the system, there are high pressure burst discs and relief valves connected to the nuclear exhaust of the experimental hall. Other features include a pressure regulator, pressure transducers, and an interlock control system for safety.

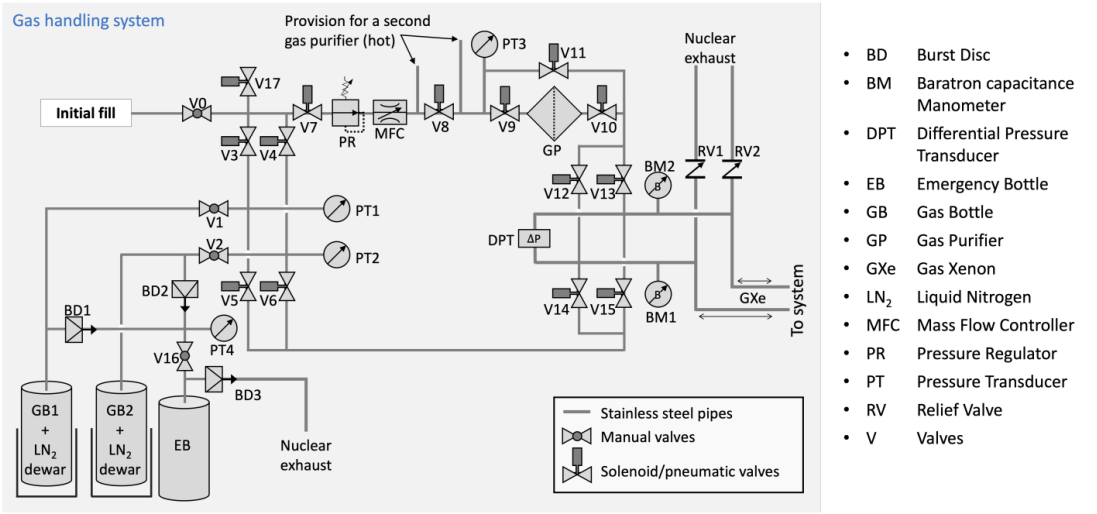

FIGURE 2.5: Gas handling system (GHS) of the Ba-tagging setup. It is a closed system to store, supply and recover GXe with minimal or no loss.

The LN_2 dewar, located at the bottom of the IC, allows for the chamber to reach temperatures as low as 103.15 K; it is also covered with super insulation. Unless hardware updates are made to support a lower temperature, the current setup is capable of liquifying Xe and Kr, given the temperature values in Table 2.1. This gives options for testing and commissioning purposes. The saturation curve of Xe is depicted in Figure 2.6 to contextualize these values, and the same plots for Ar and Kr can be found in Appendix A for comparison. The gas of choice is injected into the setup, and condenses to liquid form at the bottom of the Cu cell.

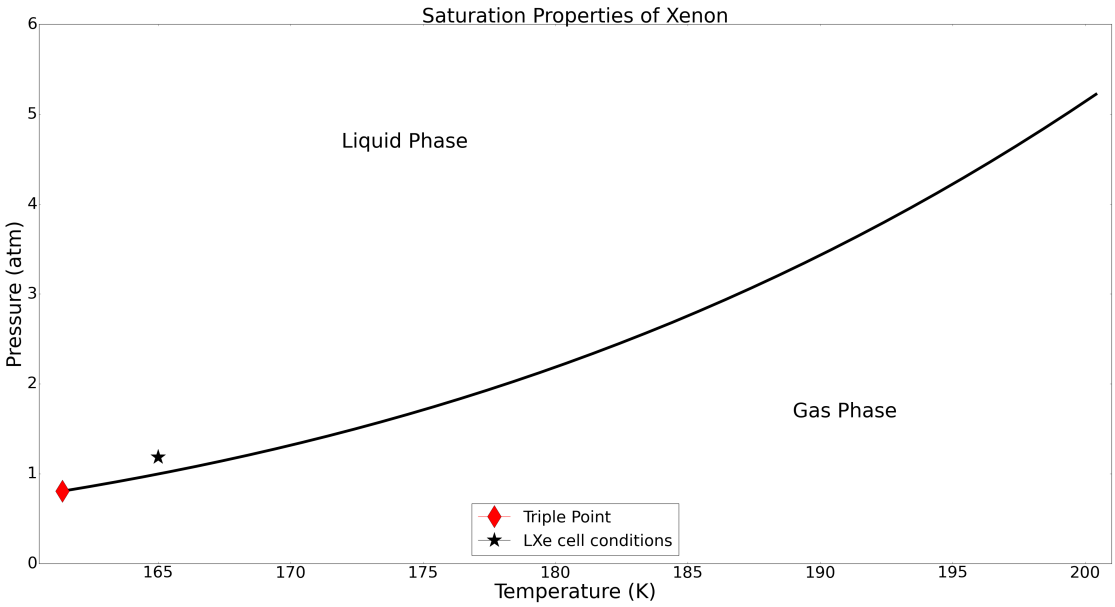

FIGURE 2.6: The saturation curve for Xe. The red diamond denotes the triple point. The green point denotes the conditions for the Xe in the IC. The black star represents the conditions in the LXe vessel. Saturation data from NIST [95].

Fluid	Boiling Point (K)	Melting Point (K)
Xe	165.02 ± 0.05	161.36
Ar	88.15 ± 0.02	83.81
Kr	119.93 ± 0.05	115.79

TABLE 2.1: Boiling and melting points of Xe [96], [97], Ar [98], [99] and Kr [100], [101].

This apparatus was previously used at Stanford University for Ba-tagging developments using an internal, spontaneously-fissioning ^{252}Cf source and a deposition substrate for Resonance Ionization Spectroscopy (RIS) and Time-of-Flight (TOF) spectroscopy [102, 103, 104]. During these studies, liquification of xenon was demonstrated. For the recommissioning of this apparatus, components such as the TOF spectrometry section and a load-lock substrate-mounting section originally included will be removed. The RIS chamber will be repurposed into a Ge chamber.

2.3 Commissioning in Gas Media and Proposed Experimental Plan

As previously mentioned, the nEXO collaboration has been developing different Ba atom and ion identification techniques. Open questions remain primarily towards the extraction of Ba-ions from LXe. Our experiment in preparation at TRIUMF is the first proposed experiment that is planned, as a proof of concept, to demonstrate that it is possible to inject radioactive barium beam into a liquid xenon cell, as in Figure 2.7, and then extract it, along with its decay products, respectively. Thus, demonstrating the missing step in the Ba-tagging scheme. The methods are described in this section. The experimental goals are divided into three phases, leading up to the commissioning of the setup with a LXe medium. The third phase is briefly described in Section 4.

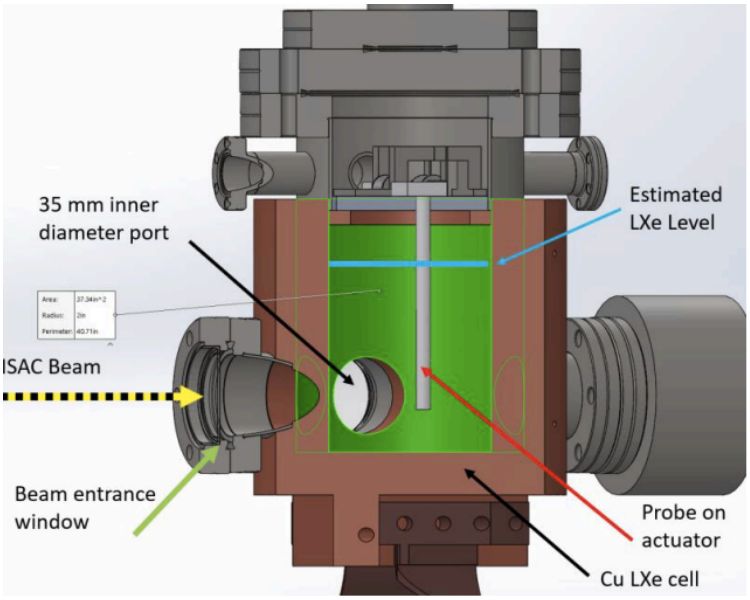

FIGURE 2.7: A cross section view of the LXe cell. The region highlighted in green is the inner wall of the LXe cell, and the fill level is denoted by the horizontal blue line. The probe is also shown; it is controlled by a linear actuator. The beam entrance window is indicated on the left, through which the beam will be injected.

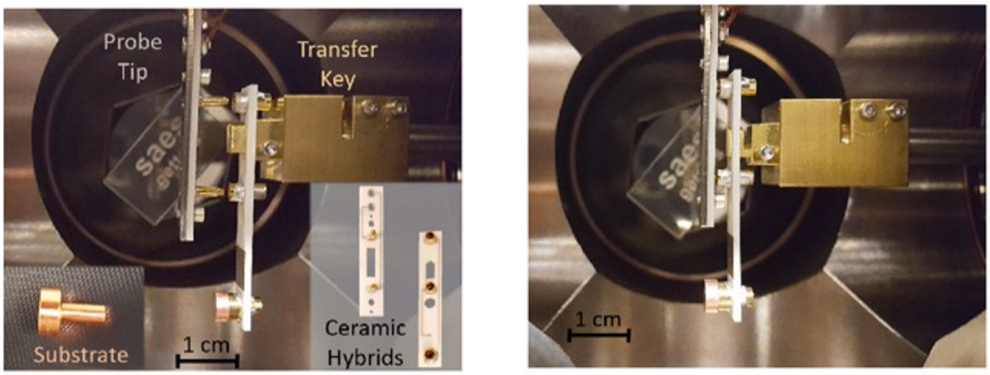

(A) (B)

FIGURE 2.8: A close view of the probe inside the Cu cell, as assembled for its previous experimental purposes [104].

Phase 1: Initial commissioning with gas media

This phase outlines the commissioning of the entire apparatus, including the vacuum system, safety interlocks, and GHS. Also, the electrostatic collection and extraction of ions from gas will be commissioned. Simulations in this thesis explore the extraction efficiency in different gas media, in addition to LXe, as well as the optimal probe biases and configurations required to extract the implanted ions from a specific position in the gas.

The plan is to connect the Cu cell, of about 1 L in volume, to the SEBT-I beamline shown in Figure 2.2 in Appendix B. The cell will be commissioned with argon and xenon gases, up to pressures of ∼900 Torr. Ar gas is more economical for the initial commissioning of the apparatus, prior to using Xe gas. Additionally, these campaigns using gas-media will be used to optimize the GHS, beam intensities and implantation times, and detection procedures including the HPGe-detector position and the necessary data-acquisition times, before the experiment will be repeated using LXe [74].

The extraction probe will be placed in the gas volume using the linear actuator. The probe tip, as in Figure 2.8, must then be aligned with the beam entrance window, labelled in Figure 2.7. The radioactive beam ions will then be implanted into the gas-filled cell through the Be beam-entrance window on a mount, in which they will travel a certain distance before coming to rest, or before all its energy is lost. This distance is referred to as the stopping range of an ion, and it can be determined by the Bethe-Bloch formula for the stopping power S, defined as the mean energy E loss suffered by a charged particle per unit path length x [105]:

$$S = -\frac{dE}{dx} = \left(\frac{e^2}{4\pi\epsilon_0}\right)^2 \frac{4\pi n Z^2}{m_e c^2 \beta^2} \left[ln\left(\frac{2m_e c^2 \beta^2}{I}\right) - ln(1-\beta^2) - \beta^2 \right], \tag{2.1}$$

for a particle with speed v, charge Z, traveling a distance into a target of electron number density n and mean excitation energy I, in SI units. The permittivity of free space is denoted by ϵ_0 and $\beta = \frac{v}{c}$, where c is the speed of light. The stopping power depends on the charge and velocity of the projectile ion, as well as the target material [106]. For an ion beam penetrating through matter, energy loss would result from collisions with electrons (electronic stopping) and target nuclei (nuclear stopping) [107]. Depending on the velocity of the ions, the energy loss is governed by one of these two regimes. Nuclear stopping dominates when the charged particle loses energy through an effective interaction with the host ions, and the electrons respond instantaneously without undergoing excitations. The electronic stopping regime dominates the ions' energy loss at high velocities, where the ion loses energy by partially screened Coulomb interactions with the electrons, and the host ions do not have time to react as a result of large inertia.

The stopping range for ^{139}Cs beam ions in LXe as calculated by TRIM are shown in Figure 2.9. In gas media, however, the stopping range for mass 139 ions is much farther than in liquids on the order of tens of millimetres.

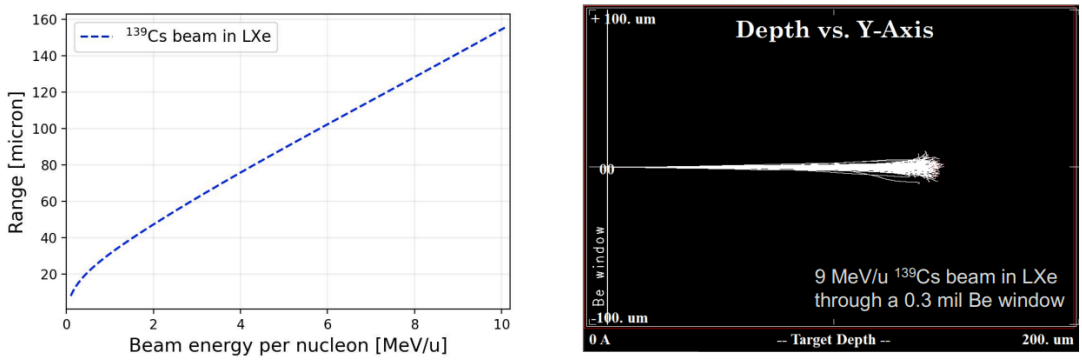

(A) (B)

FIGURE 2.9: (A) The stopping ranges for ^{139}Cs in LXe as a function of beam energy per nucleon, simulated by TRIM [74]. (B) A 9 MeV/u ^{139}Cs beam entering a LXe volume through a 7.62 μm thick Be window. The stopping range is approximately 150 μm.

The beam energy must be adjusted to ensure that the beam ions are not stopped too close to the probe, or stopped as a result of colliding with the probe tip, as this would not demonstrate electrostatic attraction of the ions. This portion of the experiment will be performed at room temperature to ensure that the Be-window is unharmed prior to continuation, as it will experience a significant pressure gradient (about 900 Torr) between its two sides.

Once the ions are implanted into the gas, a DC bias will be applied to the probe tip copper substrate to induce an electric field in the cell, guiding the beam ions towards it. A (negative) voltage of a few hundred V should be sufficient, but hardware allows for a maximum bias of approximately -2 kV. After a certain amount of collection time,

the probe will be removed from the gas volume and placed directly in front of a Ge detector. The Ge detector will be used to detect any radioactivity from the beam ions accumulated onto the probe tip.

After the isotope collected on the probe tip decays away completely, the probe may be reused for another experimental run with different conditions. In future runs, it may also be possible to use a custom-machined spacer to push the beam-entrance window mount back, instead of varying the beam energy.

Phase 2: Commissioning with LXe

In the next phase, we will change the medium inside the Cu cell. The cell will be filled with LXe, maintained at pressures of 900 Torr, and connected to the SEBT-I beamline in ISAC-II, as seen in Figure 2.2. This step will also demonstrate our ability to liquify GXe inside the Cu cell.

Similar to Phase 1, the extraction probe will be moved down into the LXe, with its tip in line with the beam-entrance window. The radioactive beam ions will be implanted through the Be-window. Since they are in LXe, the distance they will travel is on the order of microns, as seen in Figure 2.12. A bias will be applied to the probe tip, and the probe will be moved out of the LXe after collecting sufficient ions. Then, γ-spectroscopy will be performed just as in Phase 1. The ultimate goal of this step is to commission the electrostatic collection and ion extraction from a specific location within the LXe volume.

Currently, the probe is able to move only in the z-direction. Controls will be implemented to enable xy movement of the probe, to test ion collection from various positions within the LXe chamber. Due to the inside diameter of the conflat parts, the xy motion is limited, and it will be possible to scan over a small portion of the LXe chamber. Compared to the ion implantation depth, however, the range of the probe's xy motion is sufficient.

As a secondary project using this apparatus, it will also be possible to perform ion mobility measurements for the implanted beam ions, made possible through the application of electric fields [108]. Generally, this would be performed using a square wave collection voltage; the ions can be driven back and forth to simulate a longer collection path. It would be possible to compare experimentally determined ion mobility and ion drift time values to benchmark COMSOL simulations.

In addition, it may be possible to determine the charge state of the β-decay daughters. The charge state booster (CSB) would be used to produce the beam in q = 22^+. Using the EBIS, this portion of the beam production will differ, by charge breeding to higher charge states in the EBIS directly. To remove contaminants, the beam will be stripped to 31^+ or 32^+ after the drift tube linac (DTL). At these charge state values, the contaminants will be mostly isobars coming from the target.

The design of the setup allows for many systematic studies, some of which can be performed by implanting different isotopes into the Cu cell medium. Since the different isotopes would each have their own specific half-life, studies of neutralization rates of the implanted beam ions drifting through the medium would be possible.

The identification of the beam ions will be done by γ-spectroscopy, searching for the 166 keV γ-ray released in the decay of ^{139}Ba to its daughter ^{139}La. Extensive GEANT4 simulations were performed by L. Backes and I. Casandjian to determine the required number of ions to observe a signal at the anticipated energy value. As well, the simulations determined the amount of time to keep the probe in the Ge-chamber to collect sufficient decay statistics above the background. The simulations were performed assuming realistic conditions for the Ge detector geometry, efficiency, and placement. In Figure 2.11 (B), the 166 keV peak is clearly distinct after 30 minutes of observation time.

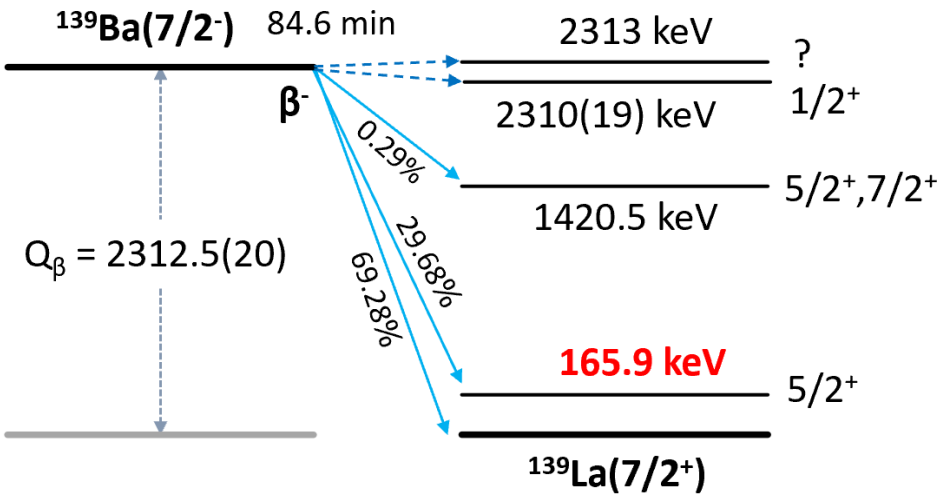

FIGURE 2.10: Schematic showing the energy level of ^{139}Ba and its stable decay product ^{139}La. The 165.9 keV state, highlighted in red, is the state of experimental interest that will be later detected through γ spectroscopy. The half-life of the ^{139}Ba-decay is 84.6 minutes. Energy values from [109].

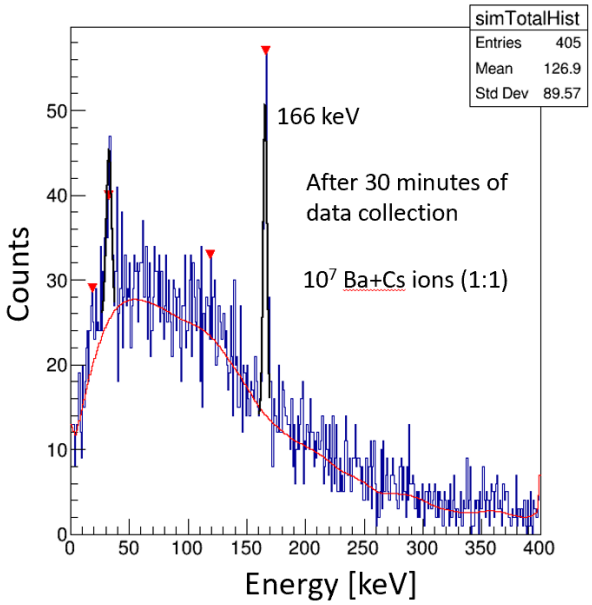

FIGURE 2.11: The γ-ray spectrum of ^{139}Ba and ^{139}Cs, as simulated using GEANT4 by L. Backes and I. Casandjian, for 30 minutes of data collection. The largest visible peak corresponds to the 166 keV γ-ray, denoted in red in (A).

Isotope	$T_{1/2}$	Yield (pps)
^{139}Cs	9.27 m 5	1-2 $\cdot 10^8$
^{139}Ba	82.93 m 9	$5 \cdot 10^7$

TABLE 2.2: Radioactive isotopes and their respective half lives [110] available at TRIUMF. The yields are as measured at the ISAC yield station. By the time the RIB reaches the Ba-tagging apparatus, there may be a decrease in this yield by a certain factor.

Ideally, the composition of the radioactive beam should be entirely ^{139}Cs; the decays to ^{139}Ba would occur in the LXe, mimicking the $0\nu\beta\beta$ decay of ^{136}Xe to ^{136}Ba in the nEXO detector. The expected beam energies for Cs isotopes in ISAC-II are up to 9 MeV/u. The maximum beam energy may reach 10 MeV/u. The stopping ranges of ^{139}Cs is found for various fluid mediums in the Cu cell, as calculated in Figure 2.12. The minimum beam energy required for implantation studies with LXe is 2 MeV/u; at this energy, the ions will travel through the beam window and come to a stop 25-50 mm into gas media and about 50 μm into LXe based on SRIM calculations [111]. The ions' positions will be far enough in the medium of choice for the electric field to guide them away from the window and towards the probe. With higher beam energies from ISAC-II, the stopping ranges will increase, as seen in Figure 2.4 (A). Varying the beam energies will provide one way to perform systematic studies on the ion extraction efficiency.

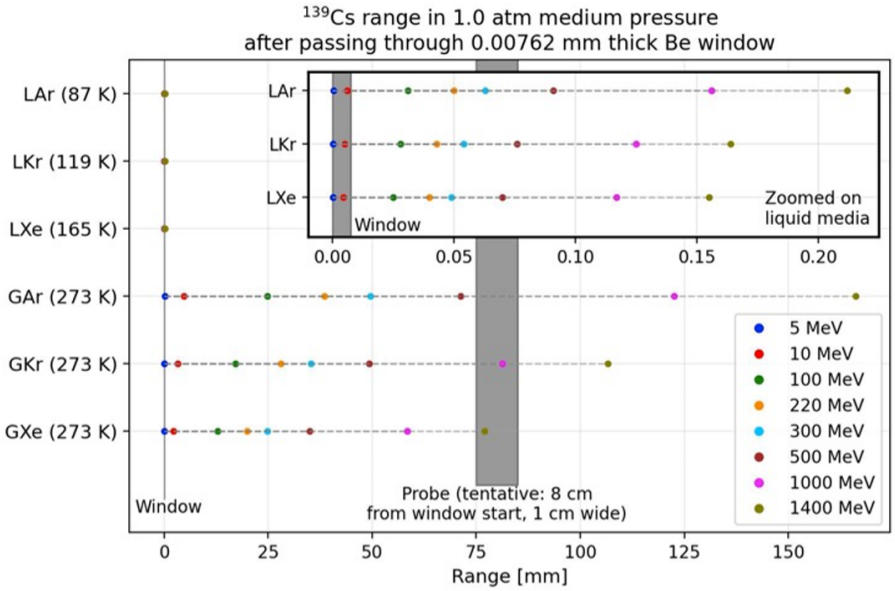

FIGURE 2.12: Stopping ranges of ^{139}Cs in various gas and liquid mediums at 1 atm. Only the latter beam energies are relevant as actual experimental parameters: beam energies greater than 2 MeV/u, corresponding to particle energies greater than approximately 280 MeV. Figure taken from D. Ray, private communication.

To conclude, the apparatus arrived at TRIUMF in late Fall 2022. Work towards Phase 1 is underway. The support structure, vacuum system and safety interlocks are all completed. The model for the window mount for Phase 2 is finalized and will be machined at McGill University before being sent to Moxtek for installation. The window mount will then be tested at UNCW to verify that it meets the pressure and cryogenic temperature requirements. The window mount is not required for Phase 1 of the experiment, since gas media will be used at room temperature. Thus, the window as installed by Moxtek is ready to use for Phase 1.

Sections 1 and 2 serve as the basis for the next section focusing on simulations of the electroprobe in liquid xenon and other mediums, as well as general studies of Ba-ion motion in LXe.

Chapter 3

Electrostatic Probe Simulations

The majority of this Master's thesis project is dedicated to simulating the outlined experimental apparatus in action prior to its arrival at TRIUMF. The purpose of the simulation is to check if ions can be drifted to specific locations within the liquid xenon, such as the electrostatic probe, which would allow for ion extraction studies. The simulations also serve as a method to understand ion loss mechanisms to determine extraction efficiency. This chapter serves as a guide for the simulation work performed of the experimental setup outlined in Chapter 2. The verification methods used to ensure that the simulation's structure and parameters are correct and that the particles' behaviour is as realistic as possible are described. The model is also used to perform various systematic studies of ion diameter, ion initial distance from probe and probe bias, to name a few.

3.1 Software Considerations

The first step in performing the simulations is selecting the most suitable software for these studies. There were several software options to carry out simulations of the experimental setup, namely COMSOL, SIMION, and OmniTrak. The capabilities were investigated of each of these listed software packages commonly used for simulating ion motion. SIMION is typically used to "calculate electric fields and the trajectories of charged particles in those fields when given a configuration of electrodes with voltages and particle initial conditions, including optional RF (quasistatic), magnetic field, and collisional effects" [112]. Ultimately, SIMION was not pursued because it is more suitable for gas environments (lower pressure mediums), rather than liquids. Convergence issues may arise while attempting to solve ion-gas collisions for xenon under very high pressure. SIMION is not a Computational Fluid Dynamics (CFD) solver.

OmniTrak is often used in the analysis of 3D charged-particle devices; it uses finite element methods to calculate ion trajectories to a high degree of accuracy. Basic simulation geometries were possible to run in OmniTrak, but difficulties arose when adding in critical parameters. For example, there is no option to consider drag force for fluids. OmniTrak characterizes all of the liquid xenon properties within the ion mobility μ. While this simplistic model provides a reasonable estimate of the barium trajectories within liquid xenon, COMSOL is required for more involved studies.

COMSOL Multiphysics can solve a wide variety of physics, ranging from mechanical, chemical, acoustic, and electrical applications. This software uses the finite element method (FEM) to compute approximations to the partial differential equations (PDEs) of interest in a specific physical geometry. Since these PDEs cannot typically be solved analytically, approximations to these equations are necessary. "These discretization methods approximate the PDEs with numerical model equations, which can be solved using numerical methods. The solution to the numerical model equations are, in turn, an approximation of the real solution to the PDEs" [113]. FEM is used to calculate these approximations.

COMSOL is the ideal software for the purposes of this project because it can combine the main physics phenomena present in the experimental setup: the electrostatics of the probe's field configuration, the fluid dynamics in liquid xenon, and the barium ion ray tracing. These functionalities can simulate the barium ions as they move through liquid xenon and onto the electrostatic probe. Other advantages to the program include the possibility to define your own parameters where appropriate, such as forces or fluid properties. There is a broad scope of possibilities for systematic studies, since the user has the freedom to control the majority of the parameters. Also, COMSOL is able to generate refined 3D visualizations and plots.

The organizational structure of COMSOL is as follows: the user is able to add on *interfaces*, which are the physics modules. These modules are also able to be coupled together in *Multiphysics*. It is possible to then add pre-existing, built-in *nodes* under every interface, each with its own specific function such as accounting for boundary conditions. The *domain* is a volume region within a geometry, and the user must define what physics to solve for each one, as well as physical properties and conditions of the material.

There are also disadvantages to using COMSOL for these studies, most of which are related to the difficulty of a beginner to learn the program and troubleshooting. Some of the common simulation issues, as well as potential fixes, are shared in this chapter. As with any programming project, it is best to begin with a simple model and gradually add in complexities.

3.2 Benchmark Model

A proof of concept exercise to investigate the capabilities of COMSOL within this context is described below. It may also act as a future tester simulation environment where parameters can be adjusted and solved rapidly, without involving other complexities of the simulation. In this preliminary model, there is a row of positively charged particles moving in the direction of an applied electric field. This simulation and the remaining simulations outlined in Chapter 3 are performed in three dimensions because it is the most comprehensive approach, especially in terms of simulating particle ray tracing.

The only material included in the simple geometry is liquid xenon. It is not necessary to include the copper vessel, or the stainless steel probe tip, just yet. The plain cylindrical

vessel is 10 cm tall and has a radius of 10 cm. The meshing is set to extremely fine, and it is possible to further resize the meshing elements to fit custom requirements. The mesh of this geometry is shown in Appendix C.

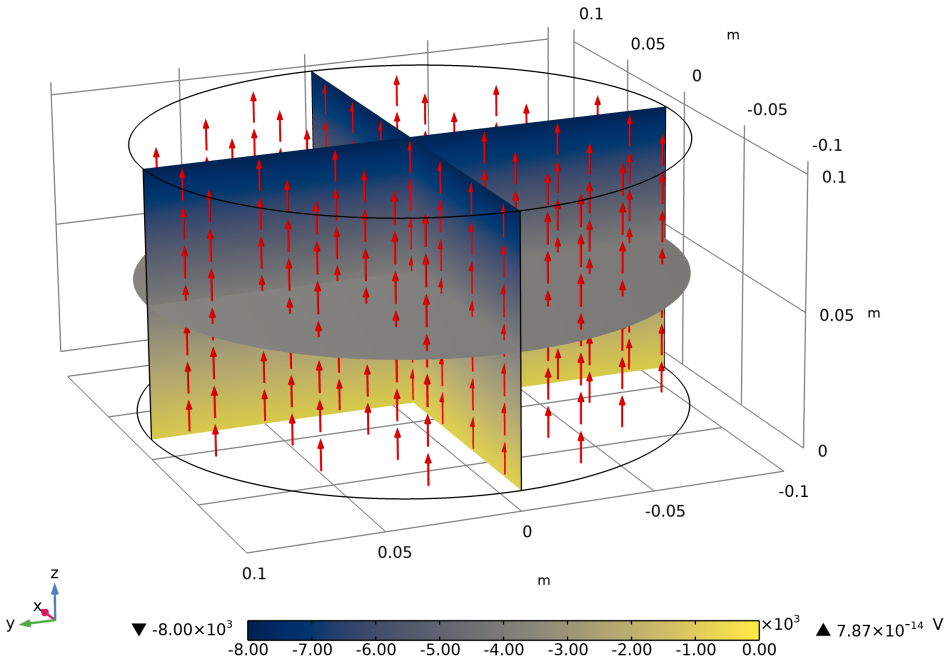

FIGURE 3.1: Electric potential (V) in simplistic model. Red arrows represent the direction of the electric field.

Using the *Electrostatics* interface, the surfaces of the liquid xenon cylinder are biased such that a uniform electric field is produced within it. The top face is biased to -8 kV ($V_{cathode}$) for ease of comparison to previous simulations, the bottom face is grounded (V_{anode}), and the curved side (V_{side}) is biased according to Equation 3.1.

$$V_{side} = V_{anode} + V_{cathode}\left(\frac{z}{Total\ Height}\right) \tag{3.1}$$

The electric potential produced throughout the geometry is shown in Figure 3.1. The direction of the field is upwards, as indicated by the red arrows. The magnitude of the electric field is represented in Figure 3.2; the field is fairly uniform throughout the liquid xenon, and the electric force will be the only driving factor moving the particles. This model does not simulate fluid flow–only the dielectric properties of the liquid xenon are required. Since fluid flow is not considered, the *Charged Particle Tracing* interface is used to perform particle tracing in Figure 3.3. The drag force is ignored, as well as gravity, and any particle-particle interactions for simplicity.

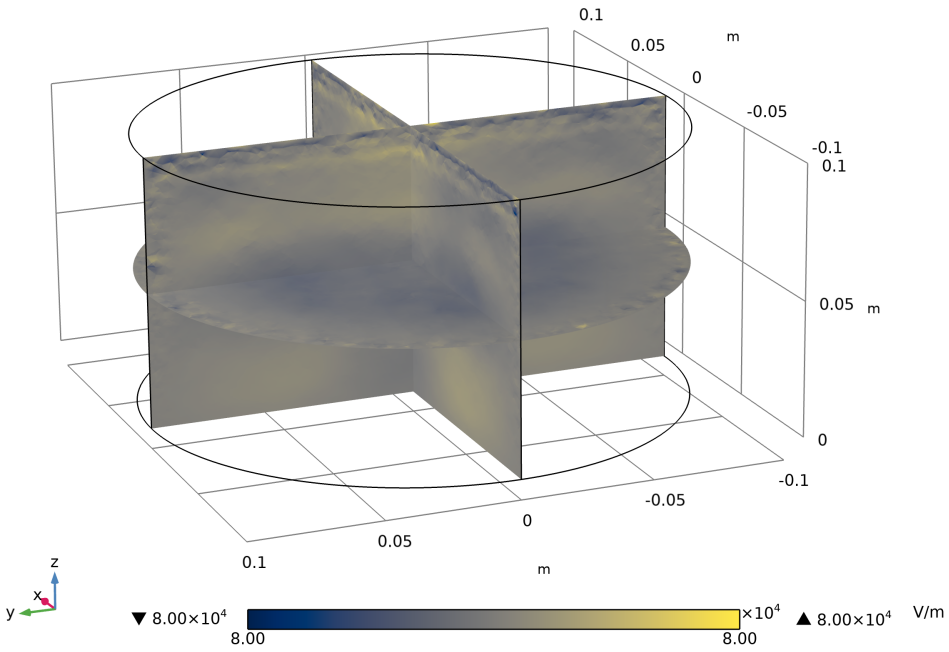

FIGURE 3.2: Electric field (V/m).

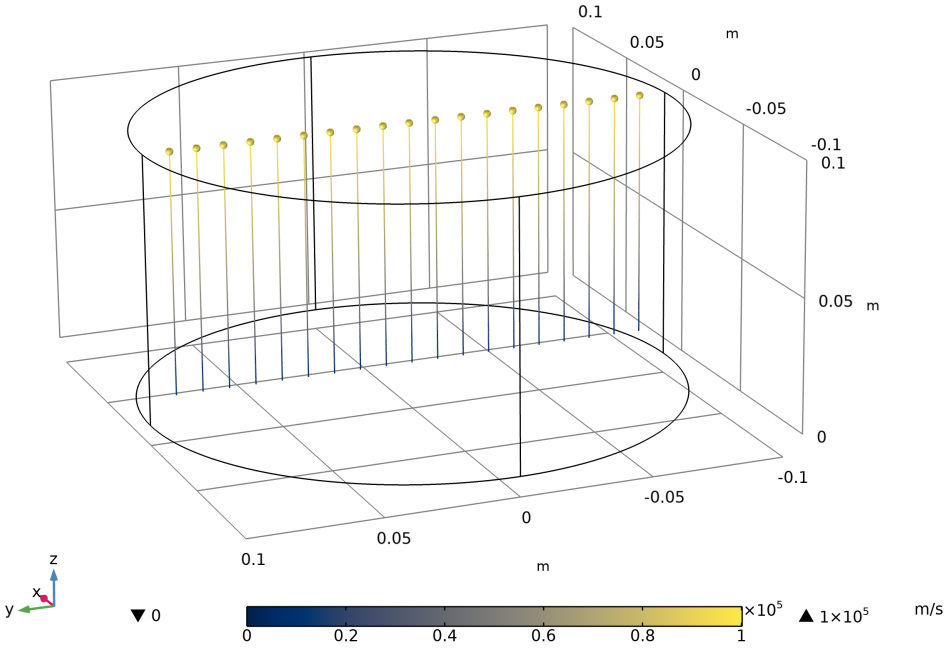

FIGURE 3.3: Singly charged ^{139}Ba trajectories in liquid xenon. Ions are shown at their final position at the top of the cylindrical vessel.

A row of singly charged ^{139}Ba ions is placed near the bottom of the cylinder. After running the simulation, the particles move upwards in the direction of the electric field as expected. The ion trajectories can be traced using smaller time steps (≈ 1 μs) to see their position evolve as they approach the top of the cylinder. In a simplified model, the ions' velocity $\vec{v}$ is represented by Equation 1.24 introduced in Chapter 1, where K is the ion mobility, and $\vec{E}$ is the electric field to which the ions are exposed.

The ion mobility is an intrinsic value that is unique to an ionic species. This value is important throughout the simulations to check particles' behaviour in the model and compare to experimentally measured values of μ.

This model demonstrates the suitability of COMSOL for performing more involved simulations of the experimental setup outlined in Chapter 2, and provides the first conditions for the main simulation environments discussed in the rest of this Chapter.

3.3 Simulation Environment

3.3.1 Simulation Geometries

In this section, two simulation models named 'Model A' and 'Model B' are introduced, including the physics solved in both of the simulation models that were built for simulating the trajectories of singly charged barium ions as they move towards an electrostatic probe. Simplifications to the geometries are also summarized. The geometries are modelled after the barium tagging experimental setup outlined in the previous chapter.

Both Model A and Model B include a fluid volume, a copper boundary surrounding the fluid, and a probe extending downwards in the centre. The probe is initially stationary inside the fluid prior to the addition of the ions. The two geometries differ in the size and placement of the inlet and outlet features. They also have different probe shapes and biased surfaces on their respective probes.

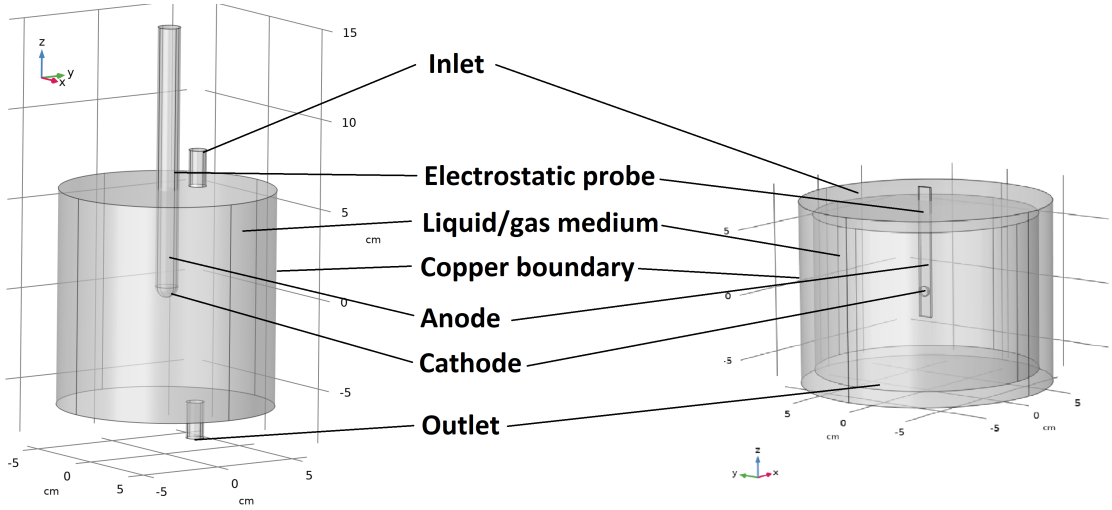

FIGURE 3.4: Geometries of the COMSOL simulations. The slight geometric differences between Model A (left) and Model B (right) are shown.

The inlet and outlet attached to the copper vessel in Model A are included for convergence purposes in the fluid dynamics model; these components are not physically present in the experimental apparatus. In Model B, the inlet and outlet features are defined as the entire top and bottom faces of the vessel. These differences in the models allow for faster convergence times depending on the type of study being run, and do not ultimately affect the physics being solved.

The coordinate units in the geometry can be configured appropriately (centimetres). Care was taken to note the unit used, especially when releasing a set of custom particle positions; it is important for scaling purposes of external files.

In later phases of the experiment, the probe may be moved into the medium during radioactive beam application. Simulating this later phase would require modifications to the current simulation model. Preliminary studies on a general moving electroprobe were done in a former student's thesis at Carleton University. However, there has been no simulation work done to explore barium ion deposition into liquid xenon, and subsequent extraction by a stationary electroprobe. As well, finding the optimal experimental settings for the barium tagging apparatus.

3.3.2 Solving Electrostatics

The simulations are separated into three main types of studies: electrostatics, fluid dynamics, and particle tracing. The former two studies are solved together using a stationary solver, and the particle tracing requires a time-dependent solver. We begin with the electrostatics solution.

The *Electrostatics* interface computes the electric field and potential distributions in

dielectric materials where the electric charge distribution is explicitly defined. This feature models the induced electric field in the medium of interest, namely liquid xenon, in the copper vessel generated by the electroprobe. It is possible to bias different components and surfaces within the geometry. A time-independent electric field is computed, by solving the necessary equations in a stationary state. Within the context of the simulation, it can be assumed that the liquid or gas medium in the copper vessel is an idealized dielectric material; it has bound charges, rather than free charges. The bound charges can be displaced by an outside electric field, producing induced electric dipoles– pairs of positive and negative charges that align with the external electric field. This process results in an electric field, $\vec{E}$, inside the dielectric material, different than that of free space. This phenomenon is described by the polarization vector field, $\vec{P}$, and the polarization charge density ρ_p. These quantities are related by [114]:

$$\rho_p = -\nabla \cdot \vec{P} \tag{3.2}$$

The electric field within a material is modified according to the relation

$$\nabla \cdot \vec{E} = \frac{\rho + \rho_p}{\epsilon_0}, \tag{3.3}$$

where ρ is the space charge density, and ϵ_0 is the permittivity of free space. Similarly, Equation 3.3 can be represented as

$$\nabla \cdot (\epsilon_0 \vec{E} + \vec{P}) = \rho, \tag{3.4}$$

where the electric field displacement $\vec{D}$ can be defined as

$$\vec{D} = \epsilon_0 \vec{E} + \vec{P} \tag{3.5}$$

The constitutive relationship for linear dielectric materials is configured in the interface as Equation 3.5, setting the relation for the electric displacement field, $\vec{D}$. By applying this definition, a modified version of Gauss' law becomes

$$\nabla \cdot \vec{D} = \rho_v \tag{3.6}$$

The *Electrostatics* interface fully describes electrostatics phenomena by finding solutions to Equation 3.6, and Equation 3.7, Faraday's law of electrostatics. Faraday's law holds true because of the condition that the electric field is irrotational.

$$E = -\nabla V \tag{3.7}$$

It is assumed that the fluid media used are linear dielectric materials in the simulated temperature ranges. The *Charge Conservation* node adds the equation for the electric potential and describes the macroscopic properties of the medium, as well as the constitutive relation for the electric displacement field– relating $\vec{D}$ and $\vec{E}$ together. One such associated material property is the relative permittivity; for liquid xenon, the value

for ϵ_r is approximately 1.87 [115]. For materials for which the relative permittivity is unknown, the value is set to 1.

After ensuring the correct equations and dielectric model are set, certain surfaces in the geometry are biased. An example of the electric potential for Model A is shown in Figure 3.5. Here, the probe tip is biased to -4 kV. The rest of the geometry is grounded.

The magnitude (and polarity) of the potential can be varied in the simulation, which consequently allows for control over the electric field density in the fluid medium. The electric field produced by biasing the probe tip immersed in liquid xenon is shown in Figure 3.6. Typical bias values (in combination with particle tracing) ranged from -100 V to -2 kV. Generally, any probe shape with biased surfaces on the probe tip will result in a similar electric field. This is explored later in this chapter.

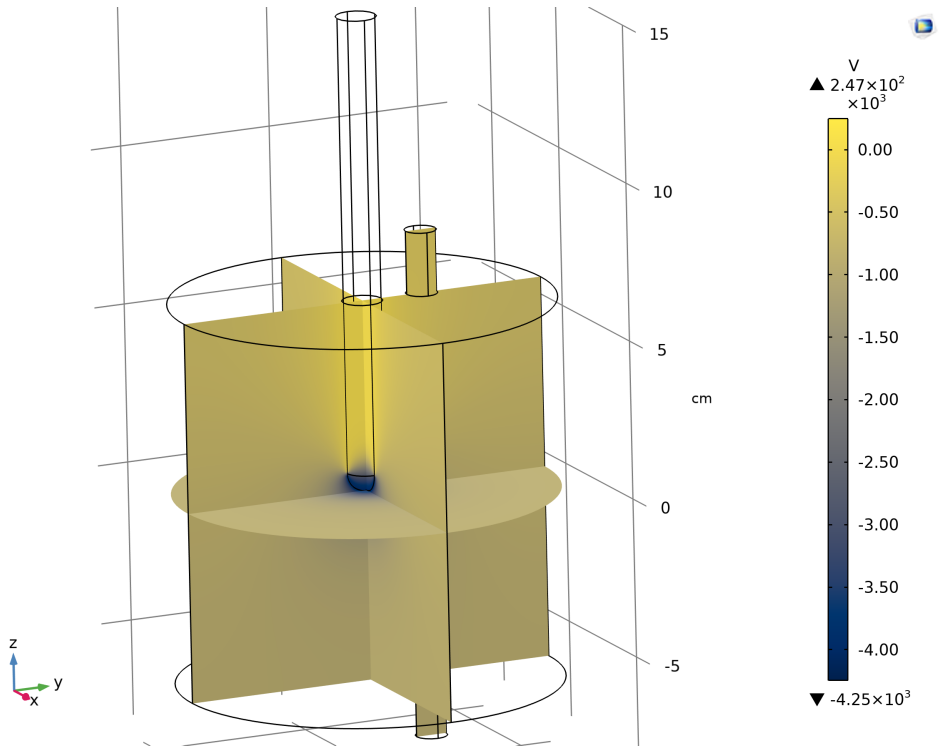

FIGURE 3.5: The electric potential (V) configuration around a biased probe tip. A voltage of -4 kV is applied to the surfaces on the rounded probe tip in Model A. The rest of the probe is grounded.

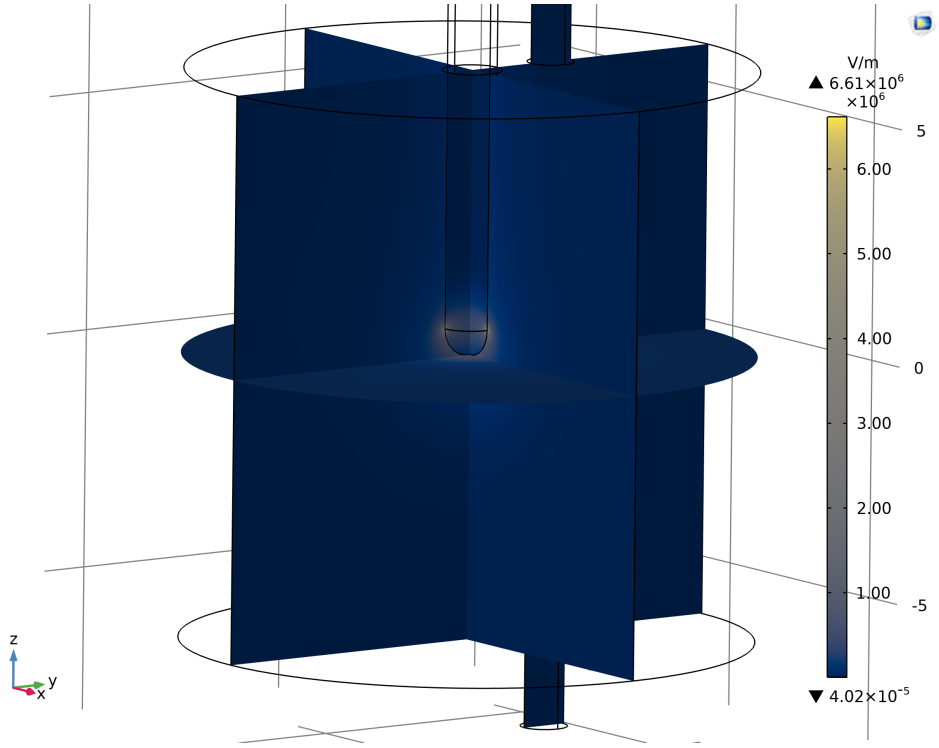

FIGURE 3.6: The electric field (V/m) around the probe tip and surrounding regions in liquid xenon, given the biased surfaces in Figure 3.5.

After configuring the electric field, it is also important to ensure that particles injected to the simulation environment are actually subjected to an electric force. This verification test was performed whenever it was suspected that the charged particles do not move as expected in the presence of an electric field. By checking the electric force felt by the particles, it is possible to determine if the strength is simply too low for particles to be affected by it, or if other troubleshooting methods should be pursued. In cases where the force is not felt by the particles, extra care was taken to check the domains included in the interface, while removing any unnecessary ones and verifying the boundary conditions. The *Electrostatics* portion of the simulation should be relatively quick to run on its own, given all of the correct boundary conditions and material properties.

3.3.3 Fluid Dynamics Solution

This section describes the fluid flow model solved in the simulations by the *Fluid Flow* interface, showing only liquid xenon solved in both Model A and Model B. It is the most computationally heavy portion of the COMSOL simulations.

There are many mathematical models that can be used to represent the movement of a fluid. The most exhaustive description is derived from PDEs. A fluid flow field is defined

by a balance in mass, momentum, and total energy described by the continuity equation, the Navier-Stokes equation, and the total energy equation in terms of the temperature:

$$\frac{\partial \rho}{\partial t} + \nabla \cdot (\rho \vec{u}) = 0 \tag{3.8}$$

$$\frac{\partial \rho \vec{u}}{\partial t} + \nabla \cdot (\rho \vec{u} \vec{u}) = -\nabla p + \nabla \cdot \tau + \vec{F} \tag{3.9}$$

$$\frac{\partial}{\partial t}\left[\rho\left(e + \frac{1}{2}u^2\right)\right] + \nabla\left[\rho\vec{u}\left(e + \frac{1}{2}u^2\right)\right] = \nabla \cdot (l \nabla T) + \nabla \cdot (\vec{u} + \tau \cdot \vec{u}) + \vec{u} \cdot \vec{F} + Q \tag{3.10}$$

The solution to these equations provides the velocity field $\vec{u}$, the pressure p, and the temperature T of the modelled fluid. These equations can describe a wide range of fluid models, from creeping flow to supersonic flow. Many times, it is not necessary to fully solve the equations above for a low-flow fluid model, and suitable approximations can be made to reduce the computation time while achieving accurate results.

There are several fluid properties to set in order to solve the fluid model; an example of common simulated values for these properties for liquid xenon are outlined in Table 3.1; these values are general estimates.

Medium	Temperature (K)	Pressure (atm)	Density kg/m^3	Viscosity μPas
LXe	165.5	1.33	3000	510.37

TABLE 3.1: Common liquid xenon fluid parameters for COMSOL simulation purposes.

The density, viscosity, and temperature values are straightforward to define. Within COMSOL, the viscous effects are encapsulated by the viscous stress tensor, denoted by τ in Equation 3.9. For a Newtonian fluid, such as liquid xenon, τ is represented by Equation 3.11:

$$\tau = \mu\left(\nabla\vec{u} + \nabla\vec{u}^T\right) - \frac{2}{3}\mu\left(\nabla \cdot \vec{u}\right)\vec{I} \tag{3.11}$$

This effect is taken into account when the constitutive relation is set for a Newtonian fluid. Also, the compressibility of the fluid must be specified by the program. A fluid with constant or very small variations of viscosity and density is considered an incompressible fluid. The condition $\frac{\Delta\rho}{\rho} \ll 1$ must be met. If viscous heating can be neglected, and the fluid is Newtonian as in our case with liquid xenon, Equations 3.8, 3.9, and 3.10 can be simplified to:

$$\nabla \cdot \vec{u} = 0 \tag{3.12}$$

$$\rho \frac{\partial \vec{u}}{\partial t} + \rho \vec{u} \cdot \nabla (\vec{u}) = -\nabla p + \nabla \cdot \left(\mu \left(\nabla \vec{u} + \nabla \vec{u}^T \right) \right) + \vec{F} \tag{3.13}$$

$$\rho C_p \frac{\partial T}{\partial t} + \rho C_p \vec{u} \cdot \nabla T = \nabla \cdot (k \nabla T) + Q \tag{3.14}$$

The term $-\frac{2}{3}\mu (\nabla \cdot \vec{u}) \vec{I}$ in Equation 3.11 would disappear from the viscous force term in the case of an incompressible fluid. It is removed because the continuity relation in Equation 3.12 must hold true. The solution to these equations gives the velocity and pressure fields for fluids with constant or very small variation of viscosity and density.

Different flow models can be described by a corresponding Reynolds number. The set of equations used for modelling fluid flow are chosen based on the range of values that the Reynolds number falls in, defined as R_e in Equation 3.15

$$R_e = \frac{\rho U L}{\mu} \tag{3.15}$$

where μ and ρ and are the fluid's dynamic viscosity and density, U is a representative velocity scale, and L is a representative length scale. If the density and viscosity are constant, and if there are no body forces, Equation 3.13 can be nondimensionalized as

$$\frac{\partial \vec{u'}}{\partial t} + \vec{u'} \cdot \nabla \left(\vec{u'} \right) = -\nabla p' \frac{1}{Re} \Delta \vec{u} \tag{3.16}$$

where p' is $(p - p_0)/(\rho U^2)$, and p_0 is a representative pressure level. From Equation 3.16, it is evident that the Reynolds number governs the importance of the viscous stresses. In fluids with a low Reynolds number, the flow is fully determined by viscous effects, whereas at high Reynolds numbers the flow is virtually non-viscous.

The limit where R_e tends towards 0 is also known as Stokes flow, which is the region of interest for these simulations. As R_e increases, the fluid flow models gradually become more turbulent. It is not required to include turbulence in this fluid flow model with liquid xenon (or argon), but it becomes relevant for gaseous media. The most suitable fluid flow model for an idealized scenario involving liquid xenon is *Creeping Flow*, since there is no turbulence, but there is still some particle motion. The Creeping Flow interface is only defined for the domain that includes the liquid xenon, where it models the Navier-Stokes equations without the contribution of the inertial term. The inertial terms are found on the left side Equation 3.13, and neglecting these terms (and the $-\frac{2}{3}\mu (\nabla \cdot \vec{u}) \vec{I}$ term) leaves Equation 3.17: only the pressure forces (first term), part of the viscous force (second term), and any external forces applied to the fluid (third term):

$$0 = -\nabla p + \nabla \cdot \left(\mu(\nabla \vec{u} + (\nabla \vec{u})^T)\right) + \vec{F} \tag{3.17}$$

This model is suitable for flow at small Reynolds numbers, such as in very small channels or in microfluidic applications. The fluid's velocity, pressure, density, and dynamic viscosity are represented by u, p, ρ, and μ respectively.

Setting the pressure of the liquid xenon using Creeping Flow, however, requires some trial and error because the fluid model is more restrictive, and prone to convergence errors. When the chamber is filled with liquid xenon in the simulation, the xenon can be thought of as nearly at rest. Realistically, however, there will not be xenon flowing in and out of the chamber during radioactive beam application. But, in order for the program to solve for a fluid model, it is required to define pressure boundaries for at least two surfaces in the fluid domain where the fluid in question is allowed to flow: one for in-flow, and the other for out-flow. It is up to the user to define how restrained the pressure boundary conditions should be. To achieve a fluid model as realistic as possible, parameter ramping must be performed to find the right combination of pressure boundary conditions that are as constricting as possible, but still converge to a full solution. As previously mentioned, the inlet and outlet seen in the geometry are included for convergence purposes in the fluid dynamics model; these components are not physically present in the experimental apparatus.

Although the liquid xenon is almost completely still, a fluid model must be solved in order to consider the drag force on the ions' motion while performing particle tracing. We need to provide pressure boundary conditions for the inlet and outlet walls. It would also be possible to define it in terms of velocity instead, if this were a known value at each wall. The difference between the inlet and outlet pressures conditions are very small to minimize the amount of flow. Equation 3.18 represents the boundary conditions on the inlet and outlet.

$$\vec{n}^T \left(-p + \mu(\nabla \vec{u} + (\nabla \vec{u})^T)\right) \vec{n} = -\hat{p_o},\ \ \vec{u} \cdot \vec{t} = 0 \tag{3.18}$$

$$\begin{cases} \hat{p_o} \geq p_o & \text{Inlet Pressure} \\ \hat{p_o} \leq p_o & \text{Outlet Pressure} \end{cases}$$

If the selected pressure range is too small, convergence issues may arise. It needs to be large enough to converge, but as small as possible to prevent the introduction of unrealistic flow in the liquid xenon. To keep the liquid xenon inside the chamber around 133200 Pa, inlet and outlet pressures were set to $p_o = 133197.5$ Pa and $p_o = 133202.5$ Pa, respectively, while actively suppressing backflow. These parameters are generally kept constant throughout all of the performed simulations since they produced acceptable solutions. It can be difficult to find a converging pair of boundary conditions, especially if there are tight constraints from a practicality perspective.

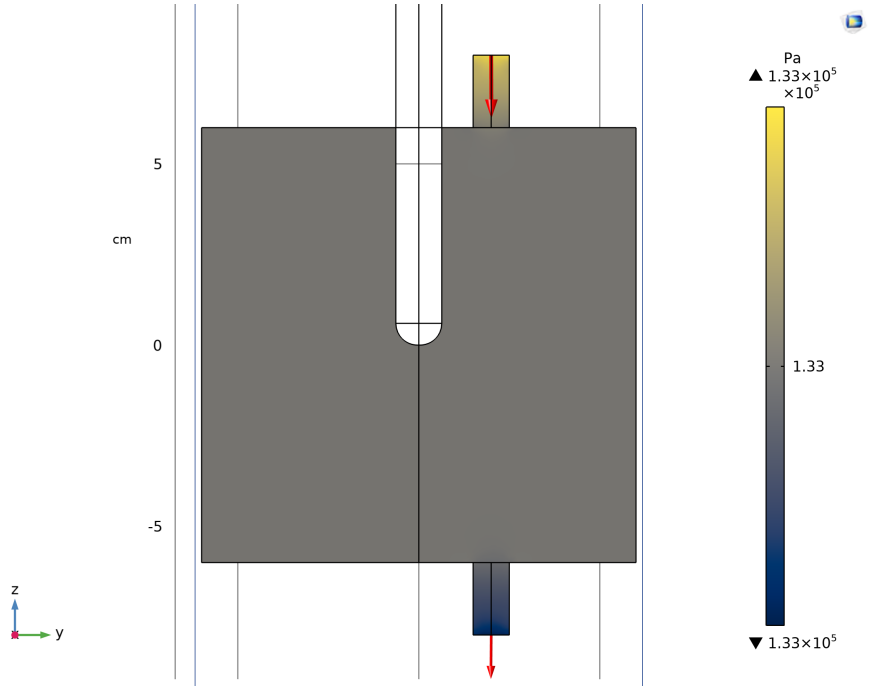

FIGURE 3.7: Liquid xenon pressure field (Pa) solved using creeping flow.

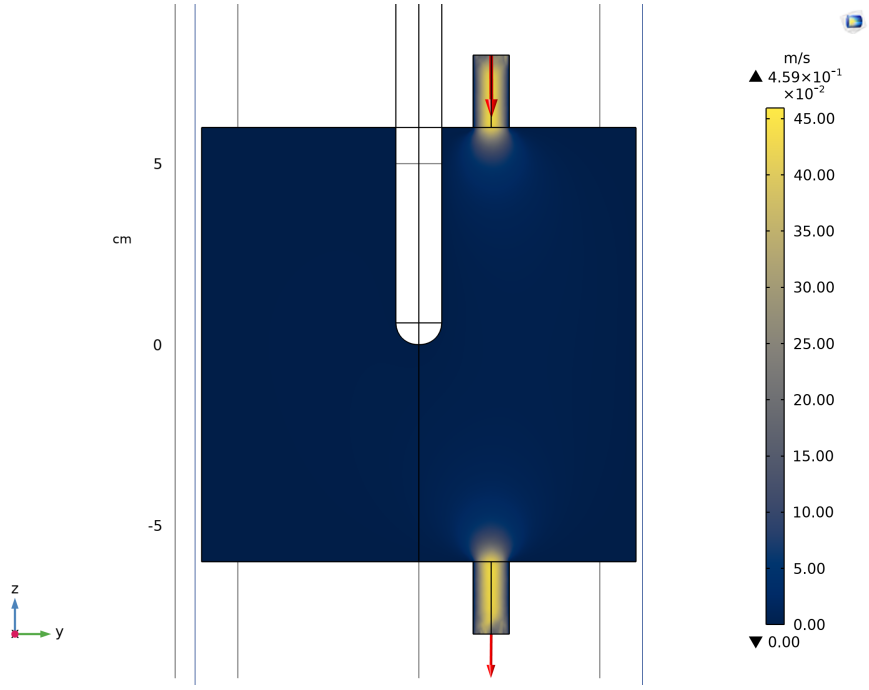

FIGURE 3.8: Liquid xenon velocity field.

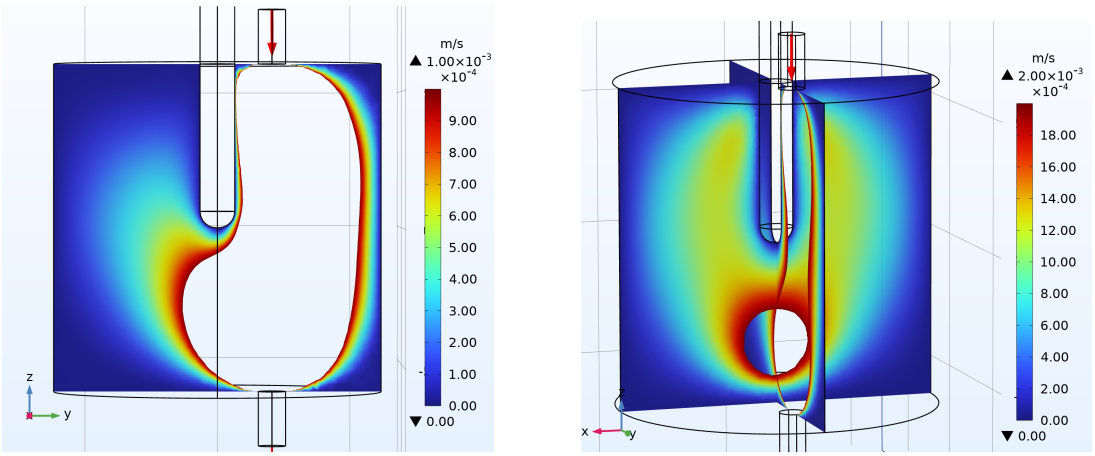

(A) Velocity < 0.001 m/s, yz plane view

(B) Velocity < 0.002 m/s

FIGURE 3.9: Enlarged velocity field map for liquid xenon solved with creeping flow, showing only the regions below a certain velocity threshold for emphasis of the flow field. The inlet and outlet pressures are $p_o = 133100$ Pa and $p_o = 133300$ Pa

The velocity field solutions are shown in Figures 3.8 and 3.9. At first glance in Figure 3.8, the velocity field seems to be uniform in the liquid xenon. Further investigations in Figure 3.9 show that there is slight flow on one side of the probe in Model A, which allows for fluid effect studies. These simulations are described in a later section.

The velocity and pressure field solutions for liquid xenon in Model B are shown in Figure 3.10, using the *Laminar Flow* fluid model. Laminar flow is when a fluid travels smoothly, in regular paths, where each layer moves past the adjacent layers with little or no mixing [116]. When operating at low R_e numbers (tending towards 0), COMSOL will automatically solve the Stokes equations for flow, identical to the *Creeping Flow* module. The differences between the two fluid models would be concerning the tolerances, and possibly the required mesh sizes.

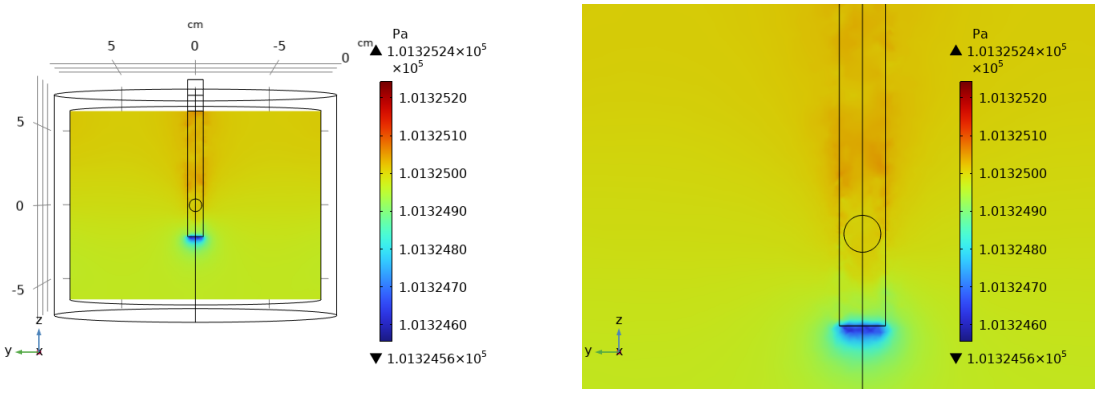

(A) (B)

FIGURE 3.10: The pressure solution (Pa) for liquid xenon solved using *Laminar Flow* The right shows an enlarged view focusing on the region near the probe tip.

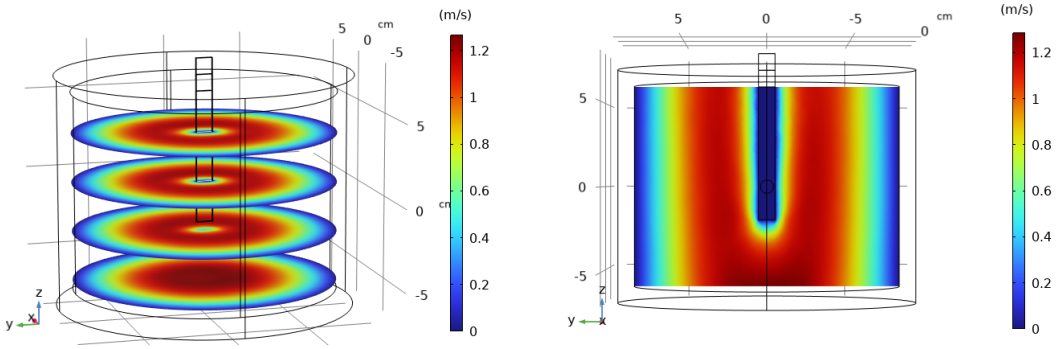

(A) (B)

FIGURE 3.11: The velocity solution for liquid xenon solved using a laminar flow model.

It seems that for the specific geometry in Model A, it is easier to arrive at a fluid solution when the surface area of the inlet and outlet are smaller if the pressure difference between the two is quite small– especially for a 3D model. This is most likely because creeping flow is the most restrictive fluid flow model. In Model B, if laminar flow is being solved, the solver is less affected by the larger inlet and outlet surface areas.

Model B is more suitable for solving gaseous mediums using laminar flow. Though, the same Stokes equations apply in these studies, and it is used to solve liquid mediums as well as gas. The level of precision/accuracy for the fluid solution can be tailored to the requirements of the specific study by choosing the more appropriate model.

At this stage, the simulation environment is ready for further complexities, such as *Particle Tracing*.

3.3.4 Particle Tracing

The *Particle Tracing* interface solves ODEs for particle positions and velocities as it moves through a liquid medium. Specifically, the *Particle Tracing for Fluid Flow* interface is designed for modelling microscopic particles in a background fluid [117]. It is defined only in the domain that includes the liquid xenon. Unless new forces that are not included in the model by default are defined, the solution is deterministic; the same particle trajectory is always given for the same set of initial conditions of the simulation.

The user is given the option to select which particle parameters to provide. For these purposes, specifications are made for the mass, diameter, and charge of the barium ions. The program does not recognize fluid displacement; the particles do not displace the fluid in which they are suspended [117]. Another assumption regarding particle size is made when modelling particle-wall interactions: the particles are assumed to be point masses when a particle-boundary interaction takes place [117]. The particle size is mostly used for any size-dependent forces that may be defined, and it plays an important role in defining the most suitable formulation of the equations of motion for the underlying physics of the problem at hand. Choosing the best formulation can reduce the computational cost, or improve the accuracy of a simulation. Thus, modelling particle tracing begins with this fundamental choice, starting with making an estimation of Lagrangian time scale τ_p for the particles.

This value depends on the particle density ρ_p, particle diameter d_p^2 and dynamic viscosity μ of a given fluid [118]:

$$\tau_p = \frac{\rho_p d_p^2}{18\mu}. \tag{3.19}$$

Comparing this time scale to the range of desired solution times helps decide how important inertia is in the problem. If the range of simulation time is much larger than the velocity response time (by a factor of several thousand), then the *Newtonian, ignore inertial terms* formulation is the best option. This is the case for Ba ions in LXe, as well as many examples involving particles of sizes on the micron scale in viscous fluids. This formulation is used for all of the particle simulations. The equations of motion for the particles can be derived by considering the classic example of a spherical particle subjected to Stokes drag. For this particle of mass m_p (kg), and neglecting gravity, the equation of motion can be written as:

$$m_p \frac{d^2\vec{q}}{dt^2} = 3\pi\mu d_p(\vec{u} - \vec{v}), \tag{3.20}$$

with q (m) as the particle position vector, $\vec{u}$ is the velocity of the fluid, and $\vec{v}$ is the velocity of the particle ($d\vec{q}/dt$).

Under the assumption that the particle size remains the same, thus fixing d_p and m_p, and given the mass of a sphere defined by $m_p = \frac{\pi}{6}\rho_p d_p^3$, Equation 3.20 can be rewritten as:

$$m_p \frac{d^2\vec{q}}{dt^2} = \frac{1}{\tau_p} m_p(\vec{u} - \vec{v}). \tag{3.21}$$

In Equation 3.21, the τ_p has units of time, and is already defined by the expression introduced in Equation 3.19. In a fluid with a spatially uniform $\vec{u}$, the difference between the $\vec{v}$ and $\vec{u}$ decays exponentially with a time scale τ_p. Evidently, the d_p^2 dependence of τ_p suggests that large particles would have a much greater velocity response time, and terminal velocity; this means that larger particles are capable of moving greater distances before the drag force has any effects on their motion, and smaller particles match the fluid velocity much sooner. It is essentially a scale indicating how fast a particle accelerates in the case where its velocity is not equal to the velocity of its surrounding fluid.

For Ba in LXe, with a particle density of 3630 kg/m^3, an ion diameter of 8.7e-10 m and a fluid dynamic viscosity of 0.0005 Pas, the Lagrangian time scale is 5.79e-27 s. Therefore, for a simulation duration on the order of seconds, millions of time steps may be necessary to come to a solution, or more if $\vec{u}$ is not spatially uniform. This example would be unnecessarily difficult to solve, because the Ba-ions would reach the same velocity as the LXe in a fraction of a second, but taking such small time steps would still be required [119]. Although time steps are specified prior to running a simulation, it is up to the solver to take smaller time steps, if required, to get an accurate solution, while not necessarily storing all of the steps.

To avoid this problem, the *Newtonian, ignore inertial terms* formulation would simplify the equation of motion by assuming that dynamic equilibrium is achieved instantaneously between the particle and the velocity of the fluid. As a result, rather than solving

$$m_p \frac{d^2\vec{q}}{dt^2} = 3\pi\mu d_p(\vec{u} - \vec{v}) + \vec{F}_{gravity} + \vec{F}_{external}, \tag{3.22}$$

where $\vec{F}_{external}$ encompasses all of the forces exerted on the particle except for drag and gravity, only a set of first order equations for the particle position is solved. Thus, where $\frac{d\vec{q}}{dt} = \vec{v}$, the velocity of the particles is initially defined as

$$\vec{v} = \vec{u} + \frac{\vec{F}_{gravity} + \vec{F}_{external}}{3\pi\mu d_p}, \tag{3.23}$$

where it is assumed that the drag force is balanced with all of the forces applied on the particle, and then the position is found by integrating $\vec{v}$ over time. This simplification is only correct when the particle inertia is insignificant in the given context, usually when τ_p is extremely small compared to the simulation time [118].

When simulating with this formulation, less forces are available to incorporate into the model because any force that is velocity dependent or dependent on the relative positions of other particles is excluded. Nonetheless, the most significant forces at play for small particles in a viscous fluid are the drag force and the electric force.

User defined forces are also possible to include if necessary, using one's own input equations. The user is also able to decide what particles of a given distribution are exposed to a defined force. For example, this feature would be helpful in a situation where within a distribution of different particles, a selection of particles are sensitive to certain forces and some are not.

The motion of Ba-ions in LXe is dominated by the drag force. The fluid flow solution calculates the Stokes drag force, F_D, that the Ba ions are subjected to during their journey to the electroprobe, given by

$$\vec{F_D} = 6\pi\mu R\vec{v}, \tag{3.24}$$

where μ is the dynamic viscosity of LXe, R is the barium particle radius, and $\vec{v}$ is the LXe flow velocity relative to Ba. In COMSOL, this relation is rewritten as Equation 3.25.

$$\vec{F_D} = \frac{1}{\tau_p} m_p \left(\vec{u} - \vec{v}\right), \tau_p = \frac{\rho_p {d_p}^2}{18\mu} \tag{3.25}$$

The electric force is defined by Equation 3.26:

$$\vec{F_e} = eZ\vec{E}, \tag{3.26}$$

where e is the elementary charge, Z is the charge of the particle species moving through the liquid, $\vec{E}$ is the electric field as defined from a previous study. It is possible to import the previously solved dataset from the *Electrostatics* interface, and set it to only affect the Ba ions. In addition, the charge of the ions must be defined, or else the particles will ignore any electric fields to which they are subjected. The particle charge is a useful parameter for troubleshooting purposes, as the effects of increasing Z to higher values are immediately observed for particles in an electric field, i.e. the particles would travel faster with a higher Z, which may be a reassuring test. Similar tests may be performed by toggling a particle's mass higher or lower.

Once the forces acting upon the particles are defined, it is time to create particle distributions to release into the simulation. There are many ways to define the particles in COMSOL. One way to fully control the initial positions and the amount of particles is by importing a file that specifies this information using the *Release from File* node. Different particle distributions are used in these simulations depending on what study is being performed: either a cylindrical distribution of Ba ions created in Python, or a

1cm × 1cm × 1cm Ba ion cloud as generated by SRIM. These distributions will be shown in the next sections. The user also has the option to release the particles in a given distribution more than once, over a range of desired time steps.

As a trivial example, a beam cross section with 10^4 $^{139}Ba^+$ ions is arranged with Python and placed near a biased probe tip (-8 kV); all of the particles are drifted towards the probe, as seen in Figure 3.12

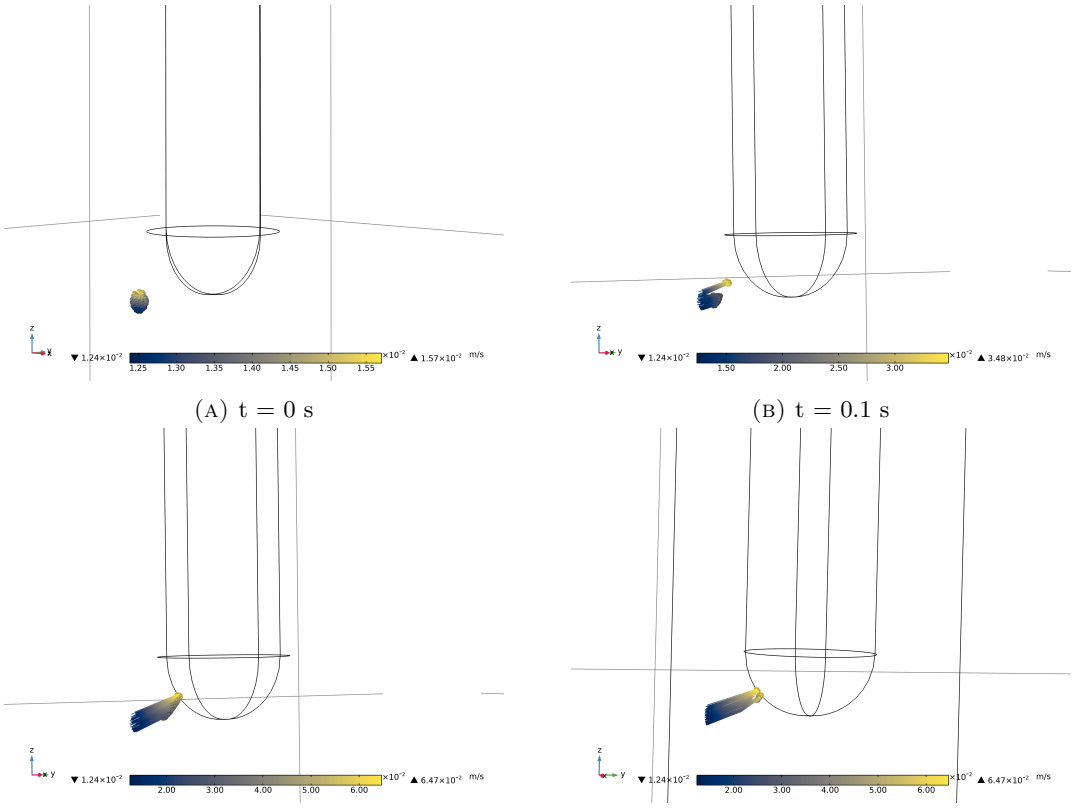

(A) t = 0 s (B) t = 0.1 s

(C) t = 0.2 s (D) t = 0.3 s

FIGURE 3.12: An example of the particle trajectories of a collection of $^{139}Ba^+$ ions in LXe travelling towards a biased probe tip (-8 kV). At nearby distances to the probe, the attraction efficiency is 100%, within a very small time interval.

For Ba-tagging developments, it is important to be able to track an ion in a fluid. Simulations enabling particle tracing are advantageous to the development of the electrostatic probe approach because a knowledge of the location of Ba ions within a LXe environment is necessary to perform ion extraction. Additionally, on a broader scope, a knowledge of the Ba ion mobility in LXe is necessary in order to know where to reach in the detector volume to tag a Ba-ion in the event of a rare $\beta\beta$ decay [88].

The ion mobility acts as an all-encompassing value describing an ion's motion in a fluid, from a computational perspective; ensuring that the correct ion mobility value is used,

enables one to trust the results of a particle tracing simulation. However, there is no direct way to set this value in COMSOL. The ion mobility is varied through setting the particle diameter until it matched experimental mobility values. This corresponds to the notion that Ba ions undergo a "Snowball Effect" when propagating through LXe, likely as a result of the electrostrictive pressure, which leads to an agreement in the experimental mobility values for Ba^+ in LXe with the Atkins cluster model for positive ions in non-polar liquids [88]. Meaning, the Ba ions' effective radius increases in LXe, from one or more layers of Xe atoms around the ion solidifying, forming a cluster or snowball structure.

From Ba ion mobility studies in LXe, the electrostriction may have other effects on the mobility, such as increasing the liquid density and viscosity around the ionic cluster [88]. These effects are neglected in these COMSOL simulations.

From literature, the mobility of alkaline earth ions, including Ba^+ ions, in LXe is measured experimentally for the first time and found to be 2.11e-4 cm^2/Vs [88]. To convert the mobility into a tangible value for simulations, the particle size is extracted by equating the electric and drag forces:

$$F_E = F_D, \tag{3.27}$$

$$eE = 6\pi\mu R v, \tag{3.28}$$

where e is the elementary charge, E is the electric field, μ is the viscosity of the LXe, R is the Ba ion radius, and v is the relative velocity between the Ba and the LXe. The mobility is given as v/E from Equation 1.24, which substituted in Equation 3.28 to get an expression relating the mobility and the radius. For $^{139}Ba^+$ in LXe, this corresponds to a particle diameter of 1579.45 pm at a temperature of 165 K, and dynamic viscosity of 0.000510037 Pas.

The relation between ion mobility and radius is described in Figure 3.13. The software program does not recognize that the ion size can vary if you input different charges for a certain isotope. Rather, the given charge value is used for electrostatic purposes only. The mobility values in Figure 3.13 are obtained from a linear fit, where the uncertainties of the simulated ion velocities are almost negligible due to machine precision, and the values are chosen to produce a reasonable linear fit. The curve demonstrated in Figure 3.13 is fit with Equation 3.28, and as a result one may extract the elementary charge value e and compare it to the accepted value 1.60217663 $\times 10^{-19}$ C. For this fit, calculating e serves as another method to check the simulation parameters as a whole. The extracted elementary charge from the curve in Figure 3.13 is within ~3% of the accepted value. Not shown in the plot, the same relation was simulated for $^{139}Ba^+$+, which yielded similar results.

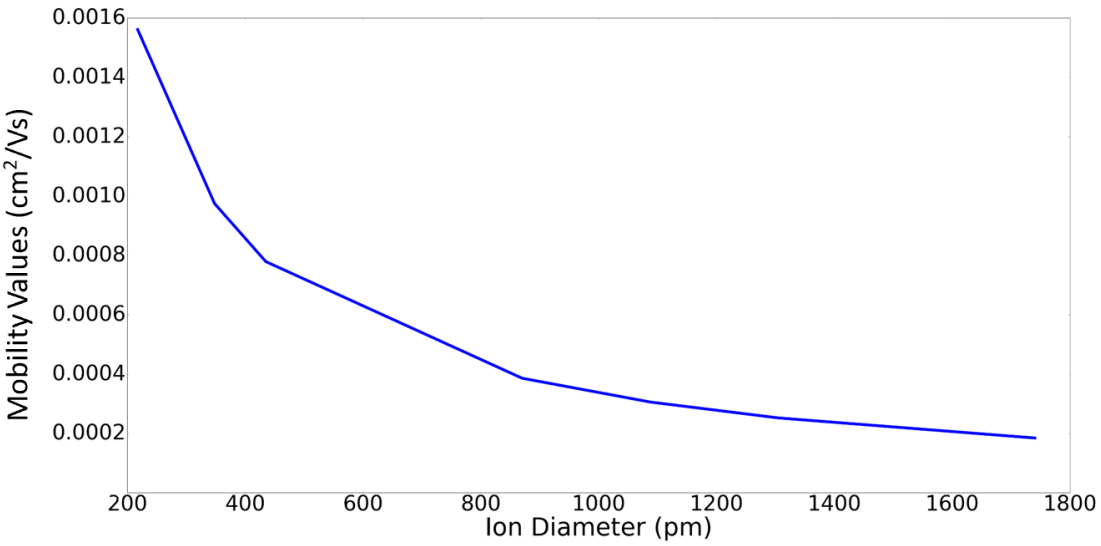

FIGURE 3.13: Simulated Ba ion mobility for various ion sizes.

This relation in Figure 3.13 would also follow the same trend as the charge state of the Ba as a function of ion diameter. In a 2^+ charge state or higher, the cluster would be larger, and thus the mobility would scale with it. Essentially, varying the ion diameter is an avenue to indirectly study the charge state effects of an ion species' mobility through a medium.

To count the ions at the probe tip, either an *Accumulator* or *Particle Counter* is used, which is a separate node to define a boundary or domain, in this case the probe tip, as a region where the released particles are to be recorded if there is a wall interaction. The exact locations of the wall interactions, within this specially defined region, are also recorded by the program.

Ultimately, the goal of these simulations is to determine the allowable distances from the probe tip for the Ba ions to begin their journey, while maintaining a 100 % extraction efficiency in a reasonable amount of time, and probe bias setting. The uncertainties on all of the parameters supplied to the simulation are not considered at this point of the project. The uncertainties for certain parameters, such as the extraction efficiency, can be estimated by varying controllable parameters, such as the voltage applied to the probe, and checking whether or not this changes the extraction efficiency. Similar approaches can be taken for parameters that are not controlled experimentally, through the introduction of random numbers, for example as an offset to the initial ion positions.

Next, general studies of the simulation environment are performed to characterize the geometry and the fluid effects.

3.4 Attraction Efficiency Simulation Results

Given any probe bias setting, it is helpful to first find the maximum distance from the probe tip that allows for ions to be attracted. Without knowing this "capture radius", it would be difficult to get a sense of how sensitive the ions are to the electric field, especially at greater distances. A strategy to finding the capture radius for any probe bias setting is to generate a uniform cylindrical particle distribution to place around the probe tip region, ensuring that the particles extend beyond the estimated capture radius. The particle distribution, called "Distribution A", shown in Figure 3.14 is used for a variety of studies in Model A. The scale is readjusted when importing into COMSOL.

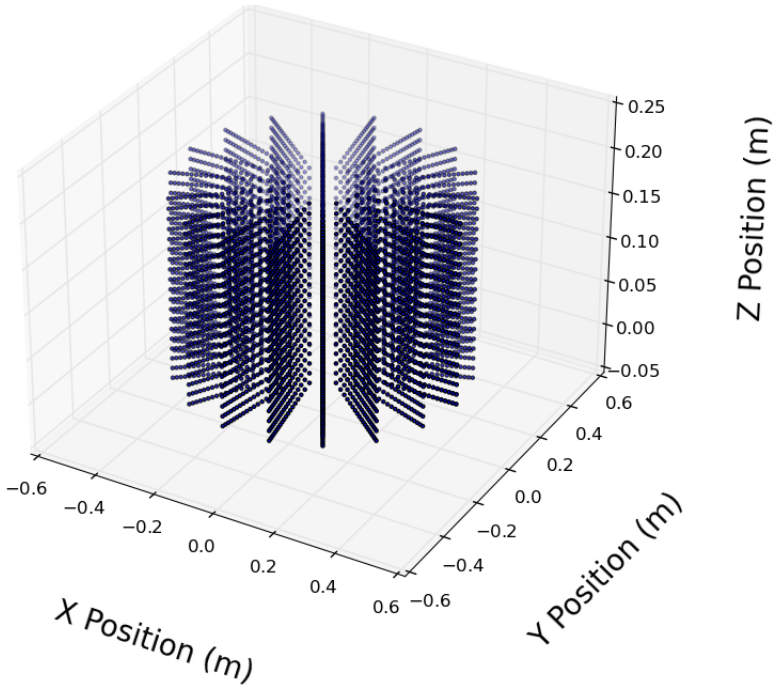

FIGURE 3.14: Distribution A: A particle distribution generated with Python. There are 6859 particles included. The units shown on the axis are rescaled once they are imported into the COMSOL environment.

There is blank space in the centre of this distribution reserved for the probe (probe not shown). The 6859 particles span a radius of 2 cm around the probe tip, leaving 2 mm of space between the probe surface and the particles, and 1 mm between each other in the radial direction for the first several rings starting from the centre. As the radial distance increases, the spacing until the next set of particles that share an r value becomes gradually smaller. This was done because it was of interest to find the capture radius within units less than ∼mm distance scales. After this distribution is imported into COMSOL, it is possible to filter out and view only the particles that connect a source (initial distribution) and a destination (boundary on the probe) using a logical

expression in the *Filter* node of the Particle Trajectories plot. It is also possible to shift the distribution around the geometry, to cover a different region from the probe.

3.4.1 Probe Bias Effects on Extraction Efficiency

The following study was performed to investigate the effects of probe bias on the number of $^{139}Ba^{+}$ ions that are attracted to the probe tip, while submerged in LXe. In this case, only the probe tip is surface is biased. Distribution A is imported into the simulation twice, in order to cover the positive and negative z-axis regions about the z=0 plane; there are 13718 ions initially surrounding the probe.

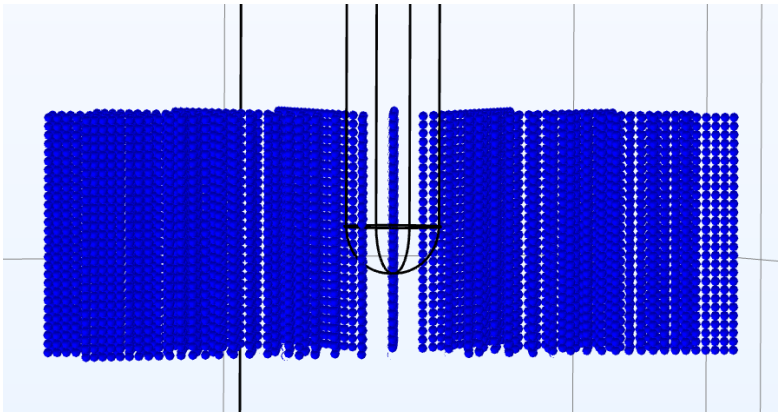

FIGURE 3.15: The initial particle distribution surrounding the rounded probe tip in Model A.

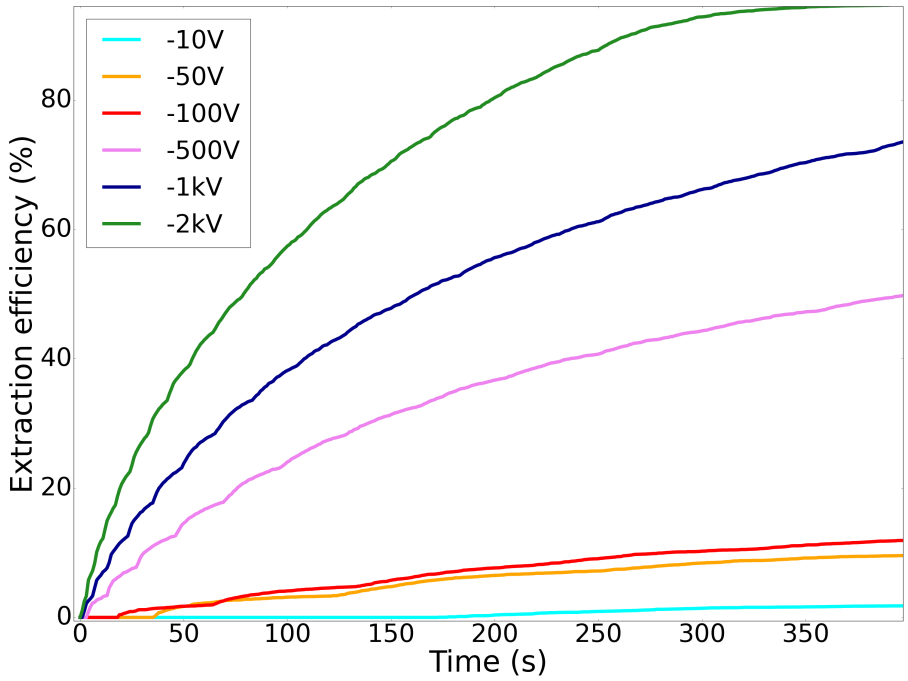

FIGURE 3.16: The extraction efficiency as a function of time for various probe bias settings.

As expected, more ions are attracted to the probe faster for -2 kV compared to the lowest simulated bias -10 V. Even for a bias of -2 kV, a perfect efficiency is not achieved for this particular particle distribution. In the event of ion loss for this simulation, the particles are found on the walls of the LXe vessel or elsewhere in the LXe. Figure A3.1 in Appendix C includes additional data for higher biases, up to -10 kV. Such large voltages are not realistic for the experimental apparatus, but it demonstrates that biases from -4 kV to -10 kV are all sufficient to attract 100 % of the ions surrounding the probe.

It is also worth exploring the effects of different electric field configurations on the ion extraction efficiency and the capture radius. One variation that was made to the electric field was biasing the top of the copper vessel, and allowing the attached probe to float (take the voltage value of the cathode). Otherwise, the same temperature and pressure conditions for the LXe medium are used, as well as the probe geometry, Model A, and position in the LXe.

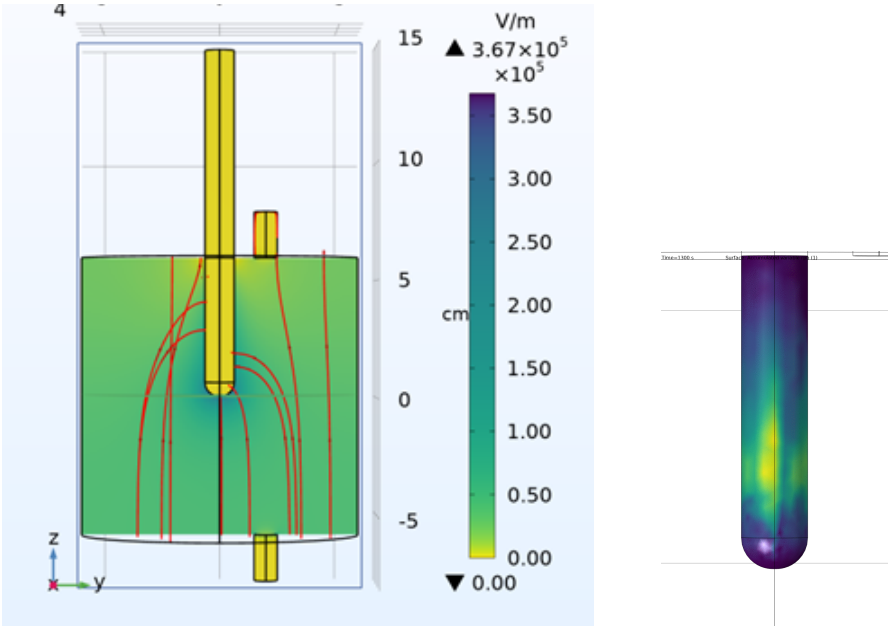

(A) (B)

FIGURE 3.17: (A): The electric field (V/m), given the whole probe is biased to -4 kV. (B): The ions' final positions on the probe, with the bias set to -5 kV.

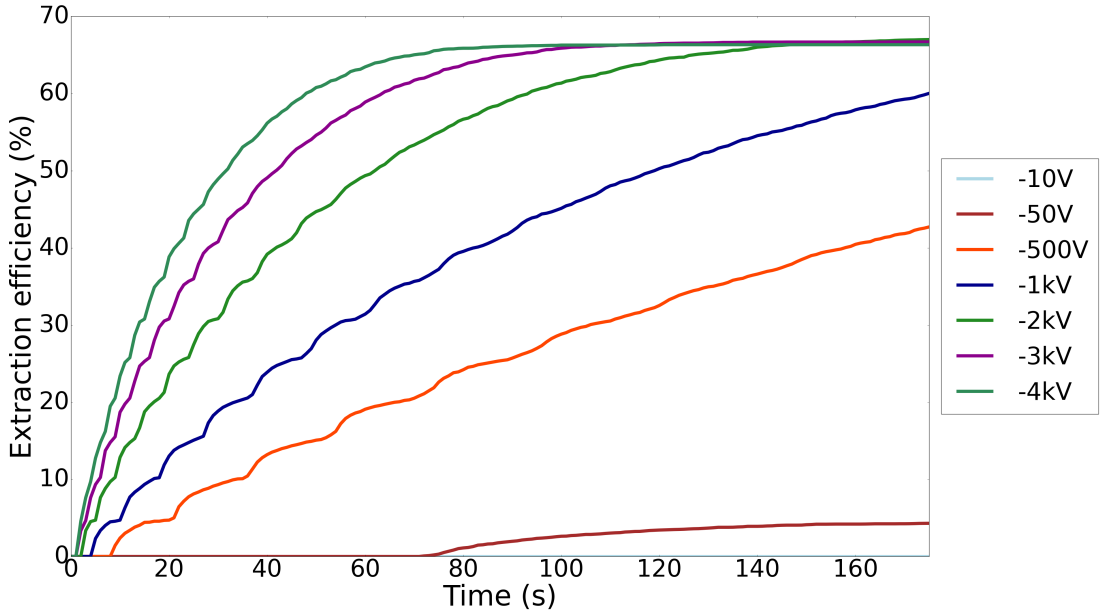

FIGURE 3.18: The extraction efficiency as a function of time for various probe bias settings, with a biased probe body and tip.

The extraction efficiencies are largely similar for these two electric field configurations. For example, with only the probe tip biased at -500 V, ∼40% efficiency is achieved after 250 s, compared to 180 s for the whole probe biased at -500 V. Also, since the electric field is not converging onto a localized region on the probe when the entire probe is biased, the ions are collected along the shaft, as shown in Figure 3.17. Similar end locations of the ions are observed for all of the probe bias values, since the electric field follows the same direction, just with varying magnitudes. This result would have implications for the post-ion extraction γ-detection setup, and the simulations suggest that it is preferable to bias the probe tip only to attract the ions to a localized region.

In Figures 3.16 and 3.18, it appears that there is oscillation-like behaviour for the initial time steps, up to ∼80 s. One likely explanation for these ripples is that they are an artifact from the initial ion distribution used, where the particles at closer radial distances to the probe were also spaced slightly further apart than the particles at the outer edges of the distribution. Each ripple observed may correspond to one set of these inner r values, and since the spacing between the ion "rings" increases as one moves outward in the distribution, more time is required to drift the ions as the radial distance increases, so only one batch of ions for one certain r value is seen at the probe at a time, until the spacing between the rings becomes so small that it is indistinguishable. This may also be why at the top of each small ripple, there is a plateau, which could mean that all ions of a certain r reached the probe– a 100 % efficiency was achieved for that particular radial distance from the probe.

3.4.2 Varying Probe Shapes and Probe Depth

Similar to changing what components of the setup are biased, the electric field shape could be varied by changing the probe's shape. Simulations were performed to consider the extraction efficiency using a flat rod-shaped probe tip. Figure 3.19 shows the biased flat face of the probe, where the electric field lines (in red) meet.

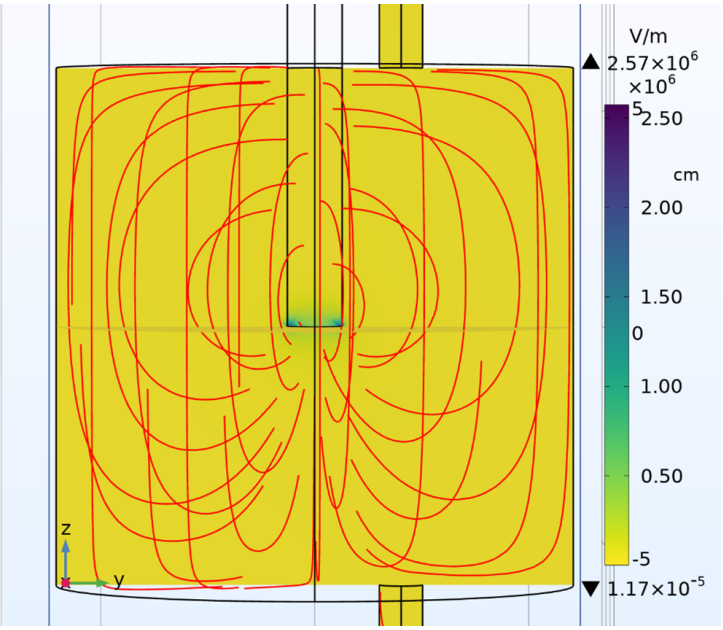

FIGURE 3.19: The electric field (V/m) in the case where the flat cylindrical face at the bottom of the probe is biased to -2 kV. The red lines represent the electric field direction.

When particles are released from Distribution A in this setting, they all follow the electric field and settle on the flat face of the probe. No particles arrive to any other region of the probe; they are all localized to one surface, and this may serve as advantageous when it comes to the detection portion of the experiment. The efficiency of the flat rod probe was compared to the regular rounded probe used in Model A, and the whole probe bias configuration, as seen in Figure 3.20. When using ion Distribution A, there is an advantage to using the biased rounded probe tip, which is capable of reaching higher efficiencies compared to the flat rod probe within the same given time frame (for a general, uniform ion distribution).

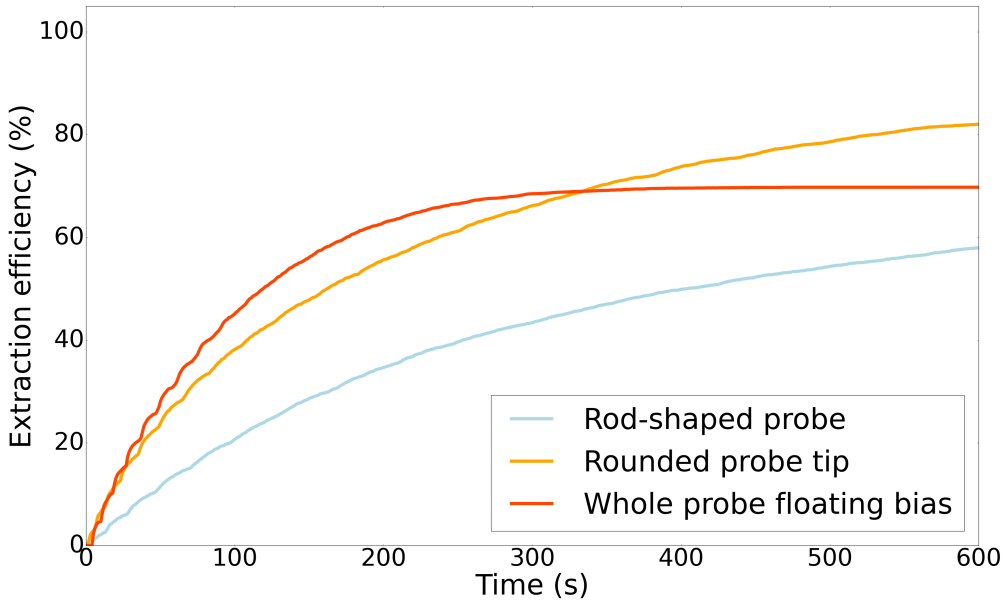

FIGURE 3.20: The extraction efficiency as a function of time for three different probe types: a biased rounded probe tip (as in Model A), a flat rod with the flat face biased, and the whole probe as in Distribution A biased.

Other variations of probe shapes were also considered, such as a mushroom-shaped probe tip. A similar electric field is produced in the case where the mushroom-shaped probe tip is biased as the flat rod example in Figure 3.19. Generally, the ideal setup would involve biasing a small part of the probe to allow for an electric field shape that converges at a confined region. From simulations, there are no significant differences found in the ion travel times, and ultimately extraction efficiency, if this general rule is followed.

Simulations were also performed to investigate the effects of the probe's depth (along the z-axis) on the ion extraction efficiency of a general particle distribution. Using Model A, the pressure difference between the inlet and the outlet is set to 5 Pa, to minimize the amount of fluid flow in the LXe around the probe. An example of this simulation is demonstrated in Figure 3.21, where the probe tip is placed at z = 2 cm and biased to -500 V. The simulation was run for a collection of z values, excluding z = -1 cm due to solution convergence errors. It is possible that the solution for z = -1 was difficult to compute because it would have been the best case scenario for the efficiency, and it overwhelmed the program during runtime.

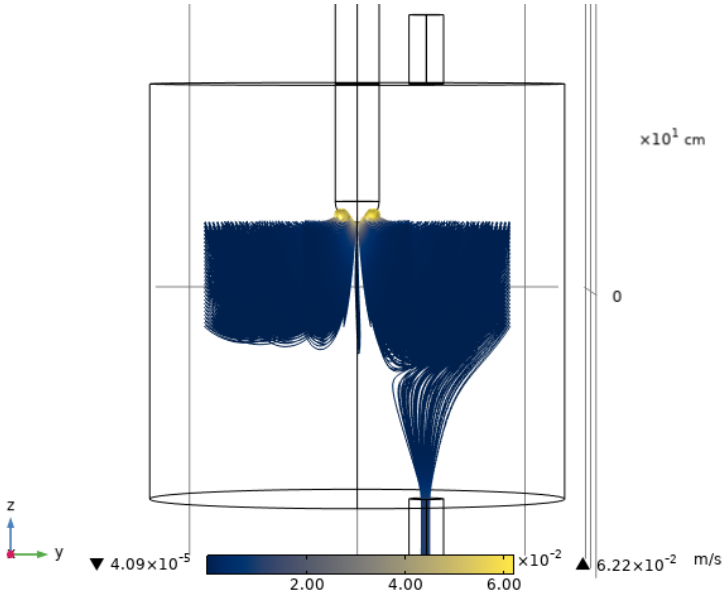

FIGURE 3.21: The rounded probe in Model A, after running the simulation with particles from Distribution A surrounding the probe shifted up 2 cm from the initial position. There is particle loss on the outer edges of the distribution on the right side, as is expected as a result of the minimal flow on the side including the inlet and outlet.

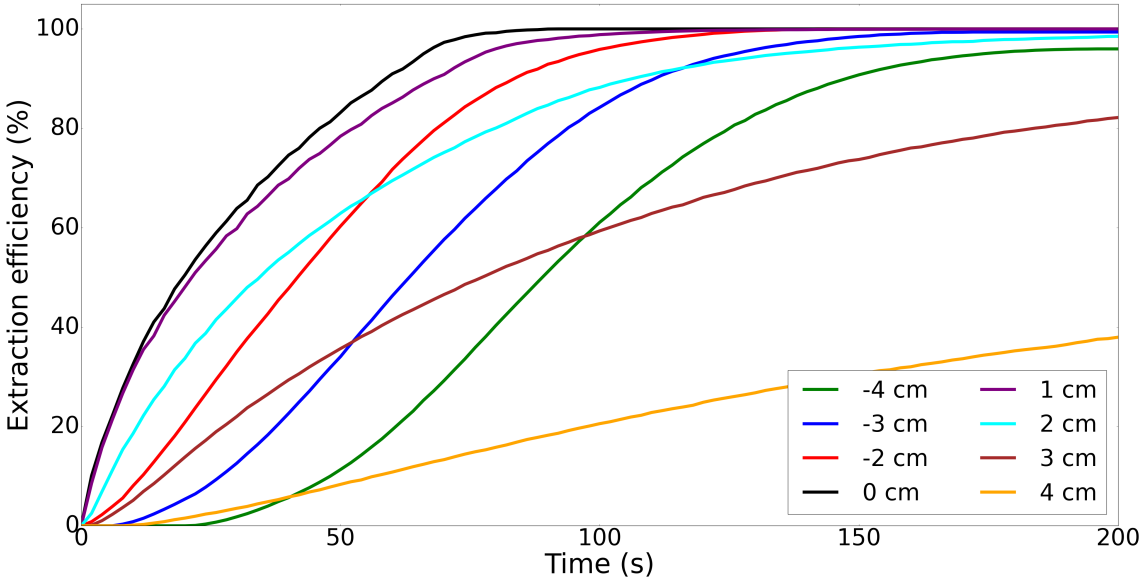

FIGURE 3.22: The extraction efficiency for various probe depths at -8 kV bias, using a rounded probe tip. The depths correspond to the z-axis.

In reality, the implanted beam ions will not resemble Distribution A. When comparing the same distance magnitude pairs (-2 and 2 cm, -3 and 3 cm, -4 and 4 cm), higher extraction efficiencies are achieved for the negative counterpart, likely as a result of the effect of gravity on the ions. As shown in Figure 3.22, for z values of equal distance but opposite sign, a cross-over point is observed in all 3 simulated pairs (-2 cm and 2 cm, -3 cm and 3 cm, -4 cm and 4 cm), but the negative z position out of each of these pairs continues on to produce a 95-100 % extraction efficiency, where the positive z counterpart stagnates. For z = 4 cm, this stagnation occurs at efficiencies as low as ∼40 %. This finding might suggest that in reality, the z component of the probe location in the LXe medium should be less than that of the ions. Note that Distribution A extends to a wider distance from the probe tip than the realistic implanted ions would, but these effects may still extrapolate to smaller particle distributions ($\leq$ 0.5 cm from the probe tip).

Most of the particle loss is observed on the right side of the probe that includes the inlet and outlet, but the effects of this are minimized for ions closer to the probe tip (for both the z and radial directions).

3.4.3 Fluid Velocity Field Effects on Extraction Efficiency

The simulations in this subsection are all performed with Model A, with -8 kV on the rounded probe tip. Initially, these studies were done to examine the initial positions of the particles that were successful in arriving on the probe tip. Upon further investigation, it was found that small flow fields present in the LXe medium were affecting the ion extraction efficiency for large ion distributions ($\geq$5 cm from probe), using a test ion distribution. The initial particle cloud Distribution A was then separated into four sections, as labelled in Figure 3.23, to study the trajectories and final destinations of the ions depending from where they were initially released. Essentially, the purpose of these studies is to determine the effects of a slight fluid flow on the extraction efficiency, to quantify the effect of the medium's flow on the capture capabilities of a given probe setting. In reality, there should be no turbulent flow or fluid circulation in the IC, but minuscule ($\sim$ μm/s) thermal currents are always introduced in the LXe due to temperature gradients between the outside walls of the vessel and the LXe volume.

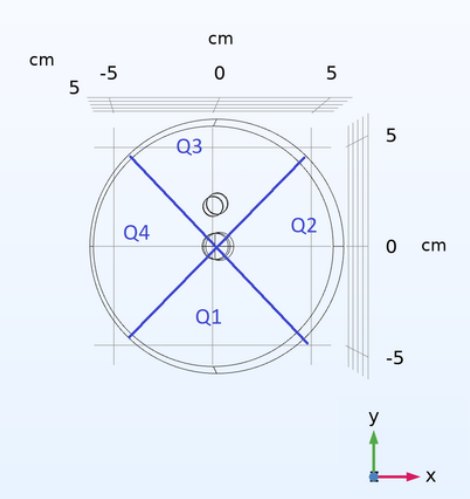

FIGURE 3.23: The boundaries for the four groups of particles within Distribution A. Quadrant 3 (Q3) contains the inlet and outlet features, and the majority of the fluid flow effects on the particles. By dividing Distribution A into quadrants, it is possible to compare the extraction efficiencies depending on the starting location around the probe.

The magnitude of the fluid flow is varied by the pressure settings at the inlet and the outlet boundaries. The larger the pressure difference between the inlet and outlet, the greater the fluid velocity field, specifically on the LXe regions in Q3, as shown in Figure 3.9. By decreasing this pressure difference, until the fluid solution no longer converges, the symmetry of the ion distribution is restored which demonstrates a dependence on the fluid flow for the capture radius. These simulations were performed for a wide range of pressure differences, from 3 Pa to 200 Pa. In addition, the data was taken for three different variations of Distribution A: only the positive z ions (called the "top"), only the negative z ions ("bottom"), and the whole distribution as is ("top and bottom"). The redundancy is meant as confirmation method, to verify that the same ion behaviour is observed when the subregions are run separately and together.

As the pressure difference is decreased, more ions are found to reach the probe tip. For pressure differences up to Δ P = 200 Pa, this results in a flow large enough to dislodge some of the outer ions in the distribution, which is observed on the left-side of the central plot of Figure 3.24. The computed LXe velocity in this case is $\geq$ 3 mm/s. As ΔP decreases to 3 Pa, the symmetry is restored about the y = 0 axis for the given set of particles; this pressure difference corresponds to a current $\leq$ 0.3 mm/s.

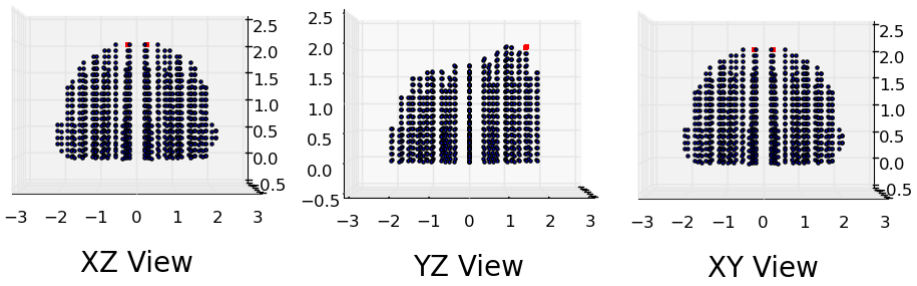

FIGURE 3.24: Three views of the initial positions of the positive z particles of Distribution A that are capable of reaching the probe tip under the given conditions. The outlines of the ion cloud find the "capture radius" when -8 kV of voltage is applied to the probe tip surface. The yz-plane view shows the asymmetry that arises (reflected over y = 0 cm) when fluid current is introduced, by a $\Delta P = 200$ Pa difference between the set inlet and outlet pressures. The labelled red points in each of the three plane views shows the particle with the greatest distance magnitude from the probe tip.

After investigating the initial ion locations by quadrant, it is clear that Q3 has the lowest extraction efficiencies across all of the fluid flow fields (introduced by varying the pressure difference between the inlet and outlet). For the three different variations of Distribution A (top region, bottom region, and simultaneous top and bottom regions), this finding is consistent. Also, the LXe region furthest from the affected quadrant, that is Q1, experiences the least ion loss when currents are introduced, up until pressure differences ≥ 100 Pa. It could also be possible that the fluid field pushes some ions, that would have otherwise gone elsewhere, towards the scope of the capture radius around the probe tip (where the electric force overpowers the current).

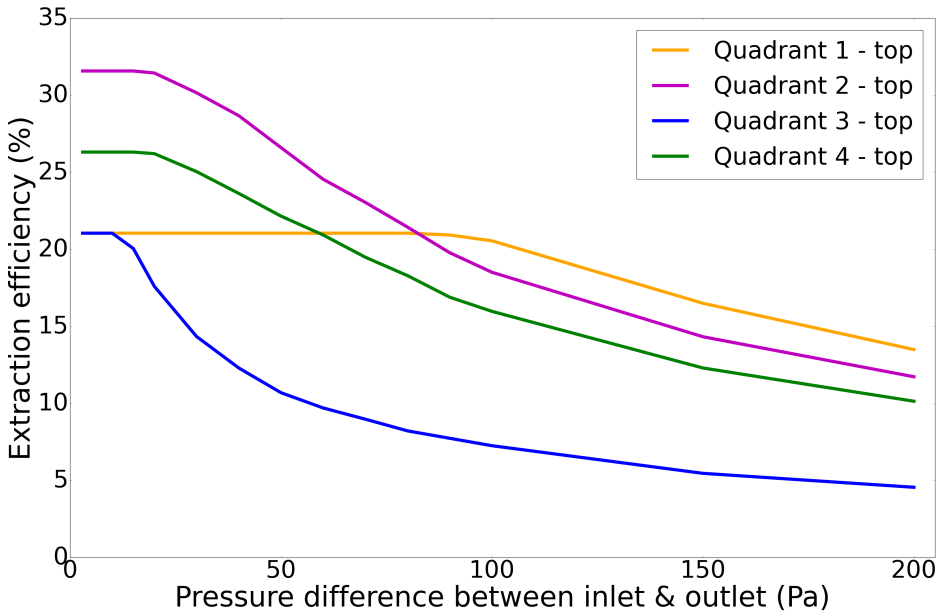

FIGURE 3.25: Ba ions at probe tip classified by their initial positions within the LXe, for all z > 0 ions.

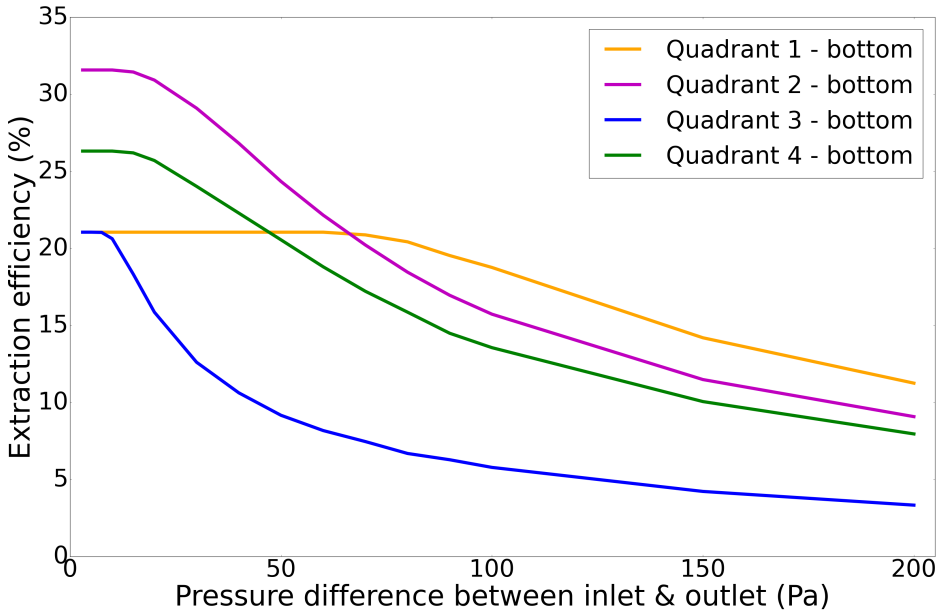

FIGURE 3.26: Ba ions at probe tip classified by their initial positions within the LXe, for all z < 0 ions.

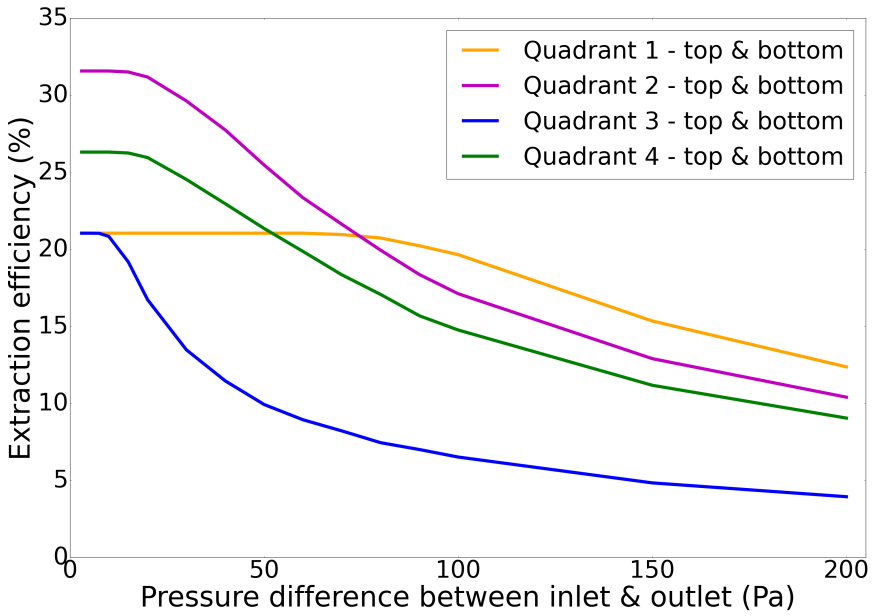

FIGURE 3.27: Ba ions at probe tip classified by their initial positions within the LXe, with positive and negative z ions distributions run simultaneously.

As a verification method, the same simulation was performed for two other particle datasets: one with a 50% reduction of particles and one with a 25% reduction. The Ba ion initial positions are also separated by quadrant in Figure 3.23. Given that the same trends are observed in Figure 3.28 as in Figures 3.25, 3.26, and 3.27, it confirms that space charge effects are not considered in the simulation, for the amount of ions present ($\sim$ 13,000 total ions for both top and bottom distributions together).

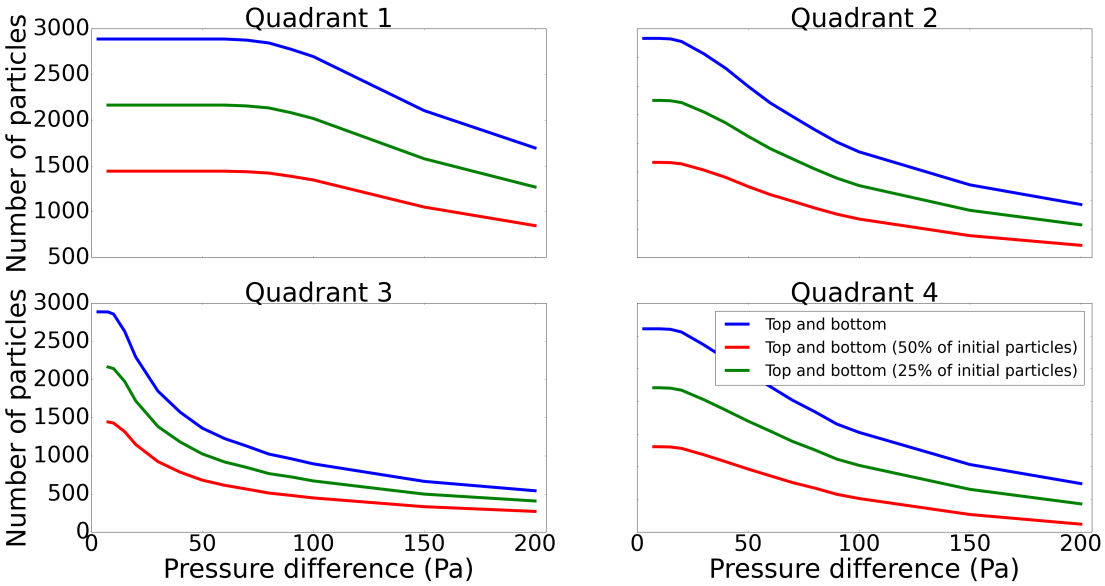

FIGURE 3.28: The number of ions extracted that originate in each quadrant for the top and bottom (simulated together) ion distributions, as well as for reduced distributions. The number of ions scales with the percent reduction (50% and 75%) of the original distribution.

Since it seems that only the outer ions in the cloud are affected by the currents, the radius of interest from the probe tip can be adjusted to compare the ion extraction efficiencies. As the radius from the probe tip increases, there is a sharper drop in the extraction efficiency for larger fluid fields, as shown in Figure 3.29. For ions within 0.53 cm from the edge of the probe tip, these LXe currents do not have any effects on the extraction efficiency even at the greatest (> 5 mm/s) applied velocity fields.

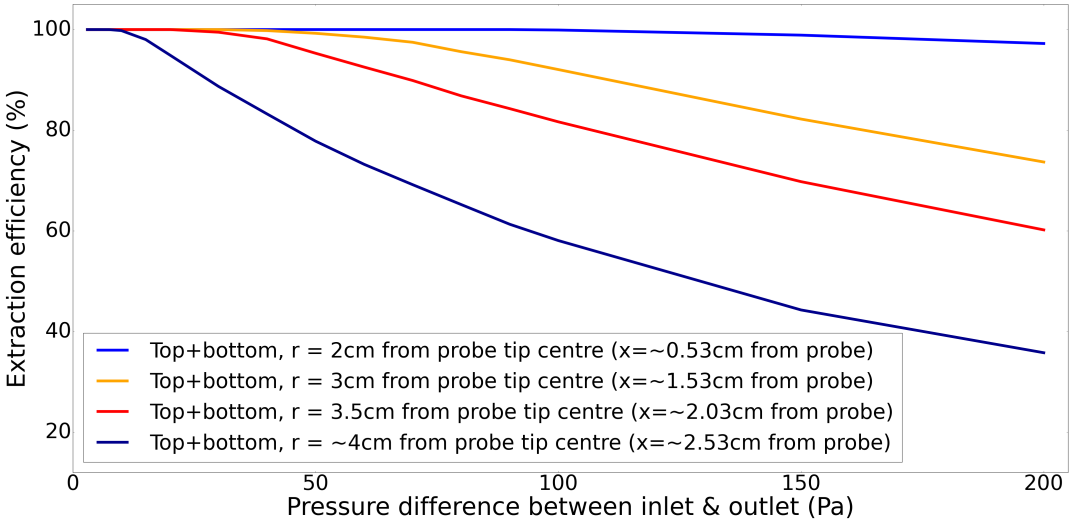

FIGURE 3.29: The effect of the currents on the extraction efficiency in the LXe volume for varying probe distances for Distribution A.

The same studies can be repeated for a reversed fluid field direction by redefining the inlet and outlet regions in the vessel's geometry and their respective initial pressures. The same trends are observed in this case.

To conclude, the precise capture radius of a given model may be found by passing a large, finely spaced particle distribution into the simulation, and then filtering out the successful particles (those that interact with a specified boundary) with logical expressions in COMSOL. A Python script was written to find the capture radius of any combination of probe tip bias and probe shape. Additionally, the introduction of small thermal currents to the LXe environment shows no significant effect on the ion extraction efficiency for realistic drift distances of about $\sim$ 1 cm from the probe.

3.4.4 Effects of Proximity to Probe on Extraction Efficiency

Given the information in the previous several studies involving probe bias and the fluid effects, these simulations can be further refined to investigate the effect of distance from the probe on the extraction efficiency. First, a new particle distribution is defined in Figure 3.30, called Distribution B; this collection of particles remains a simplification of the real experimental conditions using a high intensity beam of ions, but it allows for more efficient simulations. Using SRIM, the final positions of 100 $^{139}Ba^{+}$ ions in LXe at 165 K and 1 atm are collected after propagating through a Be window of 7.62 μm thickness and a volume of LXe much larger than the stopping range of the ions. Distribution B is placed within Model A at various distances from the rounded, biased (-500 V) probe tip to determine the amount of time needed to collect all of the ions. This study is described in Figure 3.31. Since for every initial position, the ion extraction efficiency is always 100

%, it is more descriptive to plot this data in terms of the time required to reach 100 % efficiency.

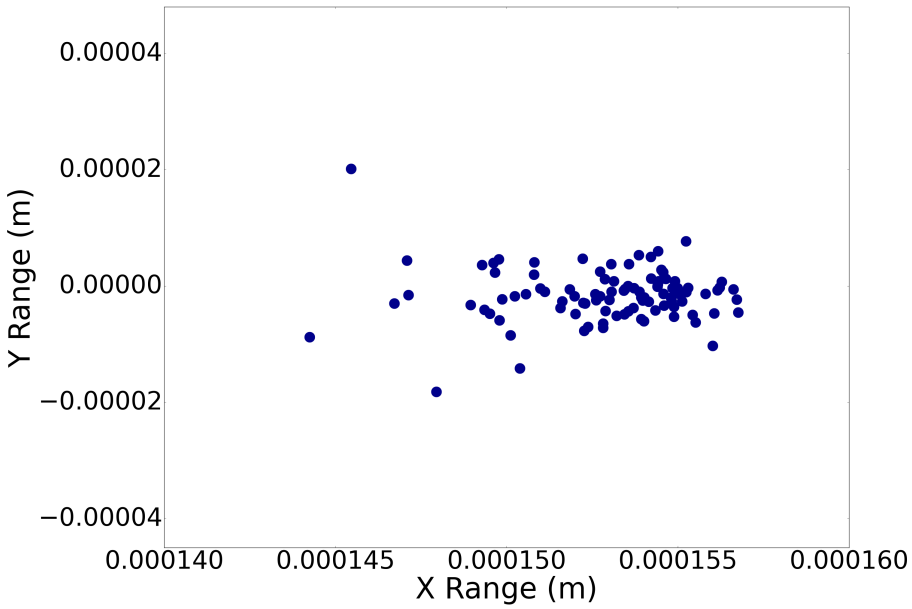

FIGURE 3.30: A particle distribution of 100 $^{139}Ba^{+}$ ions. The particle positions were simulated with TRIM, after allowing 100 $^{139}Ba^{+}$ ions to pass through a Be window of 7.62μm thickness and a volume of LXe at 165 K and 1 atm. The maximum stopping range is 0.156 mm into the LXe for a beam energy of 10 MeV/u.

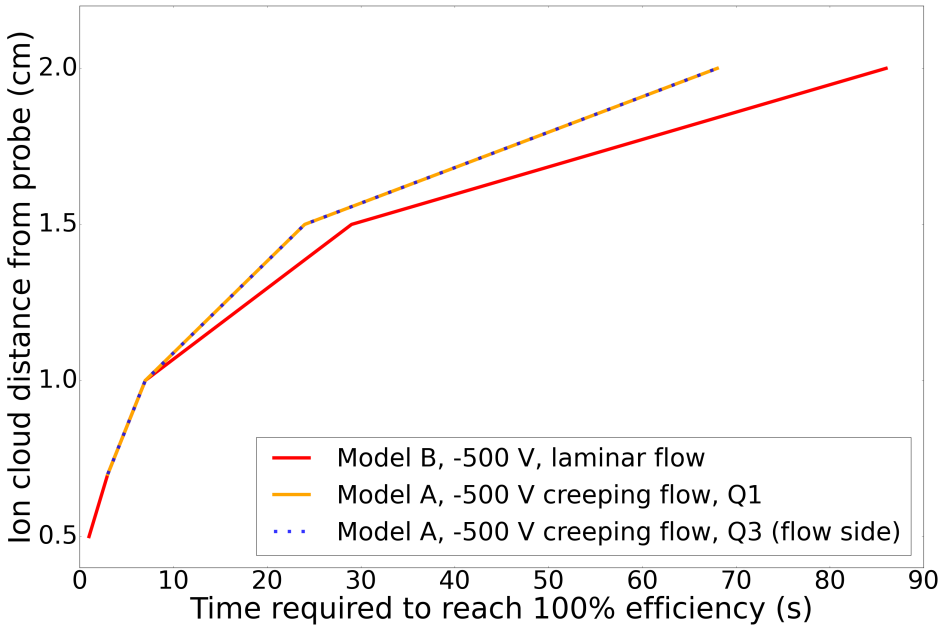

FIGURE 3.31: Ion cloud initial distances from probe as a function of time until all of the ions reach the probe boundary for 100 $^{139}Ba^{+}$ ions in LXe. The studies were performed using the Creeping Flow and Laminar Flow fluid models, and on both sides of the probe for Model A.

The same study is performed for Model B, with solving laminar flow, which is the less stiff solver for fluids compared to creeping flow, and very similar results are observed with slight discrepancies between the two fluid models at larger distances past 1.5 cm. Additionally, releasing the ions in Quadrant 1 gives the same results as Quadrant 3 in Model A, thus the fluid velocity field does not appear to change the efficiency. Perhaps the fluid velocity field would have implications on the extraction efficiency at larger distances, especially in a liquid medium; however, distances larger than 2 cm are not applicable to the experimental setup, since the beam will be implanted much closer than the maximum distance studied because of the nozzle.

Ultimately, if the ion mobility value used in these simulations deviates from the true value, the effects on the extracted efficiency can be calculated. Using Model B, for a LXe environment at 1 atm and 165 K, and a -500 V voltage applied to the probe tip, a particle distribution of $^{139}Ba^{+}$ as in Figure 3.30 is released from the position with coordinates (-2.5 cm, 0 cm, 0 cm). The time required to collect all 100 particles is recorded for a collection of ion diameter values, from 100 pm to 2500 pm, and the results are shown in Figure 3.32. Given an estimated ion mobility value of 2.11e-4 cm^2/Vs for $^{139}Ba^{+}$ in LXe [69], a 33.3 % increase or decrease in the corresponding ion diameter of 1579.45 pm would result in an ion collection time of ± 66 seconds. Ultimately, in the simulations, if the mobility value is "incorrect", then the same trends would be observed for any efficiency studies, only scaled up or down by a certain predictable factor.

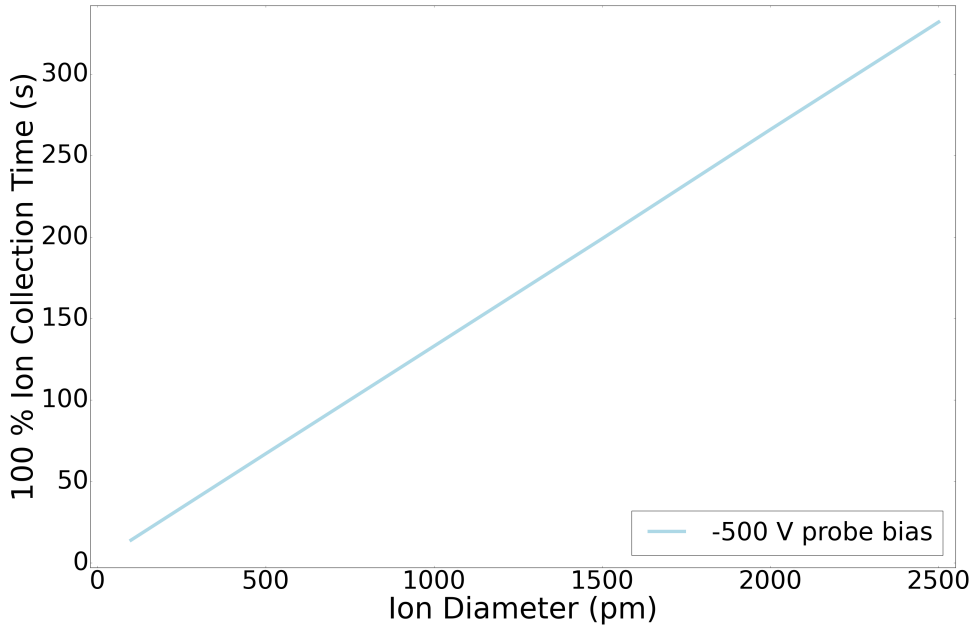

FIGURE 3.32: The collection time to achieve 100 % efficiency as a function of the ionic diameter. The data is collected from a simulation of 100 $^{139}Ba^{+}$ ions in LXe at 1 atm and 165 K starting 2.5 cm from the centre of the geometry.

3.4.5 Feasibility of Commissioning with Other Liquid and Gas Noble Mediums

For economical and commissioning purposes, the possibility of using gas and liquid mediums other than LXe is investigated. Due to availability, the use of gaseous argon (GAr) is appropriate for initial tests. Afterwards, the feasibility of using gaseous xenon (GXe) prior to employing LXe is investigated. Several parameter ramping simulations were performed to determine experimental settings for pressure and temperature of the GAr medium, as well as the probe bias.

In each of these different media, there are numerous simultaneously-changing parameters, ie., the media's dynamic viscosity, temperature, pressure, and the submerged ion's mobility. The ionic radius varies due to the clustering effect, which is how this changing ion mobility is incorporated into the simulation. The radius is calculated for each medium from ion mobility values from literature using Equation 3.28, and the values are summarized in Table 3.2.

Medium	Dynamic Viscosity η (Pas)	Temperature (K)	Ion Mobility (cm^2/Vs)	Particle Diameter (pm)
LXe	0.000510037	165	2.11e-4 [88]	1579.45
LAr	0.0026271	87	8.6e-4 [120]	752.34
GXe	0.000021118	273	~0.58 [121]	13.88
GAr	0.000021007	273	$\sim 2.32^2$	3.48
			1.80 [122]	4.49

TABLE 3.2: Ion mobility values from literature for singly charged $^{139}Ba^{1+}$ in various media, and the corresponding ionic radius for simulation purposes.

The ion mobility value for $^{139}Ba^{1+}$ in LAr is sourced from an EXO-200 experiment performing radon-polonium coincidence measurements to get $^{218}Po^{1+}$ in LAr, and assumptions to equate the ion mobilities of Ba and Po ions apply. It is commonly assumed for simulation purposes amongst collarborators that these two ions would exhibit similar behaviour in LXe. The ion mobility value for $^{139}Ba^{1+}$ in GXe is derived from a theory article using density functional theory and computational ion mobility theory to discuss the clustering and drift properties of Ba-ions (in GXe). By comparison of the mobility in LXe and LAr, the value in LAr is approximately a factor of 4 larger than that of LXe. As a benchmark, it is assumed that the same scaling applies between GXe and GAr, giving a mobility value of 2.32 cm^2/Vs in GAr. This value was used in the GAr simulations described in this section, however it is not a precise value[2].

More in-depth investigations of the ion mobility of $^{138}Ba^{1+}$ in GAr are described in a 1990's experimental article [122]. The effects of the ratio of the electrostatic field strength to the gas number density, E/n, are explored for the reduced mobility of $^{138}Ba^{1+}$, demonstrating the pressure and electric field dependence of the ion mobility. This relation is shown in Figure 3.33. The number density n of GAr at STP is found to be 2.69 $\times 10^{19}$ $1/m^3$ from $n = \frac{N_A}{M}\rho_m$, where N_A is Avogadro's constant, M is the molar mass of argon, and ρ_m is the mass density of argon. Given this value, to obtain an E/n value of 1 Td, 269 V is required to be applied on the probe tip. For a bias of -1000 V, the E/n value would be ~4 Td, which corresponds to a reduced mobility of ~1.80 cm^2/Vs. This mobility value remains valid for simulations unless there is a change in the electric field or the pressure of the gas by a factor of 100 or more.

[2]The ion mobility value for $^{139}Ba^{1+}$ in GAr is based on an assumption.

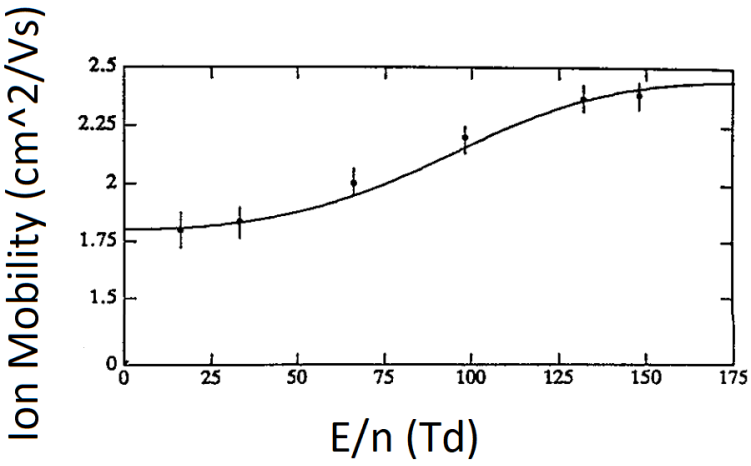

FIGURE 3.33: The reduced mobility of $^{138}Ba^{1+}$ ions drifting in Ar at 305 K, as a function of E/n. Adapted from [122] Figure 1.

The initial particle positions used in the COMSOL simulation were generated with SRIM. It was assumed that for a maximum available beam energy (10 MeV/u), one hundred $^{139}Ba^{1+}$ ions penetrated two layers of material: a thin beryllium window, and a volume of the medium in question that is much larger than the stopping range of the ions in this material.

Within Model B, this particle cloud was released from various positions from the biased probe tip, starting from 1 cm to 7 cm away from the probe. When using gaseous mediums, the beam particles that will penetrate the window will make it further into the gas than they would if it was liquid. Various initial positions were taken to evaluate the optimal position of a nozzle to be placed at the beam window extending inside the copper cylinder. These simulations serve as an indirect study to the ideal location of this nozzle, depending on the medium in the vessel.

The electric field generated by the biased probe tip in Model B is shown in Figure 3.34. In this example, -2000 V is applied to the surface of the probe tip. Once the ions are released in this environment, their trajectories while travelling in GAr are demonstrated in Figure 3.42.

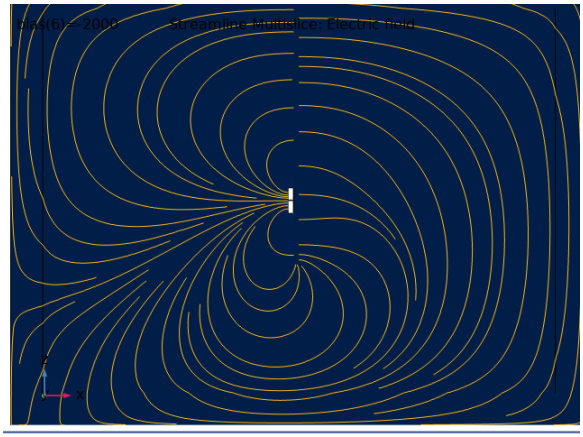

FIGURE 3.34: The electric field (V/m) of Model B where the substrate of the probe is biased to -2000 V. The field lines are shown in yellow, converging onto the substrate. Ions are injected on the left side of the vessel.

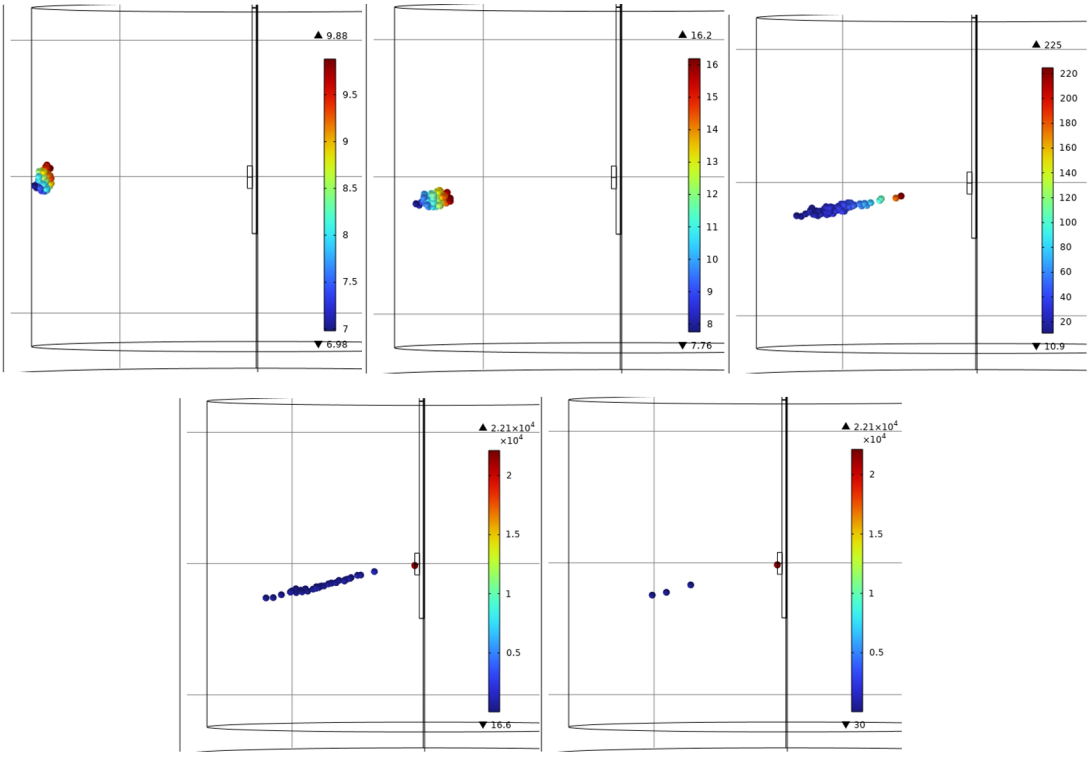

FIGURE 3.35: The trajectories of 100 Ba ions submerged in GAr, as they travel to the probe tip from the edge of the copper vessel 7 cm away (x-direction). The frames shown are read from left to right from the top row, and the bottom row. The coloured scale represents the ion velocities (cm/s), and the frames take place over the course of 30 s.

In the case where a lower beam energy is used, the particles do not travel as far into the gas. Nonetheless, simulations suggest that they will always arrive to the probe, it is a matter of time. Since we wish to reduce the collection time where possible to allow for more experimental runs, the amount of time taken to achieve 100% efficiency is of importance. It may also matter depending on the half-life of the studied species. The ion cloud initial distances from the probe tip are varied for several probe bias values, using GAr, GXe, and LAr in Figures 3.36, 3.37, and 3.38 respectively. For reference, in Figure 3.42 shows the ions beginning their journey 7 cm away from the probe (an initial position of 7cm for the whole ion cloud). The results from Figure 3.36 are summarized in Table 3.3.

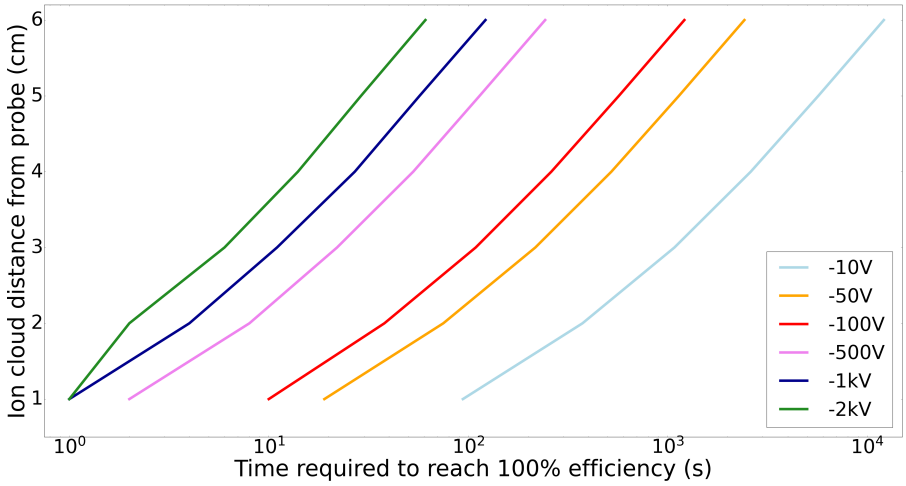

FIGURE 3.36: Ion cloud distance vs. time for various probe biases in GAr at 1 atm, 273 K.

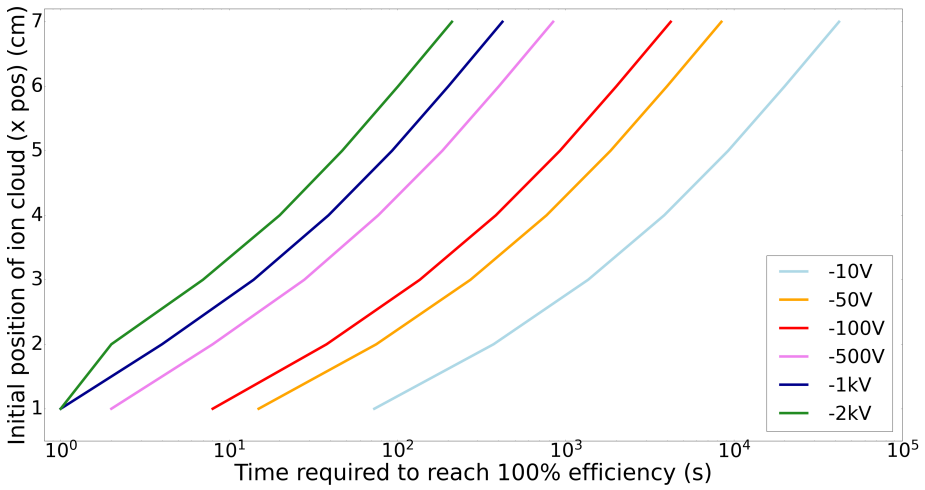

FIGURE 3.37: Ion cloud distance vs. time for various probe biases in GXe at 1 atm, 273 K.

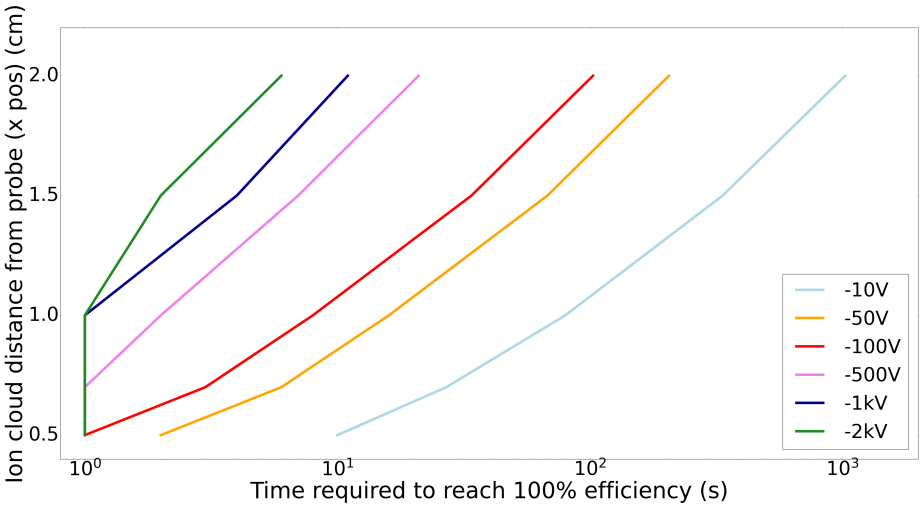

FIGURE 3.38: Ion cloud distance vs. time for various probe biases in LAr at 1 atm, 87 K.

Initial Ion Cloud Distance from Probe (cm)	Time to Reach Probe for Various Biases (s)					
	-10 V	-50 V	-100 V	-500 V	-1000 V	-2000 V
1	94	19	10	2	1	1
2	374	75	38	8	4	2
3	1081	217	109	22	11	6
4	2609	522	261	53	27	14
5	5689	1138	569	114	57	29
6	12120	2424	1212	243	122	61

TABLE 3.3: Results for Ba ion simulations in GAr at 1 atm and 273 K, as shown in Figure 3.36. The time required for all ions to be collected on the probe tip is shown for various biases, for a range of ion starting distances from the probe tip.

The ion travel time increases exponentially when the distance between the ion cloud and the probe increases. In GAr, for a reasonable experimental probe bias setting of -500 V, the ion travel time to the probe spans a range from 1 s (at 1 cm from the probe), to 243 s (starting at 6 cm from the probe). Depending on the beam energy used, the stopping range for $^{139}Ba^{1+}$ in GAr at 1 atm and 273 K falls within the probe distances explored in these simulations. As introduced in Figure 2.12, a beam energy of 0.72 MeV/u would deposit $^{139}Cs^{1+}$ ions 5 cm away from the probe tip, and higher beam energies of 3.6 MeV/u would bring the ions within millimetres from the probe tip. The effect of the probe bias magnitude on the ion travel time increases with the ion cloud distance; for instance, when comparing the two extreme scenarios of applying -10 V and -2000 V to the probe, the difference in the ion travel times is 93 s for 1 cm, but it increases to 12059 s (∼3.3 h) for a distance of 6 cm. This effect would result in practicality concerns during experimental runs, favouring high voltages applied to the probe only if necessary in cases where beam energies are expected to be low. The same trends are observed in all of the simulated media.

Krypton would also suffice in the initial phases of the experiment. However, the precise ion mobility value of Ba in gaseous krypton (GKr) is experimentally unknown and as of current times, there is no reliable value from literature; the value lies between that of GXe and GAr. For this reason, simulations involving GKr would only lead to estimations in the time required to reach 100 % extraction efficiency. The experimental apparatus would be able to keep krypton in the required temperature ranges for these studies, as the melting point is 116 K for GKr [100].

3.4.6 Modifications to Beam Entrance Window

Since the initial distance of the implanted ions is a critical parameter in the process of ion extraction, methods to control it other than varying the beam energy are explored. One possibility is the addition of a nozzle extending inside the LXe volume, bringing the implanted ions closer to the probe tip. This subsection summarizes the effects of these modifications to the simulation geometry.

The electric potential of the setup and the fluid velocity field of the LXe are shown in Figure 3.39 when the nozzle is placed 1 cm away from the probe tip. This simulation geometry will be referred to as Model C. The nozzle is defined as a hollow, stainless steel object with a thin Be sheet on the circular face in the simulation. It has no visible effect on the electric field produced by the biased probe tip. However, the fluid velocity field does differ when compared to Model B. As demonstrated in Figure 3.39, there is almost no flow field at the region of LXe between the nozzle and the probe tip (region in blue). However, the lack of fluid field does not seem to affect the ion extraction efficiency.

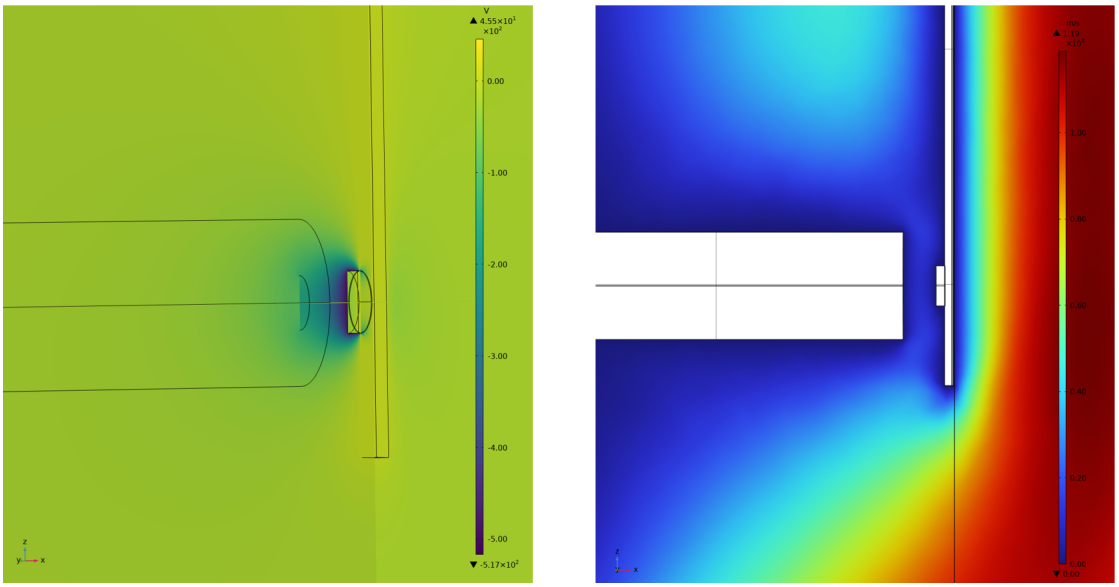

FIGURE 3.39: Left: The electric potential (V) of the model, with -500 V applied to the probe tip substrate. Right: The fluid velocity of the LXe medium at 1 atm and 165 K.

More complexities are also included with regards to the ion distribution used in these simulations, now containing 15,000 particles instead of 100 as in Distribution B. This new set of particles, named Distribution C, was also generated by SRIM, after passing Ba ions through a Be layer of 7.62 μm in thickness, and an adjacent volume of LXe. Distribution C is depicted in Figure 3.40, and these ions are placed 0.15 mm from the nozzle on the x axis (assuming a maximum ion beam energy in LXe).

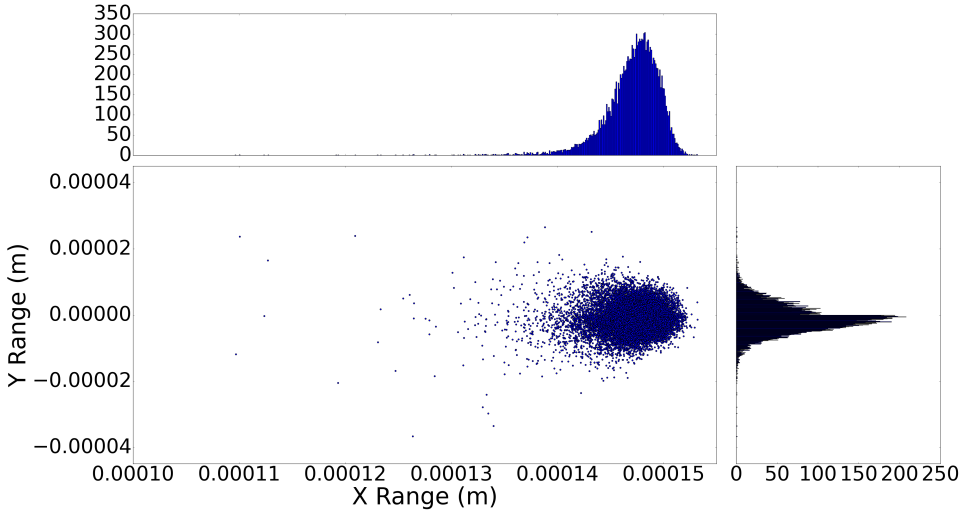

FIGURE 3.40: Distribution C consists of 15,000 particles, and their positions shown are calculated by Monte-Carlo SRIM simulations of Ba ions travelling through a Be (window) and LXe layer. For a given beam energy of 10 MeV/u, the ions come to a stop around 0.15 mm, shown on the x-axis.

The particles arrive in 15 s from 1 cm away, thus no new behaviour is found compared to previous simulations. It is interesting, however, that the ions all arrive at a localized point on the probe tip, seen in Figure 3.41, even with such a large particle distribution.

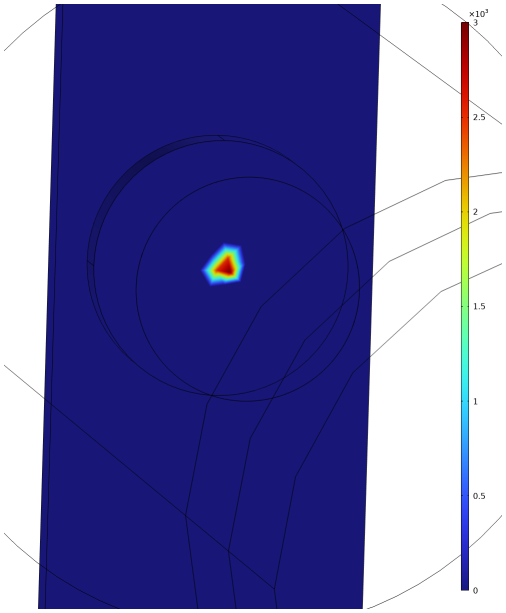

FIGURE 3.41: The final locations of the Ba ions on the probe tip, where red corresponds to a higher concentration of particles and blue represents no particles detected.

The same distribution type was also created with SRIM, but exchanging LXe with GAr. The same maximum beam energy was used (despite the stopping range being greater than the distance from the edge of the vessel to the probe) in order to maintain the most extreme cases of ion straggle (deviations from the y-axis). For lower beam energies, the implanted ions into gas media would not spread out as much as for higher beam energies; the limits of the ions' straggle behaviour is accounted for. When importing this particle data set into COMSOL, the initial position is manually configured to the edge of the vessel, as shown in Figure 3.42. Most of the particles successfully reach the probe tip in less than 5 s with -500 V applied to the probe. From these simulations, it is evident that for gas media there is no requirement for a nozzle or extension of the beam window, even for the lowest possible beam energy setting available.

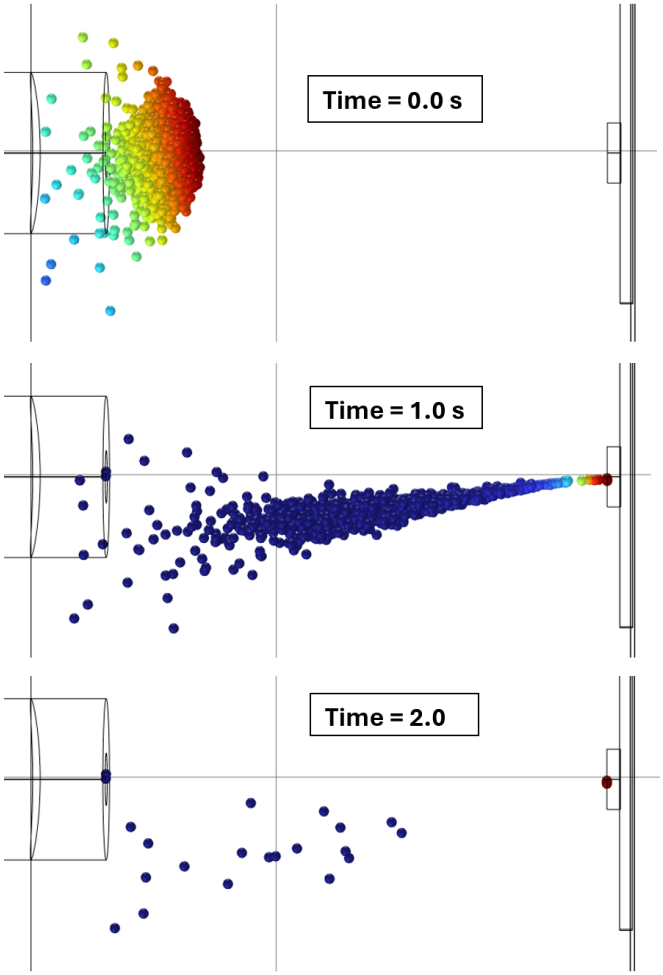

FIGURE 3.42: The simulated trajectories of 15,000 $^{139}Ba^{1+}$ ions in GAr at 1 atm and 273 K. The vast majority of the ions reach the probe in about 5 s.

Chapter 4

Discussion

COMSOL simulations were performed to investigate Ba ion motion in LXe, LAr, GXe, and GAr under different experimental conditions. The ion diameter, distance from probe tip, probe tip bias, and the pressure, temperature, and viscosity of the medium of interest were varied to study systematic effects and possible ion loss mechanisms on the ion extraction efficiency.

The ion diameter is inversely proportional to the ion mobility in a given medium and it is used to set the ion mobility, the most critical parameter in the COMSOL simulation. In LXe, the ion extraction efficiency decreases exponentially as the distance of the ions' position from the probe tip increases (for given medium and probe bias settings). Optimal voltages to attract the particles at certain distances from the probe are also explored, as a method to combat particle loss and drift the ions in the shortest, most practical amount of time.

The feasibility of using noble gases and liquids (other than LXe) is explored to allow successful commissioning of the apparatus and to understand systematics related to the experimental setup and conditions. It appears that GAr is a good candidate medium for a phased approach in commissioning the experimental setup. With the simulations discussed, a clearer understanding of the conditions and Ba ion behaviour is cultivated prior to making a precise measurement of extraction efficiencies. Performing the simulations with multiple media plays a role in bench marking, as experimental data for various media and conditions can determine if the simulation is capable of making accurate predictions.

Additionally, the effects of small thermal currents on the ion extraction efficiency in LXe are investigated. By introducing a fluid velocity field in the simulated LXe, it is found that the ion extraction efficiency is unaffected for certain proximities to the probe tip, but it entirely depends on the magnitude of the thermal current. This finding emphasizes the importance of maintaining a constant temperature and pressure within the LXe vessel during the experiment, as well as implanting the ions as close as possible to the probe tip.

This work is crucial to determine the optimum experimental configuration and conditions prior to the experiment, and to ultimately determine the extraction efficiency of Ba ions

from LXe in a controlled environment. Once insights are made towards this goal, this technique may be incorporated into the wider scheme for Ba-tagging, and eventually the nEXO detector.

4.1 Future Outlook

Now that a realistic simulation has been constructed specifically for the planned radioactive beam experiments at TRIUMF, the simulations can be advanced to include functionalities involving more ions. Particularly, the initial ion distributions can be released more than once, at a time interval corresponding to a certain beam intensity (within the computational memory limits). In addition, it may be possible to study how many layers of Ba ions can accumulate onto the probe tip surface to determine if any modifications are required to the probe bias during operation.

There is also a possibility for the need to incorporate particle-particle interactions in the simulation, but this depends on the beam intensity for the exact isotope in use. Particle-particle interactions of the implanted ions are neglected in the current simulations because the space charge effects are negligible for the number of Ba ions used; these effects may become important if the space charge density of the implanted ions becomes ~ 1 million charges/cm^3.

Once the setup has been commissioned with Ba and extraction of Ba from LXe has been demonstrated successfully, the next step would be to implant pure ^{139}Cs beam and allow it to decay to mimic a $\beta\beta$ decay and extract the decay daughter ^{139}Ba. This scenario would more closely resemble the potential $0\nu\beta\beta$ decay in ^{136}Xe for nEXO, since the decay daughter ^{136}Ba is produced within the LXe volume if extracted and identified with the electrostatic probe. Also, implanting different beam isotopes with different half lives opens up the potential to study systematic effects based on decay rate.

Depending on the initial commissioning results, it may also be worth investigating the effects of adding field shaping rings within the copper cell; this may allow the beam particles to be deposited into LXe without a beam port nozzle if the electric field is guiding the ions from the edge of the vessel. In addition, a set of quadrupoles on the beamline has the potential to unintentionally expose the apparatus to a magnetic field; this field could be added to the simulation to minimize ion losses.

In subsequent steps of the experiment, it will be tested to move the probe into the LXe cell after ions were implanted into the medium. This scenario could be simulated with COMSOL as well, and it would more closely resemble the capillary ion extraction technique.

The third and final experimental phase involves the implementation of silicon photomultipliers (SiPM). SiPMs have been chosen as the devices to detect the vacuum ultraviolet (VUV) scintillation light for nEXO. SiPMs are silicon devices with single photon sensitivity, and are approximately 1 cm^2 in size; they have a quantum efficiency of about 15% at 175 nm– the wavelength of the ^{136}Xe scintillation light.

The LXe volume, instrumented with SiPMs, will be connected to the beamline. Longer-lived Cs isotopes will be implanted into the LXe cell, without any electrostatic probe initially present. The radioactive decays of the implanted Cs will be detected by the SiPMs, and the daughter ions of the Cs-decays will be extracted with a probe. The daughter Ba atom or ion will be identified using laser spectroscopy either in ice or in vacuum. At first, this will be done with multiple decays, and eventually with only a single Cs decay. Eventually, the goal is to achieve single Ba ion capture with the electroprobe– not only clusters of barium ions as simulated.

Appendix A

Saturation and Decay Chain Plots

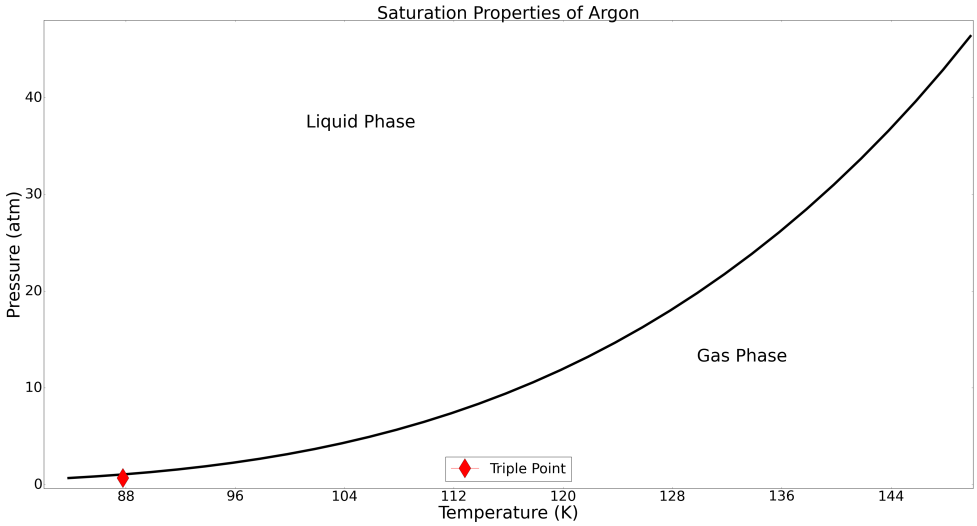

FIGURE A1.1: The saturation curve for Ar. The red diamond denotes the triple point.

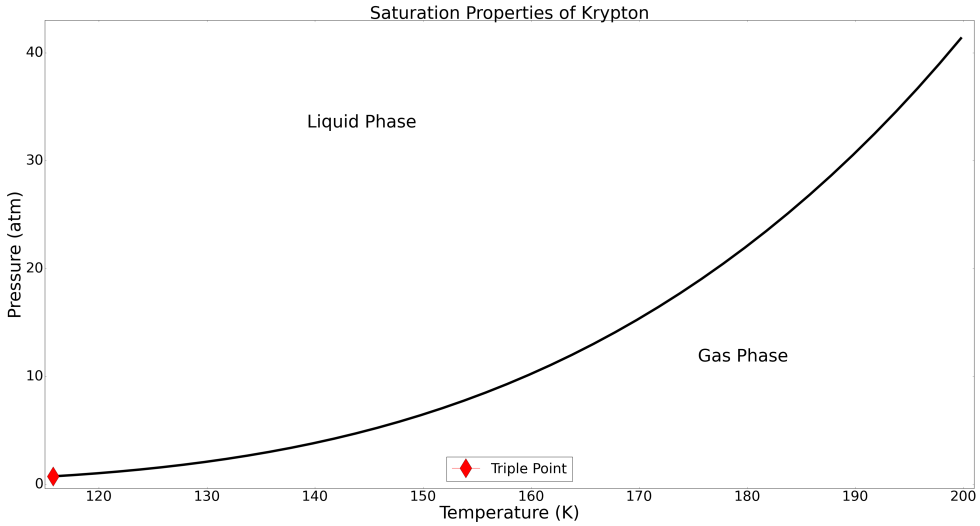

FIGURE A1.2: The saturation curve for Ar. The red diamond denotes the triple point.

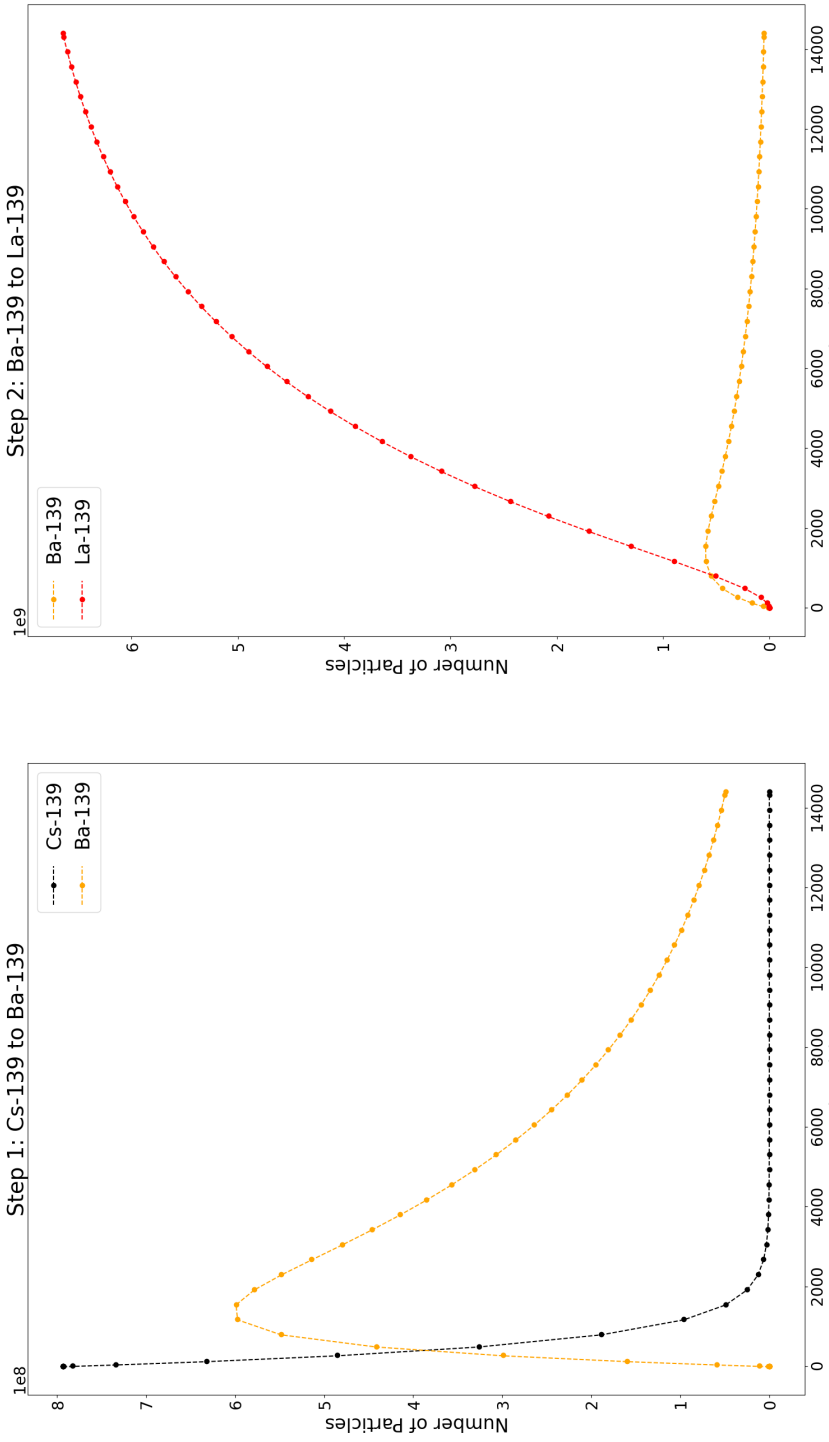

FIGURE A1.3: The decay series for ^{139}Cs after 4 hours of elapsed time. The first decay product is radioactive ^{139}Ba, and then stable ^{139}La.

Appendix B

Beam Delivery of ^{139}Cs and ^{139}Ba

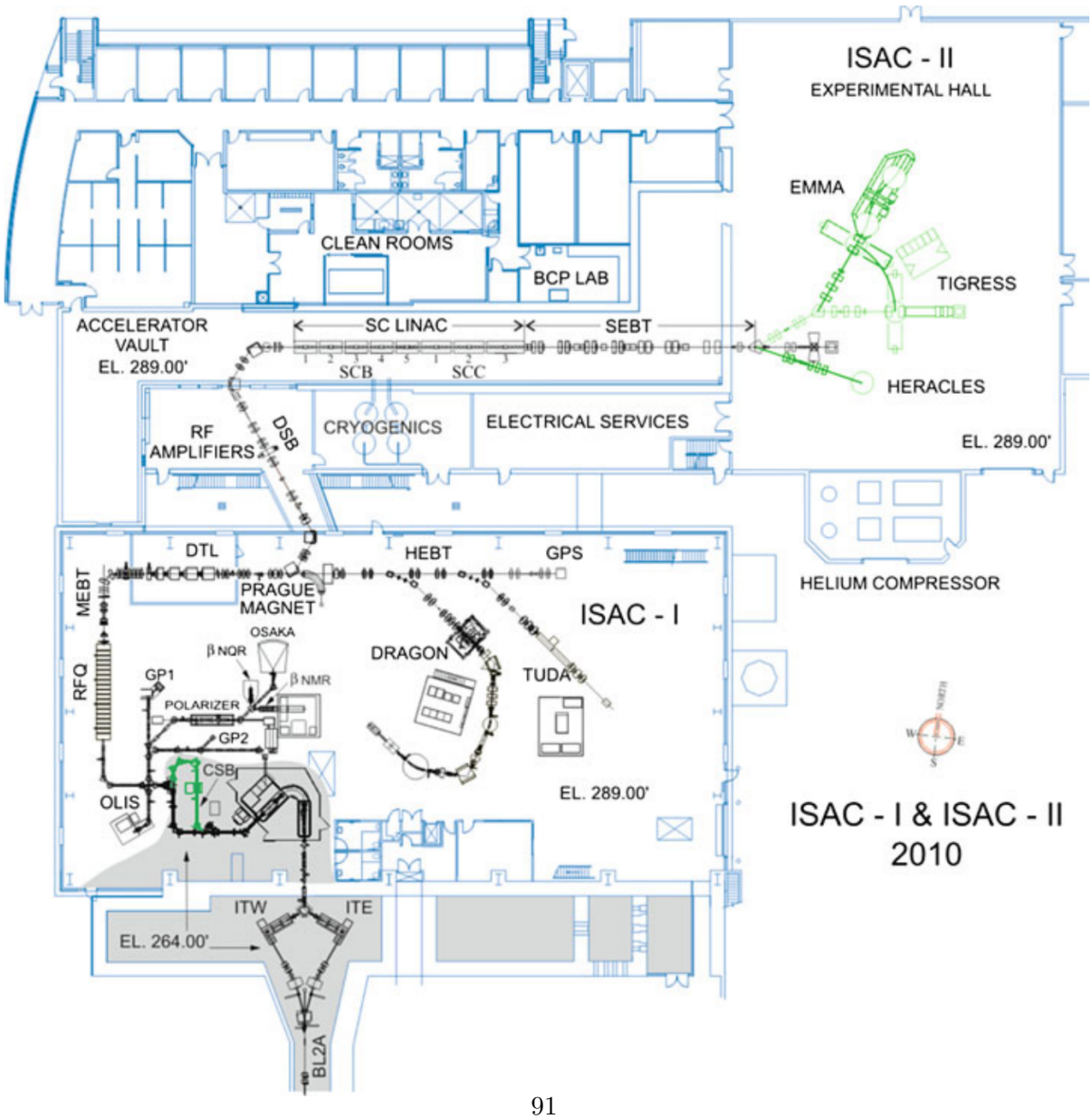

FIGURE A2.1: Beamline and accelerator network for the ISAC experimental halls [93].

Realistically, after consultation with the Beam Delivery Group at TRIUMF, the beam composition will be 1:1 ^{139}Cs and ^{139}Ba. This would not hinder the capability of demonstrating electrostatic ion extraction with a probe. The half lives and available yields of these isotopes are summarized in Table 2.2. Cs beams have been demonstrated in the past to be deliverable at adequate intensities using a UC_x target. The total transmission efficiency of the target is on the order of 10^{-4}. Higher efficiencies would be possible once CANREB becomes available for later phases of the experiment by skipping directly to the 32^+ charge state. If a very high charge state is used, such as 45^+, and closed shell breeding, additional background reduction will be possible. This possibility requires EBIS operation at full electron beam power, and improved vacuum conditions around the RFQ. In Phase 1 and 2, the isobaric contaminants are not a concern because they have unique γ spectra. For Phase 3, the contaminants become of importance because daughters of single Cs decays will be studied, and a high Ba contamination in the Cs beam may create an unwanted background. Further beam development to reduce this contaminant will be crucial.

The required beam current is estimated using ^{139}Cs as an example. A signal-to-background ratio of 30 was attained at an initial minimum count rate of $R_0 = 3$ counts/s for ^{139}Ba 166 keV line in the γ spectrum using a past setup test. With a conservative 1% Ge detector efficiency for the 166 keV line, the initial Ba activity on the probe is given by:

$$A_0 = \frac{R_0}{\epsilon_{Tot}} = 300 \text{ Bq}. \tag{B.1}$$

After about 30 minutes, a sample of ^{139}Cs would undergo three half-lives resulting in 87.5 % of the initial Cs decaying into Ba. This amount of time is sufficient for populating the sample with adequate quantities of Ba, which suggests that the minimum number of Cs ions to be implanted in the volume should be $3 \cdot 10^6$ ions. With a beam exposure time from 5 to 10 minutes, the minimum ion current required is approximately

$$I_{beam} = (4.5 - 9) \cdot 10^3 \ ^{139}\text{Cs ions/s}. \tag{B.2}$$

The estimated beam intensity is below the currently available ^{139}Cs beam at TRIUMF, outlined in Table 2.2. After considering the transmission efficiency, however, this intensity may decrease to approximately 10^4 or 10^5 pps, depending on the isotope species.

Appendix C

Extraction Efficiency Plot

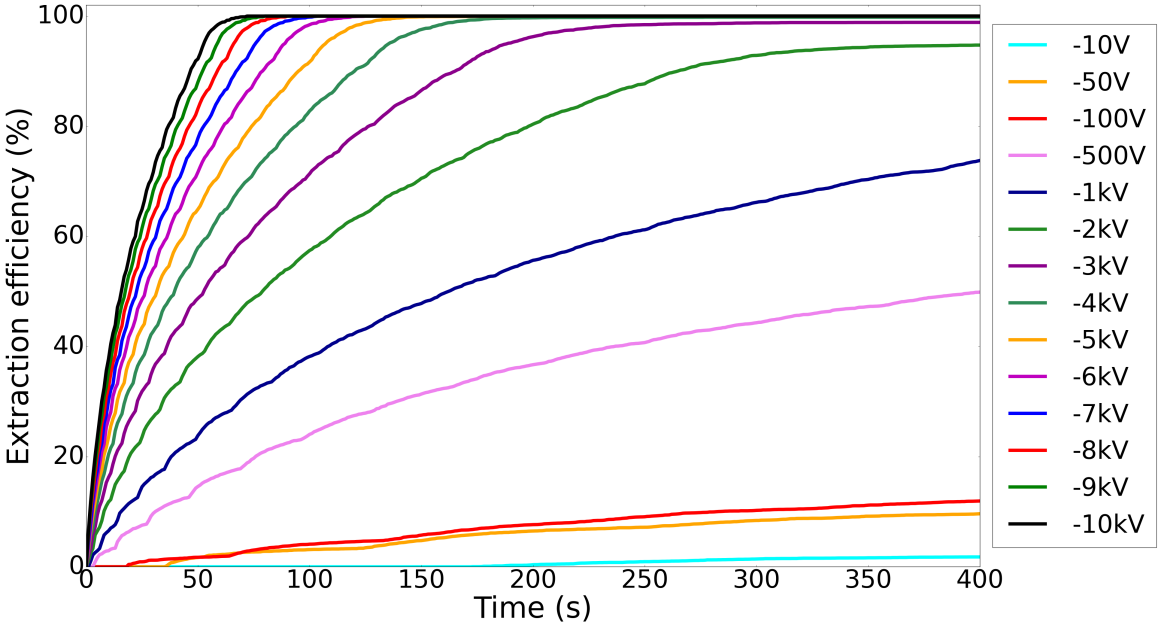

FIGURE A3.1: The extraction efficiency of Ba in LXe as a function of time for various probe bias settings using Model A and Distribution A.

Bibliography

[1] W. Buchmüller, R. Peccei, and T. Yanagida. Leptogenesis as the Origin of Matter. *Annual Review of Nuclear and Particle Science* 55(1) (Dec. 2005), 311–355. ISSN: 1545-4134.

[2] C. Kato, K. Ishidoshiro, and T. Yoshida. Theoretical Prediction of Presupernova Neutrinos and Their Detection. *Annual Review of Nuclear and Particle Science* 70(1) (Oct. 2020), 121–145. ISSN: 1545-4134.

[3] B. Müller. Neutrino Emission as Diagnostics of Core-Collapse Supernovae. *Annual Review of Nuclear and Particle Science* 69(1) (Oct. 2019), 253–278. ISSN: 1545-4134.

[4] Q. R. Ahmad et al. Measurement of the Rate of $\nu_e + d \rightarrow p + p + e^-$ Interactions Produced by ^8B Solar Neutrinos at the Sudbury Neutrino Observatory. *Phys. Rev. Lett.* 87 (7 July 2001), 071301.

[5] Q. R. Ahmad et al. Direct Evidence for Neutrino Flavor Transformation from Neutral-Current Interactions in the Sudbury Neutrino Observatory. *Phys. Rev. Lett.* 89 (1 June 2002), 011301.

[6] Y. Fukuda et al. Evidence for Oscillation of Atmospheric Neutrinos. *Physical Review Letters* 81(8) (Aug. 1998), 1562–1567. ISSN: 1079-7114.

[7] D. Griffiths. *Introduction to Elementary Particles*. 2nd. New York, USA: John Wiley Sons, 2008.

[8] J. R. Gustafson. *Wolfgang Pauli 1900 to 1930: His Early Physics in Jungian Perspective*. 2010.

[9] F. L. Wilson. Fermi's Theory of Beta Decay. *Am. J. Phys.* 36(12) (1968), 1150–1160.

[10] C. L. Cowan et al. Detection of the free neutrino: A Confirmation. *Science* 124 (1956), 103–104.

[11] G. Danby et al. Observation of High-Energy Neutrino Reactions and the Existence of Two Kinds of Neutrinos. *Phys. Rev. Lett.* 9 (1962), 36–44.

[12] M. L. Perl et al. Evidence for Anomalous Lepton Production in e+ - e- Annihilation. *Phys. Rev. Lett.* 35 (1975), 1489–1492.

[13] K. Kodama et al. Observation of tau neutrino interactions. *Physics Letters B* 504(3) (Apr. 2001), 218–224. ISSN: 0370-2693.

[14] R. Davis Jr., D. S. Harmer, and K. C. Hoffman. Search for neutrinos from the sun. *Phys. Rev. Lett.* 20 (1968), 1205–1209.

[15] J. N. Bahcall and R. Davis. Solar Neutrinos: A Scientific Puzzle. *Science* 191(4224) (1976), 264–267. ISSN: 00368075, 10959203.

[16] M. C. Gonzalez-Garcia and Y. Nir. Neutrino masses and mixing: evidence and implications. *Reviews of Modern Physics* 75(2) (Mar. 2003), 345–402. ISSN: 1539-0756.

[17] Z. Maki, M. Nakagawa, and S. Sakata. Remarks on the unified model of elementary particles. *Prog. Theor. Phys.* 28 (1962), 870–880.

[18] J. Bernabeu. On the history of the PMNS Matrix ...with today's perspective. *Il Nuovo Cimento C* 37(3) (July 2014), 145–154. ISSN: 03905551, 03905551.

[19] G. Drexlin and K. Collaboration. KATRIN-direct measurement of a sub-eV neutrino mass. *Nuclear Physics B-Proceedings Supplements* 145 (2005).

[20] V. Barger, D. Marfatia, and K. Whisnant. *The physics of neutrinos*. Princeton University Press, 2012.

[21] T. Araki et al. Measurement of neutrino oscillation with KamLAND: Evidence of spectral distortion. *Phys. Rev. Lett.* 94 (2005), 081801.

[22] S. Westerdale. Neutrino Mass Problem: Masses and Oscillations. *MIT Department of Physics* (2010).

[23] P. D. Group. 2014 Review of Particle Physics (2014).

[24] K. Nakamura and P. D. Group. Review of Particle Physics. *Journal of Physics G: Nuclear and Particle Physics* (2010).

[25] R. N. Cahn et al. *White Paper: Measuring the Neutrino Mass Hierarchy*. 2013.

[26] P. de Salas et al. Status of neutrino oscillations 2018: 3 hint for normal mass ordering and improved CP sensitivity. *Physics Letters B* 782 (July 2018), 633–640. ISSN: 0370-2693.

[27] M. J. Dolinski, A. W. Poon, and W. Rodejohann. Neutrinoless Double-Beta Decay: Status and Prospects. *Annual Review of Nuclear and Particle Science* 69(1) (Oct. 2019), 219–251. ISSN: 1545-4134.

[28] S. F. King. Neutrino mass models: A road map. *Journal of Physics: Conference Series* 136(2) (Nov. 2008), 022038. ISSN: 1742-6596.

[29] F. T. Avignone, S. R. Elliott, and J. Engel. Double beta decay, Majorana neutrinos, and neutrino mass. *Reviews of Modern Physics* 80(2) (Apr. 2008), 481–516. ISSN: 1539-0756.

[30] M. Medina Peregrina. *Development of an in-Xe-gas Laser Ablation Source for the Ba-tagging technique for nEXO*. Master's Thesis, McGill University, 2020.

[31] M. Goeppart-Mayer. Double Beta-Disintegration. *Physical Review* 48 (1935), 512–516. ISSN: 1539-0756.

[32] A. S. Barabash. Experiment double beta decay: Historical review of 75 years of research. *Physics of Atomic Nuclei* 74(4) (Apr. 2011), 603–613. ISSN: 1562-692X.

[33] R. Arnold et al. Measurement of the double-beta decay half-life and search for the neutrinoless double-beta decay of ^{48}Ca with the NEMO-3 detector. *Physical Review D* 93(11) (June 2016). ISSN: 2470-0029.

[34] C. Alduino et al. Measurement of the two-neutrino double-beta decay half-life of Te-130 with the CUORE-0 experiment. *The European Physical Journal C* 77(1) (Jan. 2017).

[35] Observation of two-neutrino double electron capture in ^{124}Xe with XENON1T. *Nature* 568(7753) (Apr. 2019), 532–535. ISSN: 1476-4687.

[36] C. Patrignani et al. Review of Particle Physics. *Chinese Physics C* 40(10) (2016).

[37] N. Aghanim et al. Planck2018 results: VI. Cosmological parameters. *Astronomy amp; Astrophysics* 641 (Sept. 2020), A6. ISSN: 1432-0746.

[38] M. Agostini et al. Final Results of GERDA on the Search for Neutrinoless Double-β Decay. *Phys. Rev. Lett.* 125(25) (2020), 252502.

[39] D. Q. Adams et al. Search for Majorana neutrinos exploiting millikelvin cryogenics with CUORE. *Nature* 604(7904) (Apr. 2022), 53–58. ISSN: 1476-4687.

[40] S. Abe et al. Search for the Majorana Nature of Neutrinos in the Inverted Mass Ordering Region with KamLAND-Zen. *Physical Review Letters* 130(5) (Jan. 2023). ISSN: 1079-7114.

[41] I. Ogawa et al. Search for neutrino-less double beta decay of Ca-48 by CaF-2 scintillator. *Nucl. Phys.* A730 (2004), 215–223.

[42] I. J. Arnquist et al. Final Result of the Majorana Demonstrator's Search for Neutrinoless Double- Decay in Ge-76. *Physical Review Letters* 130(6) (Feb. 2023). ISSN: 1079-7114.

[43] R. Arnold et al. First Results of the Search for Neutrinoless Double-Beta Decay with the NEMO 3 Detector. *Physical Review Letters* 95(18) (Oct. 2005). ISSN: 1079-7114.

[44] O. Azzolini et al. Final Result on the Neutrinoless Double Beta Decay of Se-82 with CUPID-0. *Physical Review Letters* 129(11) (Sept. 2022). ISSN: 1079-7114.

[45] F. Danevich et al. Double decay of 116Cd. Final results of the Solotvina experiment and CAMEO project. *Nuclear Physics B-proceedings Supplements - NUCL PHYS B-PROC SUPPL* 138 (Jan. 2005), 230–232.

[46] New Direct Limit on Neutrinoless Double Beta Decay Half-Life of Te128 with CUORE. *Physical Review Letters* 129(22) (2022).

[47] D. Q. Adams et al. Search for Majorana neutrinos exploiting millikelvin cryogenics with CUORE. *Nature* 604(7904) (Apr. 2022), 53–58. ISSN: 1476-4687.

[48] G. Anton et al. Search for Neutrinoless Double-β Decay with the Complete EXO-200 Dataset. *Phys. Rev. Lett.* 123 (16 Oct. 2019), 161802.

[49] S. Abe et al. Search for the Majorana Nature of Neutrinos in the Inverted Mass Ordering Region with KamLAND-Zen. *Physical Review Letters* 130(5) (Jan. 2023). ISSN: 1079-7114.

[50] J. Argyriades et al. Measurement of the double beta decay half-life of 150-Nd and search for neutrinoless decay modes with the NEMO-3 detector. *Physical Review C* 80(3) (2009). ISSN: 1089-490X.

[51] K. Zuber. *Neutrino Physics*. CRC Press, 2020.

[52] J. Kotila and F. Iachello. Phase-space factors for double decay. *Physical Review C* 85(3) (Mar. 2012). ISSN: 1089-490X.

[53] P. Vogel. Nuclear structure and double beta decay. *Journal of Physics G: Nuclear and Particle Physics* 39(12) (Nov. 2012), 124002. ISSN: 1361-6471.

[54] B. Martin. *Nuclear and particle physics: an introduction*. John Wiley Sons, 2006.

[55] O. Cremonesi. Neutrinoless Double Beta Decay: Present and Future. *Nuclear Physics B - Proceedings Supplements* 118 (2003), 287–296.

[56] A. Garfagnini. Neutrinoless double beta decay experiments. *International Journal of Modern Physics: Conference Series* 31 (Jan. 2014), 1460286. ISSN: 2010-1945.

[57] https://www.nist.gov/pml/xcom-photon-cross-sections-database, visited 11/2023.

[58] K. Fujii et al. High-accuracy measurement of the emission spectrum of liquid xenon in the vacuum ultraviolet region. *Nuclear Instruments and Methods in Physics Research Section A: Accelerators, Spectrometers, Detectors and Associated Equipment* 795 (2015), 293–297. ISSN: 0168-9002.

[59] J. Albert et al. Improved measurement of the 2 half-life of 136-Xe with the EXO-200 detector. *Physical Review C* 89 (Jan. 2014).

[60] N. Ackerman and e. al et. Observation of two-neutrino double-beta decay in Xe-136 with the EXO-200 detector. *Physical Review Letters* 107(21) (2011), 212501.

[61] nEXO Collaboration et al. *nEXO Pre-Conceptual Design Report*. 2018.

[62] M. Redshaw et al. Mass and Double-BetaDecay Q-Value of Xe-136. *Physical Review Letters* 98(5) (2007).

[63] E. Aprile and T. Doke. Liquid xenon detectors for particle physics and astrophysics. *Reviews of Modern Physics* 82(3) (2010).

[64] R. Ford. SNOLab: Review of the facility and experiments. *AIP Conference Proceedings* 1441 (2012).

[65] S. A. Kharusi. Neutrinoless double-β decay with nEXO. *SNOLAB User's Meeting, Oral Presentation* (2021).

[66] J. B. Albert et al. Sensitivity and discovery potential of the proposed nEXO experiment to neutrinoless double- decay. *Physical Review C* 97(6) (June 2018). ISSN: 2469-9993.

[67] G. Adhikari et al. nEXO: neutrinoless double beta decay search beyond 1028 year half-life sensitivity. *Journal of Physics G: Nuclear and Particle Physics* 49(1) (Dec. 2021), 015104. ISSN: 1361-6471.

[68] M. Moe. Detection of neutrinoless double-beta decay. *Physical Review C* 44(3) (1991), 931.

[69] J. B. Albert et al. Measurements of the ion fraction and mobility of - and -decay products in liquid xenon using the EXO-200 detector. *Physical Review C* 92(4) (Oct. 2015). ISSN: 1089-490X.

[70] M. Green et al. Observation of single collisionally cooled trapped ions in a buffer gas. *Physical Review A* 76(2) (Aug. 2007). ISSN: 1094-1622.

[71] C. Chambers et al. *Imaging individual barium atoms in solid xenon for barium tagging in nEXO*. 2018.

[72] A. D. McDonald et al. Demonstration of Single-Barium-Ion Sensitivity for Neutrinoless Double-Beta Decay Using Single-Molecule Fluorescence Imaging. *Physical Review Letters* 120(13) (Mar. 2018). ISSN: 1079-7114.

[73] W. Neuhauser et al. Localized visible $Ba^{+} mono-ionoscillator$. *Physical Review A* 22(3) (1980), 1137.

[74] D. Ray et al. Ba-tagging for a nEXO upgrade and future 0 experiments: The Canadian approach. *Atom* (In preparation).

[75] H. Rasiwala et al. 'Searching for a needle in a haystack;' A Ba-tagging approach for an upgraded nEXO experiment. *Nuclear Instruments and Methods in Physics Research Section B: Beam Interactions with Materials and Atoms* 541 (2023), 298–300. ISSN: 0168-583X.

[76] T. Brunner et al. An RF-only ion-funnel for extraction from high-pressure gases. *International Journal of Mass Spectrometry* 379 (Mar. 2015), 110–120. ISSN: 1387-3806.

[77] K. Murray et al. Design of a multiple-reflection time-of-flight mass spectrometer for barium-tagging. *Hyperfine Interactions* 240(1) (2019).

[78] D. J. Harvey. *Mass Spectrometry | Overview*. Encyclopedia of Analytical Science (Third Edition), 2019.

[79] E. M. E. McDaniel. *The Mobility and Diffusion of Ions in Gases*. John Wiley Sons, New York, 1973.

[80] E. M. E. Mason. *Transport Properties of Ions in Gases*. John Wiley Sons, New York, 1988.

[81] https://www.comsol.com/multiphysics/diffusion-equation. Fick's Law, COMSOL.

[82] Z. K. G. Eiceman. Ion Mobility Spectrometry. *CRC Press, Inc.* (1994).

[83] H. E. Revercomb and E. A. Mason. Theory of plasma chromatography/gaseous electrophoresis. Review. *Analytical Chemistry* 47(7) (1975), 970–983.

[84] V. Gabelica and E. Marklund. Fundamentals of ion mobility spectrometry. *Current Opinion in Chemical Biology* 42 (Feb. 2018), 51–59. ISSN: 1367-5931.

[85] https://labs.chem.ucsb.edu/bowers/michael/theory_analysis/ion-mobility/cross-sections/index.shtml. Ion Mobility Theory.

[86] M. Laatiaou. Development of an Ion Mobility Spectrometer for Heavy Element Research. PhD thesis. University of Munich, 2009.

[87] A. Cortez. *A Practical Approach to Ion Mobility*. New Horizons in Time Projection Cambers, Santiago de Compostela (Spain), 2020.

[88] S.-C. J. et al. Measurements of the mobility of alkaline earth ions in liquid xenon. . *Phys. D: Appl. Phys.* 42 (2008).

[89] TRIUMF. http://www.triumf.ca/research-program/research-topics. Research Topics.

[90] TRIUMF. http://www.triumf.ca/research-program/research-facilities/main-cyclotron-beam-lines. Main Cyclotron and Beam Lines.

[91] J. Dilling, R. Krucken, and G. Ball. ISAC overview. *Hyperfine Interactions* (January 2014), 1–8. ISSN: 1572-9540.

[92] Y. Blumenfeld, T. Nilsson, and P. Van Duppen. Facilities and methods for radioactive ion beam production. *Physica Scripta* (2013).

[93] L. R. Marchetto M. High energy beam lines. *Hyperfine Interactions* 225 (2014).

[94] J. Dilling, R. Krucken, and L. Merminga. ISAC and ARIEL: The TRIUMF radioactive beam facilities and the scientific program. *Springer, Dordrecht* (January 2014), 1–284.

[95] N. I. of Standards and Technology. NIST Standard Reference Database 69: NIST Chemistry WebBook, Saturation Properties for Xenon — Temperature Increments (2024).

[96] J. Lab. Accessed Jan 2024.

[97] M. Ziegler et al. Calculation of the Vapor Pressure and Heats of Vaporization and Sublimation of Liquids and Solids below One Atmosphere Pressure VIII. Xenon. *Ga. Inst. Technol.* (1966).

[98] L. A. N. Laboratory. Accessed Jan 2024.

[99] M. Gosman et al. Thermodynamic Properties of Argon from the Triple Point to 300 K at Pressures to 1000 Atmospheres. *Nat. Stand. Ref. Data Ser.* (1969).

[100] U. Jefferson Lab. Accessed Jan 2024.

[101] M. Ziegler et al. Calculation of the Vapor Pressure and Heats of Vaporization and Sublimation of Liquids and Solids below One Atmosphere Pressure. VI. Krypton, *Ga. Inst. Technol.* (1964).

[102] K. Twelker et al. An apparatus to manipulate and identify individual Ba ions from bulk liquid Xe. *Review of Scientific Instruments* 85 (2014).

[103] K. Twelker. Surface adsorption and resonance ionization spectroscopy for barium identification in neutrinoless double beta decay experiments. *PhD. Thesis, Stanford University* (2014).

[104] S. Kravitz. Identification of single barium atoms with resonance ionization mass spectroscopy for the nEXO neutrinoless double beta decay experiment. *PhD. Thesis, Stanford University* (2017).

[105] M. E. Ghossain. Calculations of Stopping Power, and Range of Ions Radiation (Alpha Particles) Interaction with Different Materials and Human Body Parts. *International Journal of Physics* 5(3) (2017).

[106] Y. Song and Y. Wang. Effect of ion-nucleus sizes on the electric stopping power for heavy ions in solids. *Nuclear Instruments and Methods in Physics B* 135 (1998).

[107] W. Brandt and M. Kitagawa. Effective stopping-power charges of swift ions in condensed matter. *Phys. Rev. B* 25(9) (1982).

[108] K. Wamba. Aspects of the RD for the Enriched Xenon Observatory for double beta decay. PhD thesis. Stanford University, 2006.

[109] R. Sandler et al. Investigation of the potential ultralow Q-value -decay candidates 89Sr and 139Ba using Penning trap mass spectrometry. *Physical Review C* 100(2) (Aug. 2019).

[110] P. Joshi. Nuclear Data Sheets. *National Nuclear Data Centre* 138 (2016).

[111] D. Ray. *Stopping Power Ranges of* ^{139}*Cs in Various media*. Private communication, 2023.

[112] SIMION. https://simion.com/info/manual.html. SIMION User Manual.

[113] COMSOL. https://www.comsol.com/multiphysics/finite-element-method?parent=physics-pdes-numerical-042-62. An Introduction to the Finite Element Method.

[114] COMSOL. https://www.comsol.com/multiphysics/electrostatics-theory. Accessed Dec 2023.

[115] A. Harvey and E. Lemmon. Method for Estimating the Dielectric Constant of Natural Gas Mixtures. *International Journal of Thermophysics* (1) (2005).

[116] V. Streeter. *Fluid Mechanics, Section 3.3*. McGraw-Hill, 1951-1966.

[117] COMSOL. https://doc.comsol.com/5.4/doc/com.comsol.help.particle/ParticleTracingModuleUsersGuide.pdf. COMSOL Particle Tracing Module Users Guide.

[118] COMSOL. https://www.comsol.fr/blogs/what-formulation-should-i-use-for-particle-tracing-in-fluids/. Formulation.

[119] COMSOL. https://doc.comsol.com/6.0/doc/com.comsol.help.particle/particle_ug_modeling.05.09.html#683513. Particle Tracing Formulation.

[120] P. Agnes. Measurement of the ion fraction and mobility of 218-Po produced in 222-Rn decays in liquid argon. *Journal of Instrumentation* (2019).

[121] E. Bainglass et al. Mobility and clustering of barium ions and dications in high-pressure xenon gas. *Physical Review A* 97(6) (June 2018). ISSN: 2469-9934.

[122] L. A. Viehland and D. S. Hampt. The distribution of velocities for Ba+ ions in Ar gas. *The Journal of Chemical Physics* (1992).